





3 1293 01055 3257

This is to certify that the  
dissertation entitled  
LASER SURFACE TREATMENT OF STEEL  
USING ND:YAG LASER  
presented by  
Motilal J. Tayal  
has been accepted towards fulfillment  
of the requirements for  
Ph.D. degree in Materials Science

  
K. Mukherjee  
Major professor

Date May 14, 1992

**LIBRARY**  
**Michigan State**  
**University**

**PLACE IN RETURN BOX to remove this checkout from your record.**  
**TO AVOID FINES return on or before date due.**

<b>DATE DUE</b>	<b>DATE DUE</b>	<b>DATE DUE</b>
OCT 05 1998 <del>11-4629703</del>	_____	_____
_____	_____	_____
_____	_____	_____
_____	_____	_____
_____	_____	_____
_____	_____	_____
_____	_____	_____

**MSU is An Affirmative Action/Equal Opportunity Institution**

c:\cric\datedue.pm3-p.1

**LASER SURFACE TREATMENT OF STEEL USING**

**ND:YAG LASER**

**By**

**Motilal J. Tayal**

**A DISSERTATION**

**Submitted to**

**Michigan State University**

**in partial fulfilment of the requirements**

**for the degree of**

**DOCTOR OF PHILOSOPHY**

**Department of Materials Science and Mechanics**

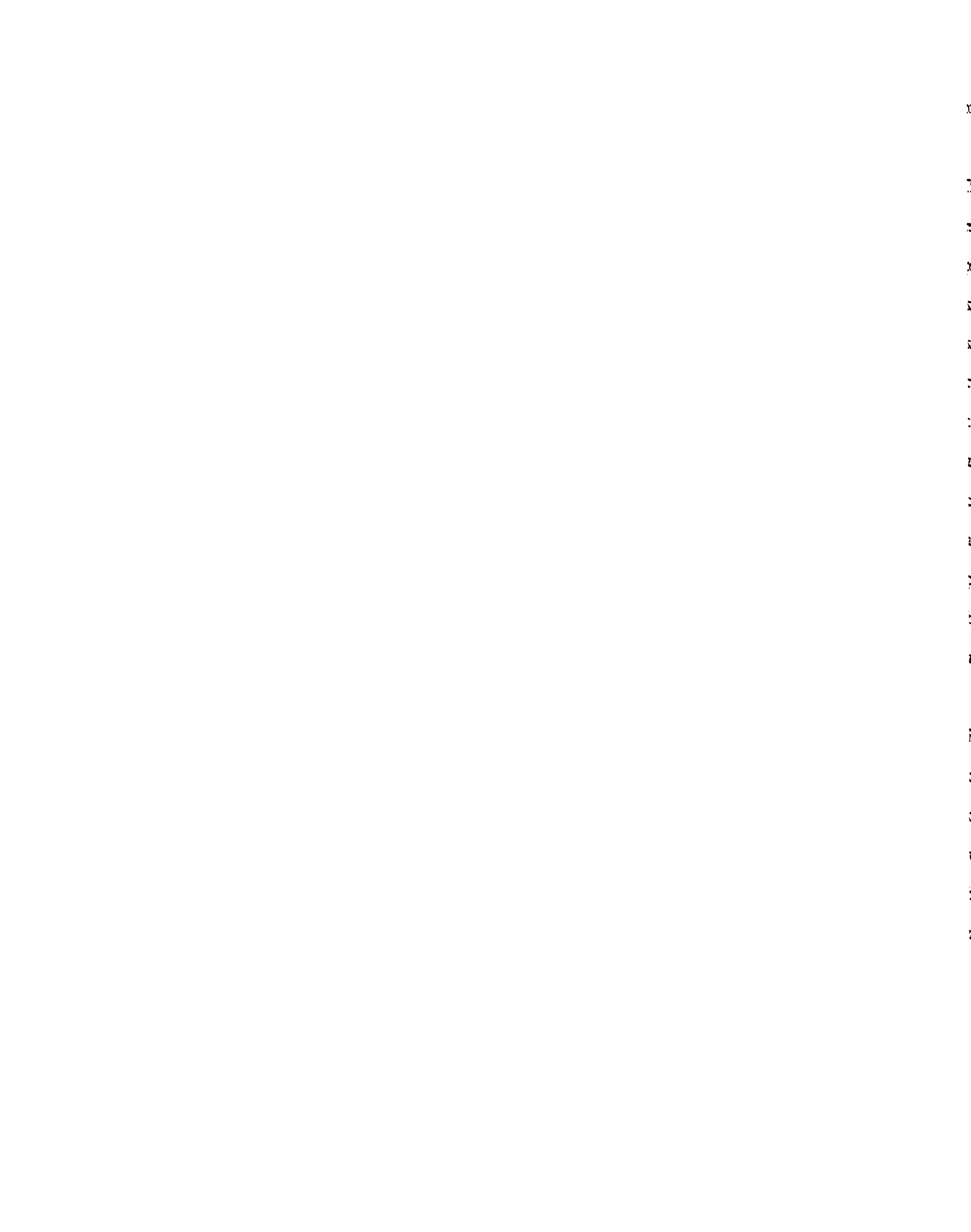
**1992**

**ABSTRACT**  
**LASER SURFACE TREATMENT OF STEEL USING**  
**ND:YAG LASER**

**By**  
**Motilal J. Tayal**

**Laser surface treatment of steel is a process of growing interest for local surface modifications. This process makes the surface wear resistant by modifying the microstructure, and or composition locally. Selective surface treatments like transformation hardening, carburizing, and boriding can be done using a high-energy laser. Selective hardening of AISI 1045 steel has been achieved by using a Nd:Yag laser under different process parameters. The maximum surface hardness of ~780 Hv has been achieved. The relatively high hardness is attributed to the fineness of the martensitic structure, attained by a relatively high cooling rate in laser processing. The highest hardness of the laser surface hardened layer increases with power density of laser, up to a certain level. Pre-processing surface treatments like etching, and graphite coating improve the coupling of laser energy significantly.**

**The highest hardness, which can be obtained by laser transformation hardening of AISI 1018 steel is ~450 Hv. The higher hardness of 1050 Hv has been achieved in this steel by laser carburizing. Incorporation of higher carbon concentration, through fine ledeburitic microstructure in surface layers, produces such high hardness. Further increase in hardness can be obtained by laser boriding. Laser boriding of AISI 1018 steel produces hardness ranging from 1350 to 2200 Hv (can be compared with the hardness of SiC ~ 2300 HV). The amount of boron controls the type and amount of boride phases, formed in surface layers, treated by laser. The phases responsible for such high hardness were found to be FeB and or Fe<sub>2</sub>B, in varying proportions. FeB phase was found to be the hardest phase in the laser**



borided surfaces of AISI 1018 steel, having hardness of ~2200 Hv.

The laser surface treatments described above, rely on the modification of the surface with respect to microstructure and/or composition. This is controlled by the distribution of temperature on the surface, to be laser treated. Temperature distribution controls the microstructure scale, morphology, and microcracking (which is often associated with laser surface processing), which leads to the next phase of this thesis. A simple analytical heat transfer model, using Green's functions, was developed to predict the temperature distribution on a workpiece during laser surface treatment. This model demonstrates a new approach to formulate heat transfer problems, involving high energy sources. The model can be used to predict the case depth during laser hardening. The results obtained by the analytical model compare fairly well with the results, obtained by the commercial FEM package ANSYS. The simulation of moving laser, in ANSYS, showed that maximum hardness achieved at the surface of a workpiece is shifted towards the trailing end. The above analytical model has been modified to implement the laser traverse speed.

Few problems have been encountered with laser carburizing of AISI 1018 steel. In some cases, cracks and porosity have been found in the laser treated surface. The cracks produced were found to be of two kinds: straight cracks and wiggly cracks. The cracks formed were due to a combination of various factors such as shrinkage, thermal stresses, surface brittleness and low melting point, interdendritic liquid phase. The contribution of these factors, were analyzed in detail.

## **ACKNOWLEDGMENTS**

**I would like to express my appreciation and gratitude to Professor Kali Mukherjee, my major advisor, for his constant support, encouragement, patience, guidance and friendship, and especially invaluable assistance in the preparation of this thesis.**

**Dr. K. N. Subramanian, Dr. Dahsin Liu and Dr. C. Foiles, my thesis committee members, for their support, suggestions and understanding.**

**Department of Materials Science and Mechanics at Michigan State University for providing me teaching assistantship during my studies and Division of Engineering Research at MSU for partially supporting my stay at school.**

## LIST OF CONTENTS

	page
<b>LIST OF TABLES</b> .....	vii
<b>LIST OF FIGURES</b> .....	viii
<b>I. INTRODUCTION</b> .....	1
<b>II. BACKGROUND</b>	
<b>2.1. High Power Lasers</b> .....	4
<b>2.1.1. Gas Lasers</b> .....	5
<b>2.1.1.1. CO<sub>2</sub> Laser</b> .....	5
<b>2.1.2. Solid State Lasers</b> .....	10
<b>2.1.2.1. Ruby Laser</b> .....	10
<b>2.1.2.2. Nd:Yag Laser</b> .....	11
<b>2.1.3. Chemical Lasers</b> .....	13
<b>2.1.4. Semiconductor Lasers</b> .....	13
<b>2.2. Laser Process Parameters</b> .....	16
<b>2.2.1. Laser Power</b> .....	16
<b>2.2.2. Laser Beam Diameter and Intensity Distribution</b> .....	17
<b>2.2.3. Absorptivity</b> .....	22
<b>2.2.4. Traverse Speed</b> .....	25
<b>2.2.5. Shielding Gas</b> .....	25
<b>2.3. Laser Surface Treatment</b> .....	27
<b>2.3.1. Laser Surface Alloying</b> .....	29
<b>2.3.1.1. Alloy Deposition Systems</b> .....	34

2.3.2. Laser Cladding .....	35
2.3.3. Laser Glazing .....	35
2.3.4. Laser Shock Hardening .....	38
2.4. Laser Heat Treatment of Steel .....	38
2.4.1. Transformation Hardening .....	40
2.4.2. Laser Alloying and Cladding of Steel .....	41
2.5. Heat Transfer in Laser Surface Treatment .....	43
2.6. Solidification During Laser Surface Treatment .....	51
2.6.1. Grain Structure .....	52
2.6.2. Subgrain Structure .....	54
2.7. Thermal and Residual Stresses Involved in Surface Treatments .....	59
2.7.1. Measurement of Residual Stresses .....	64
2.7.1.1. Center Hole Method .....	64
2.7.1.2. Curvature Method .....	66
2.7.1.3. Non-Destructive Methods .....	68
<b>III. EXPERIMENTAL WORK .....</b>	<b>72</b>
<b>IV. RESULTS AND DISCUSSION</b>	
4.1. Laser Hardening .....	78
4.1.1. Microstructural Study .....	78
4.1.2. Effects of Surface Conditions .....	81
4.1.3. Effect of Laser Power, Traverse Speed and Defocal Conditions .....	84
4.1.4. Experimental Model .....	88

4.1.5. Hardness in the Case Depth .....	89
4.2. Laser Carburizing .....	91
4.2.1. Microstructural and Hardness Profile Study .....	91
4.2.2. Solidification Morphology .....	105
4.2.3. Features of Austenite in Laser Carburized Zone .....	119
4.2.4. Limitations of Laser Carburizing .....	123
4.3. Laser Boriding	
4.3.1. Microstructural Studies .....	135
4.3.2. Hardness Profile Study .....	143
4.3.3. Phase and Composition Analysis .....	143
4.3.4. Stress State in Laser Borided Layer .....	147
4.4. A New Approach to Temperature Distribution Modelling During Laser hardening .....	150
4.4.1. Physical Definition of the Process .....	151
4.4.2. Mathematical Definition of the Process .....	151
4.4.3. Derivation of the Model .....	153
4.4.4. Solution of the Model .....	156
<b>V. CONCLUSIONS</b> .....	165
<b>VI. APPENDICES</b>	
(A) A Complete Solution of the Model Developed in Section 4.4 .....	167
(B) Computer Program to Solve the Model in Section 4.4 .....	170
(C) Development of Heat Transfer Model for a Moving Laser Source.....	179
<b>VII. REFERENCES</b> .....	184



## LIST OF TABLES

	<b>Page</b>
1. Laser cladding activities .....	37
2. Composition of steels in weight percentage .....	72
3. Values of thermal expansion coefficients .....	147

## LIST OF FIGURES

Figure		Page
1.	Schematic diagram of a conventional discharge CO <sub>2</sub> :N <sub>2</sub> :He laser.[96].....	6
2.	Two methods of exciting a CO <sub>2</sub> gas laser. (a) Discharge applied to CO <sub>2</sub> :N <sub>2</sub> :He mixture directly, (b) Only N <sub>2</sub> excited in discharge followed by resonant energy transfer to CO <sub>2</sub> downstream .....	8
3.	Energy level diagram for CO <sub>2</sub> and N <sub>2</sub> . [14] .....	9
4.	Energy levels of the Nd ion. [25] .....	12
5.	Barrier voltage for a p-n junction in a semiconductor [26]. (a) without a forward bias, and (b) with a forward bias. ....	15
6.	Different Q-switching types and their applications. [24] .....	18
7.	Beam manipulation techniques: (a) segmented mirror system [33], (b) two-axis vibrator system [33] and (c) optical integrator [12] .....	21
8.	Absorption of laser light in iron as a function of wavelength and temperature. [166] .....	24
9.	Relationship between the traversal speed and case depth in various materials. [33] .....	26
10.	Weld penetration versus weld speed for 304 steel welded with a 10 Kw CO <sub>2</sub> laser. [27] .....	26
11.	Achievement of welds in different gases. [47] .....	28
12.	Blanketing effect of an addition of 10% argon to a helium shielding gas. [47] .....	28
13.	Methods of laser surface treatment of materials. [48] .....	30
14.	Operational regimes for various laser materials processing techniques. [49] .....	31
15.	Laser cladding with blown powder. [48] .....	36

16.	The laser shock process [90]: (a) laser shocking setup and (b) schematic of the vaporization and pressure reactions at the metal surface during laser irradiation. ....	39
17.	Cr concentration profile on cross-section of melt trail (250 micro-meter) for Cr on iron scanned with CW CO <sub>2</sub> laser. [96] .....	42
18.	Comparison of abrasive wear resistance of various laser treated structures, TiB <sub>2</sub> coated. ....	44
19.	(a) Temperature distribution due to a moving source of heat and (b) temperature distribution at cross-sections shown in (a) [95] .....	47
20.	Schematic of temperature distribution around heat source. (a) and (b) are the representation in the form of a hill, (c) and (d) are the representation in topographic projection. Temperature distribution shown in (a) and (c) is in a plate treated with higher traversal speed where as the temperature distribution in (b) and (d) is a plate treated with comparatively slower traversal speed. [96] .....	49
21.	Competitive growth in the fusion zone. The arrows in the grains of the base metal indicate the easy growth direction, say <100> in f. c. c or b. c. c. metals. [122] .....	53
22.	Comparison of weld pool shapes: (a) slow, (b) intermediate, and (c) fast speed[164] .....	55
23.	Constitutional supercooling in alloy solidification [133]. (a) phase diagram, (b) solute-enriched layer in front of the solid/liquid interface and (c) constitutional supercooling.....	57
24.	Crude representation of development of residual stresses in a cooling hot ingot. [137] .....	61
25.	(a) Volume change for martensite in steel, and (b) typical hardness and residual stress profiles. [139] .....	63
26.	Distribution of longitudinal and transverse residual stresses and of transverse strains along the y and x axis in a single pass welding. [140] .....	65
27.	45° rectangular strain gage rosette for residual stress measurement. [149].....	67
28.	(a) Schematic of the sample, after a mechanical sputtering of	

	one of its large faces, the symmetry is broken and the sample bends. (b) variation of the sample curvature with the residual thickness 'h'. [159] .....	67
29.	Lattice spacing variation with $\sin^2(\psi)$ , in four different cases. [154] ..	71
30	Microstructure of AISI 1018 steel before laser treatment. ....	73
31,	Microstructure of AISI 1045 steel before laser treatment .....	73
32.	Sample design used for laser transformation hardening. ....	74
33.	Schematic of laser carburizing / laser boriding. ....	76
34.	Typical HAZ of laser hardened sample (a) (x75): (i), (ii), (iii) and (iv) are the magnified (x500) views of the 4 sub-zones respectively. ....	79
35.	Subzones in HAZ corresponding to AISI 1045 temperatures in the Fe-Fe <sub>3</sub> C equilibrium diagram.....	80
36.	Micrographs comparing martensite (a) from conventional (furnace) heating, x3000 and (b) from laser hardening, x3000. ....	82
37.	Influence of surface conditions on the hardness profiles at the HAZ of laser hardened samples. ....	83
38.	Hardness profiles at the HAZ of laser hardened samples, with increasing laser power (just up to austenization).....	85
39.	Hardness profiles at the HAZ of laser hardened samples, with increasing laser power (beyond austenization). ....	86
40.	Influence of focal conditions on the hardness profiles at the HAZ of laser hardened samples. ....	87
41.	Comparison of hardness profiles at the transverse section of samples, surface treated by laser hardening and laser carburizing ....	92
42.	Fe - Fe <sub>3</sub> C equilibrium diagram. [185].....	93
43.	SEM micrograph showing hypo-eutectic structure. Laser power 200 W, traversal speed 3.88 mm/s, and graphite layer thickness 0.41 mm. (x8000) .....	94
44.	SEM micrograph showing eutectic structure. Laser power 150 W,	

	traversal speed 3.88 mm/s, and graphite layer thickness 0.41 mm. (x10900). .....	95
45.	SEM micrograph showing hyper-eutectic structure. Laser power 200 W, traversal speed 3.88 mm/s, and graphite layer thickness 0.41 mm. (x13000) .....	96
46.	SEM micrograph showing martensite structure. Laser power 250 W, traversal speed 3.88 mm/s, and graphite layer thickness 0.13 mm. (x4000). .....	97
47.	SEM micrograph showing the variation of microstructure from center line of the carburized zone to fusion line of carburized zone. Laser power 200 W, traversal speed 3.88 mm/s, and graphite layer thickness 0.41 mm. (x500) .....	99
48.	SEM micrograph of transverse section of laser carburized sample, showing hyper-eutectic structure. Laser power 100 W, traversal speed 3.88 mm/s and, graphite layer thickness 0.18 mm. (x500) .....	100
49.	Influence of laser power on the hardness profiles in the transverse section of carburized zones. ....	102
50.	Influence of graphite layer thickness (level of carbon dilution) on the hardness profiles in the transverse section of carburized zones...	103
51.	Micrographs showing the variation of microstructure, in carburized zone with varying degree of concentration of carbon. (a) hyper-eutectic structure, x500, (b) hypo-eutectic structure, x500, and (c) martensitic structure, x1000. ....	104
52.	SEM micrograph, from longitudinal section of carburized zone, showing cellular morphology. Laser power 200 W, traversal speed 3.88 mm/s and graphite layer thickness 0.41 mm. (x13000).....	106
53.	SEM micrograph showing degenerated cellular morphology. (x6000) .....	107
54.	SEM micrograph showing dendritic morphology in the carburized zone. Laser power 200 W, traversal speed 3.88 mm/s, and graphite layer thickness 0.41 mm. (x12000) .....	108
55.	SEM micrograph showing dendritic morphology in the carburized zone. Laser power 200 W, traversal speed 3.88 mm/s and graphite layer thickness 0.41 mm. (x7900) .....	109

56.	SEM micrograph, from the carburized zone, showing acicular morphology. Laser power 100 W, traversal speed 4.25 mm/s, and graphite layer thickness 0.22 mm. (x1000). .....	110
57.	SEM micrograph showing cellular-planar structure. Laser power 150 W, traversal speed 3.88 mm/s, and graphite layer thickness 0.41 mm. (x13000) .....	111
58.	Schematic diagram, showing the relationship between laser traversal speed and actual growth rate. [133] .....	113
59.	Schematic illustration of morphology change from planar to cellular and cellular dendritic as the temperature gradient, in the solidification direction, decreases. The temperature gradient decreases from (a) to (c). The arrows in the grains of the base metal indicate the easy growth direction. ....	114
60.	Schematic diagram illustrating the effect of G, R and carbon content on the evolution of various morphologies.....	115
61.	Planar-to-cellular-to-cellular dendritic transition in the laser carburized zone. (a) micrograph (x1000) and (b) schematic illustrations. ....	117
62.	Micrograph from longitudinal section of carburized zone, showing multidirectional orientation. Laser power 250 W, traversal speed 3.88 mm/s, and graphite layer thickness 0.41 mm. (x1000). ....	118
63.	SEM micrograph showing interconnected carbide network in the hyper-eutectic structure. Laser power 150 W, traversal speed 3.88 mm/s, and graphite layer thickness 0.41 mm. (x10,000) .....	120
64.	SEM micrograph showing carbide monoliths in hyper-eutectic structure. (x3500) .....	121
65.	X-ray Diffraction data from laser carburized zone. ....	122
66.	Micrograph showing the limitations of laser carburizing: porosity and cracks. (x500) .....	124
67.	Micrograph showing typical (a) straight cracks (x200), and (b) wiggly cracks. (x150). ....	126
68.	SEM micrograph showing wiggly cracks around austenite dendrites, (x2500). ....	127

69

70

71

72

73

74

75

76

77

78

79

80

81

69.	SEM micrograph showing wiggly cracks (intergranular along prior austenite grain boundaries). (x690) .....	128
70.	Effect of composition on wiggly cracking susceptibility of laser carburized zone. Regions of cracks susceptibility: A no cracking; B liquid healing possible; C crack sensitive.....	129
71.	SEM micrograph showing intergranular cracking (straight) in iron carbide needles. Laser power 100 W, traversal speed 3.88 mm/s, and graphite layer thickness 0.41 mm. (x6000) .....	131
72.	SEM micrograph showing transgranular cracking (straight) in iron carbide needles. (x5000) .....	132
73.	SEM micrograph showing the mixed mode cracking in iron carbide needles. Laser power 100 W, traversal speed 3.88 mm/s and graphite layer thickness 0.41 mm (x4900) .....	133
74.	Schematic cooling curves showing the difference in contraction of the surface and interior.....	134
75.	Comparison of hardness profiles at the transverse sections of samples, treated by laser carburizing and boriding. ....	136
76.	Typical microstructure of laser borided zone. Two passes of laser (200 W), boron layer thickness 0.30 mm, and traversal speed 2 mm/s. (a) x1500 and (b) a portion of (a) at x2000 .....	138
77.	Fe-B equilibrium diagram. [185] .....	139
78.	Laser borided microstructure showing additional features, as compared to that in figure 76. 3 cycles of laser passes (200 W) and boron coating laying, traversal speed 2 mm/s. (x1000) .....	141
79.	SEM micrograph of transverse section of laser borided zone, showing softer microstructure, mixture of Fe <sub>2</sub> B and eutectic. Two passes of laser (200 W) on boron coated (.18 mm) sample, with traversal speed of 2 mm/s. (x200) .....	142
80.	Hardness profiles at the transverse section of laser borided samples, treated under different process conditions. In this figure 'x' is the number of times boron coating was laid, 'y' is the number of laser passes, 'p' is the laser power (watts) and 't' is the thickness (in mm) of boron coating. ....	144
81.	X-ray diffraction data from laser borided zone, process conditions	

	for this sample are shown in figure 78.....	146
82.	Micrograph showing boron and iron mapping in an area near the surface (in transverse section) of laser borided sample. Bigger grains are found to be FeB and smaller grains are Fe <sub>2</sub> B. (sample from fig. 78). (a) main micrograph, (x800), (b) boron mapping, and (c) iron mapping.....	148
83.	Micrograph showing boron and iron mapping in an area away from surface (transverse section) of laser borided sample. Grains are found to be FeB and Fe <sub>2</sub> B. Process conditions are shown in fig. 78. (a) main micrograph, (x800), (b) boron mapping and (c) iron mapping. ....	149
84.	Schematic diagram illustrating the various dimensions, coordinates and boundary conditions for the laser surface processing heat transfer model. ....	152
85.	Main flow chart of computer program, developed to solve the analytical heat transfer model .....	157
86.	Detailed flow chart for the computation of triple summation in the heat transfer model. ....	158
87.	Diagram showing computed temperature variation with increasing laser dwell time on the sample .....	159
88.	Temperature contour on AISI 1018 steel surface due to impingement of stationary laser. Laser power 200 W and interaction time 0.1 s ...	161
89.	Temperature contour on AISI 1018 steel surface due to a moving laser . Laser power 200 W, interaction time 0.1 sec., snap shot at time 0.2 s. ....	162
90.	Temperature contour on AISI 1018 steel surface due to a moving laser. Laser power 200 W, interaction time 0.1 sec., snap shot at time 0.3 s.....	163
91.	Schematic diagram illustrating the various dimensions, coordinates and boundary conditions for the laser surface processing heat transfer model in appendix C. ....	180

## INTRODUCTION

Localized surface treatment of steel with a laser is an emerging technique. It has proven to be superior to other conventional techniques such as induction hardening, flame spraying [1] and plasma spraying. Induction hardening is not suitable for parts with complex geometry. Laser hardening provides a very good alternative [2]. By easy manipulation of optics, inaccessible areas such as grooves and notches can be reached by laser. Flame spraying technique can not provide focussed high energy; hence, the width of the heat affected zone (HAZ) is considerably high, leading to distortion. The distortion requires post treatment machining [3,4]. Laser surface treatment of steel can be achieved with minimum distortion.

Laser surface treatments can be of various types; transformation hardening [5,6,7], alloying [8] and cladding [9]. The effectiveness of each of these laser treatments depends on laser process parameters. The laser process parameters are power, traverse speed, and spot size. Applications of laser surface treatment in the automobile industry have been investigated extensively. Laser hardening of areas such as engine cylinder bores, valve seats, and steering housing has been investigated [3,10,11]. Most of the published work on laser surface treatment has been performed using a high power CO<sub>2</sub> laser. In this work the laser used was a 400 watt Nd:Yag laser. The idea behind using a Nd:Yag laser instead of a CO<sub>2</sub> laser, was to explore the possibility of tapping the better coupling factor of Nd:Yag laser beam (wavelength = 1.06  $\mu\text{m}$ ) with metals. The Nd:Yag laser has an absorption coefficient of 60% for ferrous alloys as compared to that of 20% for CO<sub>2</sub> laser [12].

The materials' properties such as wear resistance, erosion resistance, and corrosion resistance depend on microstructure and the composition of the surface. Conventionally the

wear resistance of low hardness steels is improved by solid state carburizing and diffusion boronizing. Such techniques are time consuming and cumbersome for surface treatment of confined areas such as grooves and notches. The laser is an alternative to implement such techniques in a very controlled fashion, which does not require any pre- or post processing treatments. Present investigation is focussed on determining the relationship between laser process parameters, microstructure, composition, and the hardness of laser surface treated steel. AISI 1018 steel specimens were selected for laser carburizing and laser boriding studies. Such steels are very commonly used for automobile components such as gears and connecting rods, which need surface treatments. AISI 1045 steel specimens were selected for laser hardening studies. Such steels are typical of candidate materials for a variety of hardened automobile components such as main shaft and pinions. Research in this dissertation is focused on a number of distinct, although related, topics leading to a conclusion on the feasibility of various laser surface treatments like transformation hardening of AISI 1045 steel, carburizing of AISI 1018 steel, and boriding of AISI 1018 steel. The phases investigated are:

**(a) Microstructural study:** Systematic studies were carried out to correlate the microstructure produced during laser surface treatments with the process parameters. The microstructures were studied with respect to:

- (i) various phases produced during different laser surface treatments
- (ii) morphology of microstructures produced during laser surface treatment.

**(b) Phase and Chemical analysis:** Phase analysis, in the laser surface treated zones, was done using a x-ray diffractometer. Chemical analysis of various phases, present in the surface treated zones, was done by using an electron beam micro-probe.

**(c) Hardness profile study:** This phase of the study involved the hardness profile mea-

surements on the longitudinal and transverse section of the laser surface treated tracks. Optimum laser process parameters were obtained to get maximum surface hardness and hardened depth.

**(d)Heat transfer model:** Laser surface treatment is strictly controlled by temperature distribution achieved at the surface during treatment. An analysis of surface temperature distribution is essential to avoid or minimize surface cracking. A simple analytical heat transfer model, using Green's functions, was developed to predict the temperature distribution on the work piece during laser surface treatments. A commercial FEM code ANSYS was also used to predict the temperature distribution on the work piece during laser surface treatments. The results from the analytical model matched quite closely with the results from ANSYS. A more sophisticated model has been proposed and developed (without a numerical solution), which takes into consideration the dynamic effect of laser traverse velocity, while predicting the temperature distribution on the work piece, during laser surface treatment.

## **II. BACKGROUND**

### **2.1. High Power Lasers**

The word laser is an acronym for Light Amplification by the Stimulated Emission of Radiation. Since the first lasers were constructed, their number and variety have increased very rapidly. Currently, a laser light may just as easily be obtained from a solid (Nd:Yag laser), a liquid (dye lasers) or a gas (CO<sub>2</sub> laser). Power lasers are energy conservation systems, which consist of an oscillator followed by a chain of amplifying stages. Basically, the oscillator comprises a laser head containing the active medium interposed between two mirrors, which form the resonant optical cavity [13]. Using various pumping methods [14], the influx of energy creates a 'population inversion' between the excited levels in the active medium. The number of atoms or molecules which are found in the raised or excited energy state becomes higher than the number in a lower state.

The laser transition from higher state to lower state is governed by the laws of interaction with electromagnetic radiation according to an absorption stimulated emission process [5], and each active medium will be characterized by its own effective cross-section of stimulated emission. When the active medium has a sufficiently large stimulated emission cross-section, the photon produced by stimulated emission will be reflected by the mirrors at each end of the cavity and will be amplified on each pass by stimulated radiation. A very large photon pulse is thus built up which leaves the oscillator by one of the semi-transparent mirrors. Power lasers may be classified in four categories according to the pumping method[15]:

- (1) Optical pumping (e.g. Nd:Yag laser).
- (2) Electrically excited pumping (e.g. CO<sub>2</sub> laser).
- (3) Pumping by excitation transfer (e.g. a gaseous mixture of water, N<sub>2</sub> and CO<sub>2</sub> )

(4) Pumping by particle acceleration (e.g. free electron laser).

Among the various lasers, gas lasers and solid state lasers are most widely used commercially for materials processing.

### **2.1.1 Gas Lasers**

Lasers which utilize a gaseous material as the active laser medium have been extremely common [16]. There are various advantages of using gas as active medium. The material is homogeneous, so the problems involving optical inhomogeneity, that are common in solid state lasers, are avoided. Heat can be removed readily by transporting the heated gas out of the region of the interaction. Gas laser can be subdivided into three categories; neutral gas laser (e.g. Helium-Neon laser), the ionized gas laser (e.g. Argon laser), and the molecular laser (e.g. CO<sub>2</sub> laser). Gas lasers may have a continuously flowing or contained lasing medium. The medium needs to be excited to a higher energy state in order to emit photons of energy. The pumping source is normally an electric discharge through electrodes inside the laser cavity. The atoms get excited after collision with other atoms or electrons accelerated by the electric field. Excitation is also possible with electron beam, chemical transitions and transition induced by sudden changes in pressure through expansion of the gases [17]. Gas lasers can be used in continuous wave (CW) or pulse wave (PW) mode; but CW mode is the one, most often used.

#### **2.1.1.1 CO<sub>2</sub> Laser**

The CO<sub>2</sub> laser is the most widely used gas laser. It is notable for its relatively high efficiency [18]. Most lasers have low efficiency of conversion of electrical energy into optical energy. Typical efficiency range from few tenth of a percent up to few percent. The CO<sub>2</sub> laser is capable of operation in the range of the 20-30 % efficiency. The CW CO<sub>2</sub> (figure 1) laser is nothing but a water cooled tube with mirrors on both ends, through which the

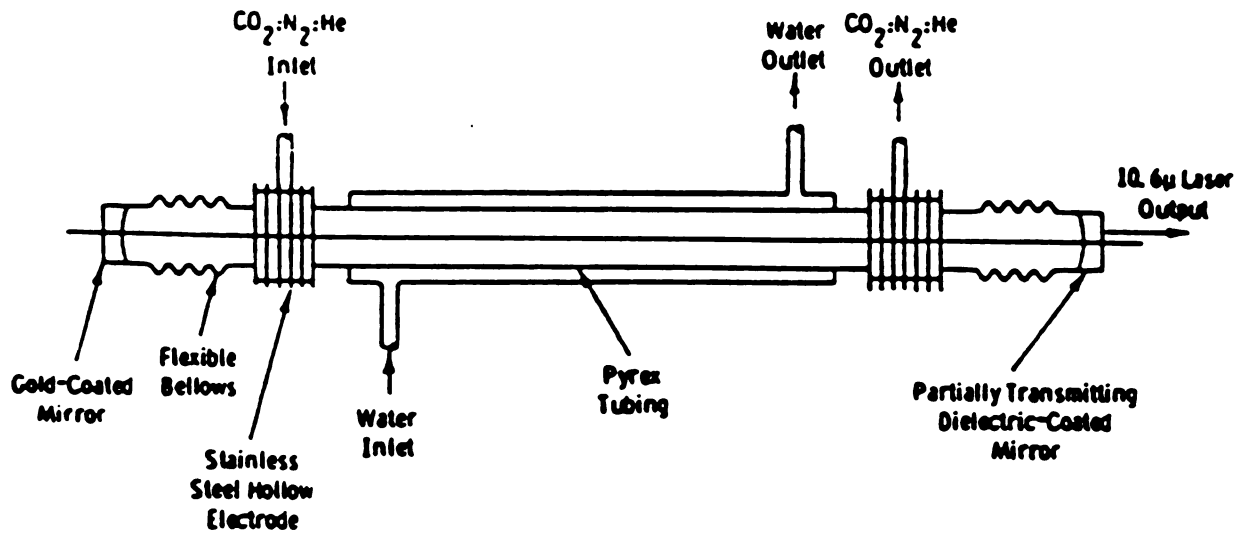


Figure 1. Schematic diagram of a conventional discharge CO<sub>2</sub>:N<sub>2</sub>:He laser.[96]

laser mixture ( $\text{CO}_2$ ,  $\text{N}_2$  and He) is circulated and electrically excited [19]. There are two methods for exciting a  $\text{CO}_2$  laser. The first method applies the discharge energy directly to the continuously flowing  $\text{CO}_2$ : $\text{N}_2$ :He mixture. In order to achieve the highest power from this method, a ratio of 0.8:1:7 of the gases must be used [20]. The output power increases steadily with the flow rate of the gas. This is due to the enhanced removal rate of the dissociation products such as CO and  $\text{CO}_2$ , and the direct cooling of the discharge. The second method consists of separate inlets for the  $\text{N}_2$  and  $\text{CO}_2$  gases. In this case, only the  $\text{N}_2$  is excited by the discharge. The  $\text{N}_2$  molecules will later transfer the energy to the  $\text{CO}_2$  as it collides with  $\text{CO}_2$  downstream (figure 2).

A simplified energy level diagram showing the vibrational energy levels which are important for the  $\text{CO}_2$  laser operation is shown in figure 3. The 001 level is only  $18 \text{ cm}^{-1}$  wavenumber above the first excited vibrational level of the nitrogen molecule which can be excited by collision with electrons having approximately 2 eV of energy in the electrical discharge. This energy is transferred by collision with  $\text{CO}_2$  molecules to the (001) state. This produces a population inversion between the (001) state and the (100) and (020) states. These correspond to laser operation at  $10.6$  and  $9.6 \mu\text{m}$ , respectively. The gain is higher for the  $10.6 \mu\text{m}$  transition, so the preferred transition will be  $10.6 \mu\text{m}$ . The resulting laser radiation, which can be continuously produced is highly monochromatic and exhibits high spatial coherence and high temporal coherence correlation. The spatial coherence results in high radiance from the laser sources. Once produced, the laser energy is allowed to leave the discharge section of the tube through the partially transmitting mirror as a coherent beam. The other end of the tube is covered by a totally reflecting mirror. This mirror helps to direct the laser energy to the opposite end of the tube.

Early experiments showed laser output at a laser wavelength of  $10.6 \mu\text{m}$  in pure  $\text{CO}_2$ : however the power output was low. High power was obtained by adding nitrogen to the mixture

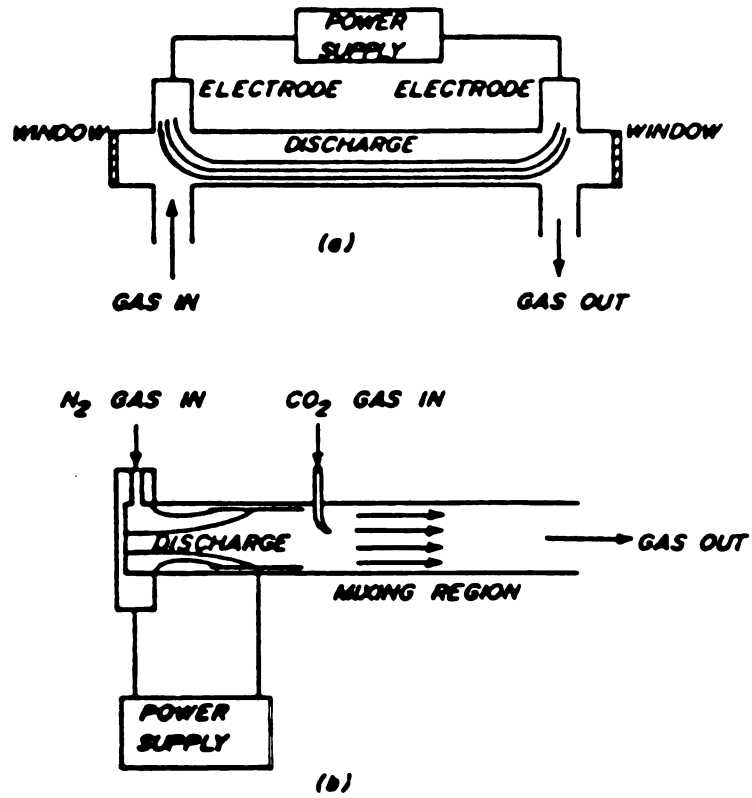


Figure 2. Two methods of exciting a CO<sub>2</sub> gas laser. [13]  
 (a) Discharge applied to CO<sub>2</sub>:N<sub>2</sub>:He mixture directly.  
 (b) Only N<sub>2</sub> excited in discharge followed by resonant energy transfer to CO<sub>2</sub> downstream

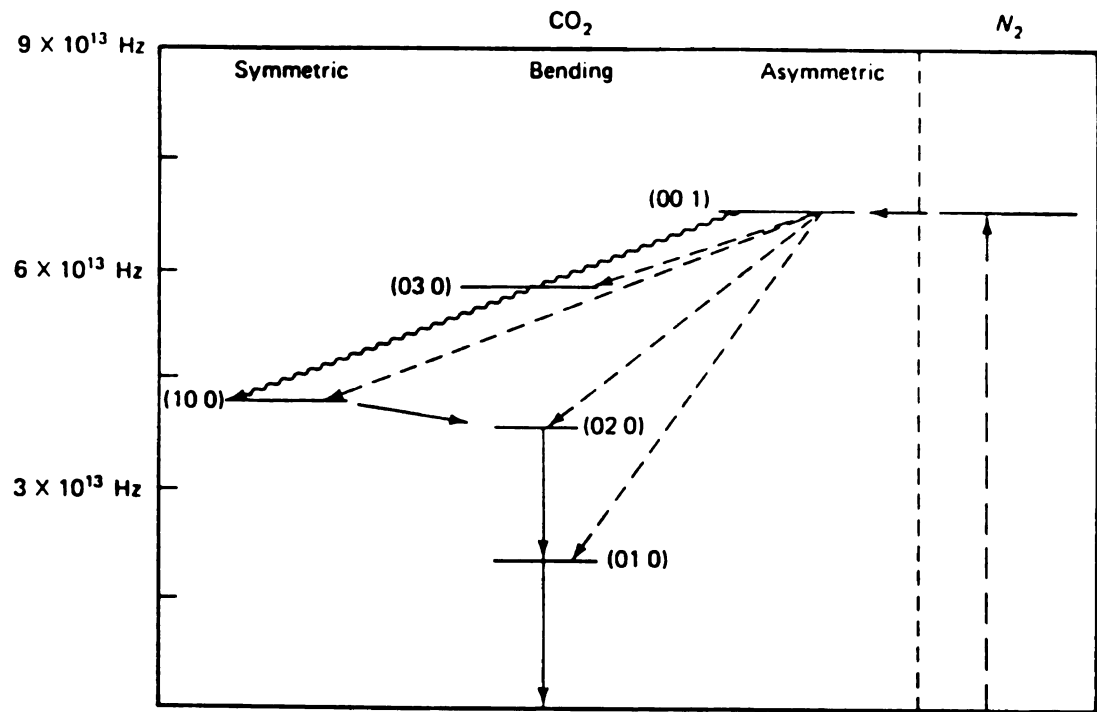


Figure 3. Energy level diagram for CO<sub>2</sub> and N<sub>2</sub>. [14]

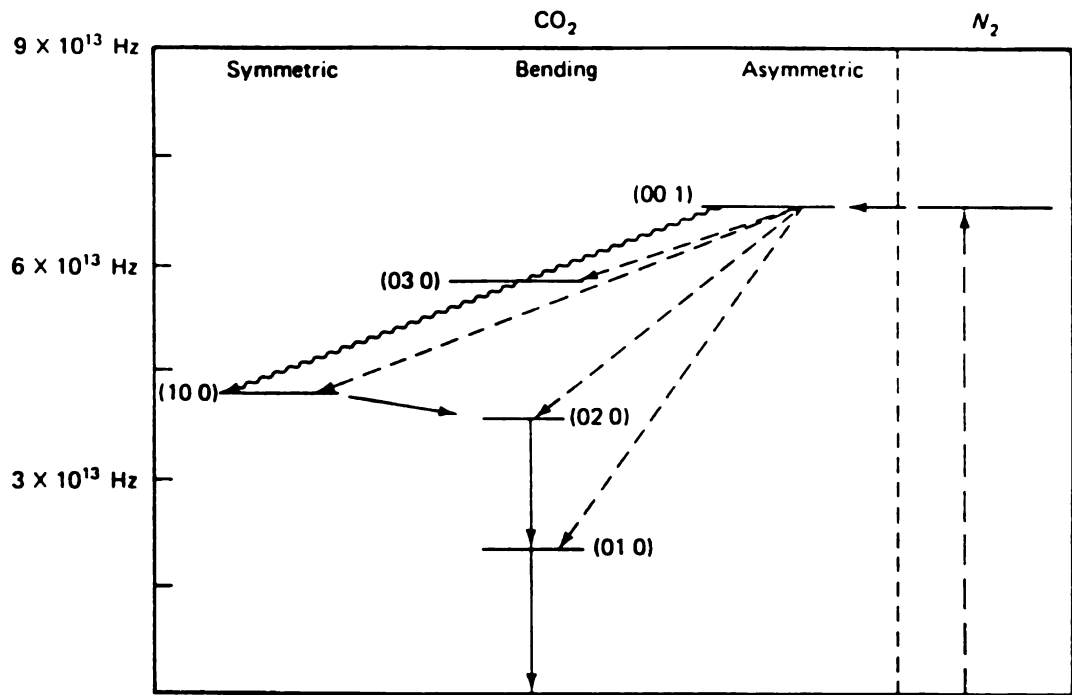


Figure 3. Energy level diagram for CO<sub>2</sub> and N<sub>2</sub>. [14]

[ 21]. The nitrogen molecules enhance population inversion between the (001) and the (100) state. The addition of helium to the gas mixture further increases the output power. The helium helps to deplete the population of the lower level by collision and also helps to keep the gas mixture cool, because of the high mobility of the helium atoms.

There are many applications of CO<sub>2</sub> CW lasers; it can be used for many material fabrication processes like cutting, welding etc. The monochromaticity of the laser light allows it to be used for atomic and molecular spectroscopy. It's temporal coherence allows interferometric measurements and nonlinear optics to be performed. The greatest advantage of the CO<sub>2</sub> laser is it's high power and it's ability to perform in either a pulse wave mode (PW) or continuous wave mode (CW). This increases the number and variety of processes for which it can be used.

### **2.1.2 Solid State Lasers**

The solid state laser is characterized by an active medium involving ions of an impurity in some solid host material. The laser material is in the form of a cylindrical rod with the ends polished flat and parallel. The pumping is done by optical excitation. The impurity ions, that are commonly employed are either ions of the transition metals or of rare earth elements. These elements all share the common features of an interior unfilled shell of electrons, which leads ultimately to a narrow fluorescent linewidth. A narrow fluorescent linewidth is favorable for laser operation [22], because it leads to a high gain, and to reduced requirements on the minimum population inversion necessary for laser operation. There are a variety of solid state lasers available. Neodymium in glass, and Neodymium doped yttrium aluminum garnet (Nd:Yag) are the ones widely used on a commercial basis.

#### **2.1.2.1 Ruby Laser**

The ruby laser is one of the widely used solid state lasers [23]. A cylindrical bar made of synthetic ruby ( $\text{Al}_2\text{O}_3$  doped with 0.5% Cr), acts as the lasing medium. It is the chromium, which provides the lasing action. A flash tube is used to excite the lasing medium. It may be in the form of either a helical tube wrapped around the crystal, or a rod placed parallel to the ruby. Because the ruby laser has only a three level transition process, there are long periods of time between population inversion. This is an intrinsic property for every three level solid state laser. It is possible to overcome this problem by using a solid state lasing medium containing four levels, which are capable of participating in the laser action [24]. The photons capable of providing laser light will be produced between the second and third energy levels. Since this population inversion will be able to occur at faster rates, there is less wasted energy.

The ruby solid state laser is operated in a PW mode. This is necessary because of the length of time required between pulses of energy.

#### **2.1.2.2 Nd: Yag Laser**

Next to  $\text{CO}_2$  laser, Nd:Yag is the most widely used laser for material processing. In this solid state laser, Neodymium are impurity ions and yttrium aluminum garnet (YAG) is the host material. YAG has the chemical composition  $\text{Y}_3\text{Al}_5\text{O}_{12}$ . YAG is the best commercially available crystalline laser host. It offers low values of threshold and high values of gain. It's hardness (8.5 on the Moh's scale) allows for good optical polishing characteristics. It has high thermal conductivity; over ten times that of glass. This is one of the most important features.

The energy level diagram of the neodymium ion in YAG is shown in figure 4. This energy level diagram is mainly characteristics of the neodymium ions. There is some shift with

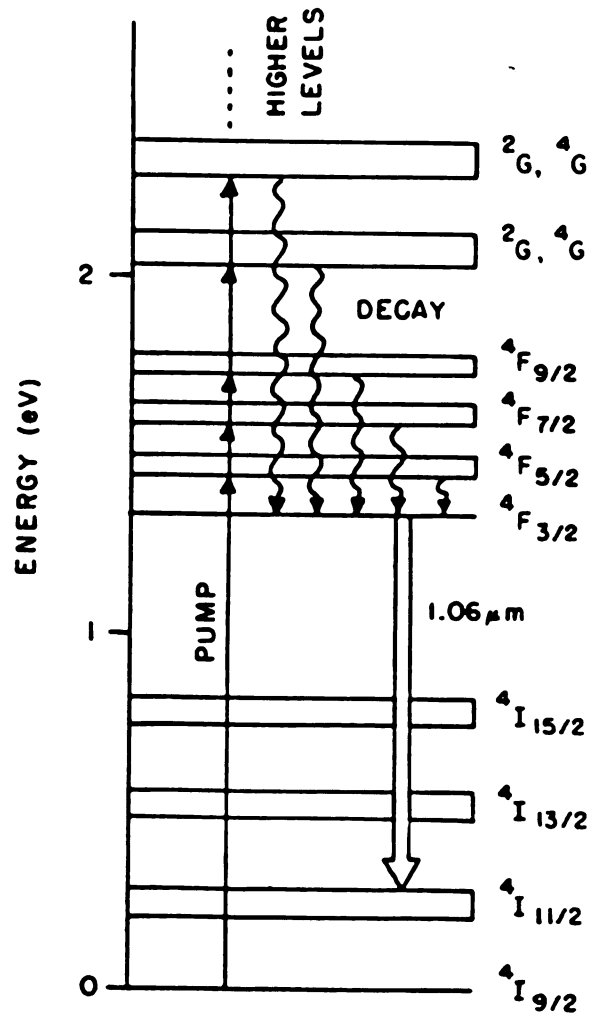
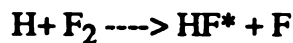


Figure 4. Energy levels of the Nd ion. [ 25]

varying host materials. As shown in figure 4, Nd:Yag is a four level laser system. The laser transition is between the  ${}^4F_{3/2}$  and the  ${}^4I_{11/2}$  level. Nd:Yag lasers may be used in three modes; namely continuous, repetitively pulsed, and continuous pulsed.

### 2.1.3 Chemical Lasers

Chemical lasers depend on chemical transition to obtain emission. Chemical lasers offer the desirable characteristic of possible operation without an electrical input. The population inversion is produced by the excitation energy produced in the chemical reaction. All the energy required for laser operation should be produced in the chemical reaction. One of the leading examples of the chemical laser can be represented by the set of reactions:



In the first reaction, a free fluorine atom is required to initiate the reaction. The excited  $HF^*$  molecules, produced in this reaction is an excited state which can be the upper level of the laser transition. The third reaction above indicates the transition to the lower laser state, which is not populated by the chemical reaction. This is accompanied by emission of light energy,  $h\nu$ . Thus, the population inversion is produced automatically whenever the chemicals react and yield some excited state molecules as the end products. Some electrical energy may be required for initiation, that is, for production of the original free atoms, but once the reaction has begun, further free atoms are produced and these reactions may continue cyclically. The most common chemical laser systems used are:  $D_2-F_2-CO_2$  at  $10.6 \mu\text{m}$  and HF and DF over the range of  $2.6-5.0 \mu\text{m}$  wavelengths.

### 2.1.4 Semiconductor Lasers

A forward biased p-n junction serves as the active medium for this type of lasers. The most commonly employed semiconductor material for lasers is gallium arsenide [26]. In semiconductor lasers, the energy level involved in the lasing action are characteristic of the entire crystalline lattice in contrast to ruby laser where the radiative transitions (that produce lasing) are characteristics of discrete atomic energy levels of the impurity. An energy band diagram of a p-n junction is shown schematically in figure 5. As shown in the figure 5, the bands in the region of the junction undergoes an energy shift. The electronic states are filled up to the Fermi level ( $E_F$ ). Thus there will be electrons in the conduction band in the n-type material and there will be holes at the top of the valence band in the p-type materials.

When a forward bias is applied to the junction, barrier voltage is reduced, as shown in figure 5b. There will be a partial overlap between the regions where electrons are present in the conduction band, and where holes are present in the valence band. This narrow region near the junction, thus has a population inversion. There are filled electronic states lying at energies above empty electronic states. In this region, radiative recombination can occur, with electrons falling across the gap and recombining with holes. The energy difference is emitted as radiation. Because of the population inversion, amplification by stimulated emission occurs.

In order for laser operation to occur, one particular inversion must be great enough so that optical gain exceeds optical loss. Thus the current density through the junction must exceed minimum value. This threshold value of current density scales as approximately as the cube of the operating temperature, between 77 and 300<sup>0</sup> K. Thus GaAs semiconductor laser are often operated at liquid nitrogen temperature, although they may be operated at room temperature with increased current density.

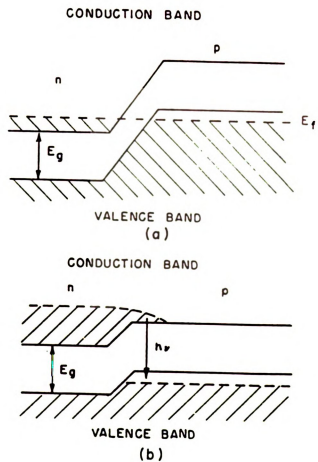


Figure 5. Barrier voltage for a p-n junction in a semiconductor [26]  
(a) is without a forward bias and  
(b) is with a forward bias.

## **2.2 Laser Process Parameters**

The effectiveness of any laser surface treatment depends on the various laser process parameters. The major process variables for laser surface treatment include the following:

- 1) Incident laser beam power;
- 2) Incident laser beam diameter;
- 3) Absorptivity of the material;
- 4) Traverse speed of the laser beam across the substrate surface; and
- 5) Other parameters such as: shielding gases and depth of focus with respect to substrate.

### **2.2.1 Laser Power**

The depth of the laser affected zone is controlled by the laser power density. Laser power density, in turn is controlled by incident beam power and beam diameter at the surface of the sample. Exactly at the focal point of a focusing lens, the incident beam diameter is the minimum possible by that lens (diffraction limited) and hence power density is maximum at that location for a fixed power level. As the sample surface moves away from the focal plane, towards the lens or away from it, incident beam diameter increases proportionately. Hence the power density at the surface of sample is dependent on its position with respect to focal plane.

Generally for constant beam diameter, penetration increases with the increasing power. Locke et al [27] reported that penetration increases almost linearly with incident beam power. Courtney and Steen [28] formulated empirically (while laser hardening EN 8 steel) that the depth of hardening is closely correlated with the parameter  $P/(D.V)^{1/2}$  where P is laser power, D is beam diameter, V is traverse speed.

The beam power is usually measured by calorimetric techniques using either air or water cooled calorimeters. Air cooled devices are restricted to lower powers than those cooled by water. Measurements can be made either by directing the total beam into a calorimeter, or by sampling a known fraction of the beam.

Solid state lasers can use Q-switching methods to increase peak power [29]. Various Q-switching methods are active and passive optical modulation and mechanical methods. These optical switches are placed in the cavity (optical), in various ways, schematically shown in figure 6.

In the initial Q-switched lasers, mechanical methods were used, where one of the cavity mirrors was simply replaced by a rotating prism or mirror. The mechanical Q-switches had the disadvantage of producing a laser beam, whose spatial profile changed with time. In the modern Q-switched lasers, active optical methods such as Kerr [30] and Pockel's cell [31] and passive optical methods such as liquid and solid saturable absorber are being employed. Kerr and Pockels cells are based on the principle that the refractive index of a solid crystal or liquid medium changes strongly under the influence of an applied electric field.

In liquid and solid saturable absorber, the absorber remains opaque to the laser in the first phase of pumping. Then, at a certain laser flux threshold, it becomes totally transparent. To obtain high peak powers, the saturable absorber is most commonly used [32].

### **2.2.2 Laser Beam Diameter and Intensity Distribution**

The beam diameter is important in laser surface treatment, since the focused beam diameter

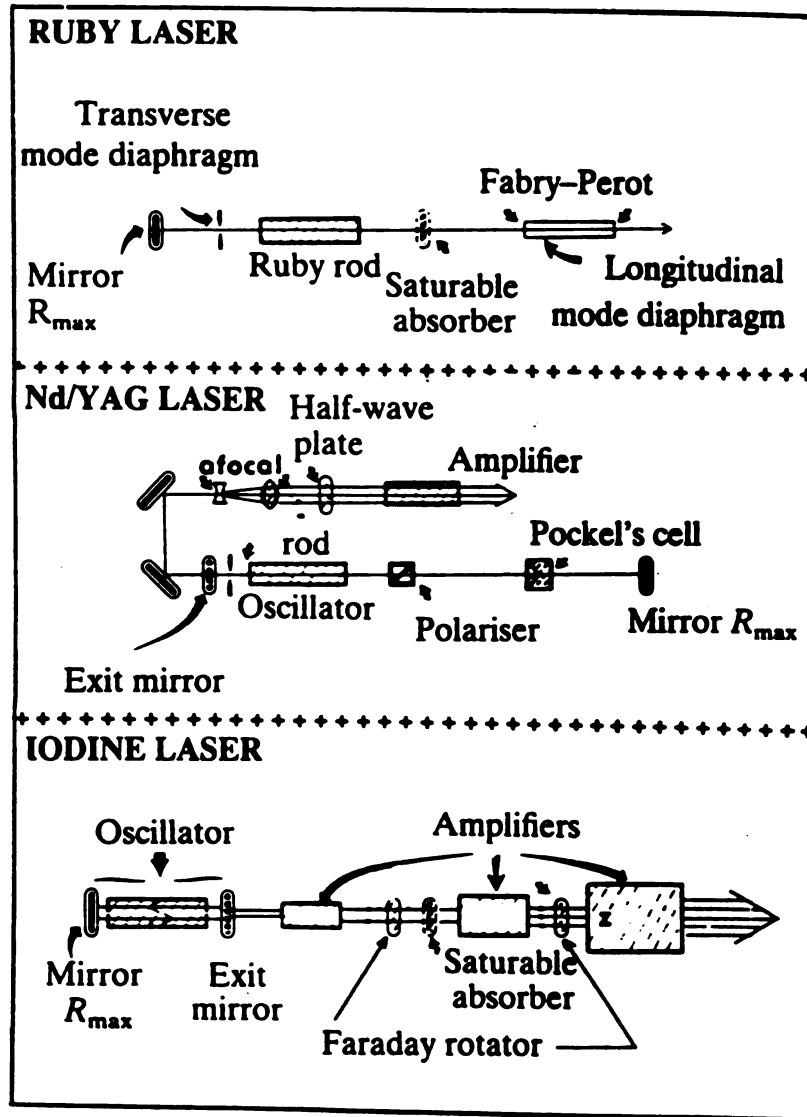


Figure 6. Different Q-switching types and their applications. [24]

and depth of focus quantify the energy in the focused region. The unfocused beam diameter is defined by the optical resonator. The intensity distribution within the beam is a function both of the resonator and the relative alignment of the optical components. Although the focused beam is important for laser processing, it is very difficult to measure high power laser beams. This is partly due to the definition of what is to be measured. A gaussian beam diameter may be defined as the diameter where the power has dropped to  $1/e^2$  or  $1/e$  of the central value. The beam diameter defined on the basis of  $1/e^2$  of the central value contains more than 80% of the total power whereas the power contained for  $1/e$  beam definition is slightly over 60%. Many techniques have been employed to measure the beam diameter and intensity profile. Heating or charring sensitive materials such as wood, firebricks and asbestos compounds are the simplest methods for looking at the profiles of an unfocused or partially focused beam. These techniques give an indication of beam diameter and symmetry. It is, however, a technique, where the affected area, and hence the measured beam diameter depends on both power and exposure. It is therefore more suitable for comparative measurements [34]. Measurements made by vaporizing acrylic materials are also subjected to reservations; however more information can be obtained than with heating or charring because of the possibility of the vaporizing a deep region in the acrylic and hence making a 3-dimension print. Again this technique is more relative than absolute. One of the better methods for the measurement of beam diameter is the photon drag detector [35].

The diffraction limited spot size at the focal point of a laser beam can be calculated on the basis of the diffraction theory of light. Assuming no aberration is formed by the laser, beam diameter ( $D_b$ ) can be given by following expression [36]

$$D_b = \frac{(244\lambda f) (2m + 1)^{1/2}}{D} \quad (\text{EQ 2.2.2.1})$$

where  $\lambda$  is wavelength of the laser; 'f' is the focal length of lens, 'D' is the diameter of the

unfocused laser beam; and 'm' is the number of oscillating modes

From the above equation, it is obvious that decreasing  $f/D$  ratio will decrease the  $D_b$ . However smaller values of  $m$  will also give the smaller beam diameter. Although the expression above for beam diameter is flawless, in practice the diameter is smaller than the one calculated by the above expression. This is due to the aberrations formed by the focussing optics.

Unlike laser welding or cutting, a wider beam with uniform intensity distribution is preferred for laser surface treatment and laser surface alloying, as opposed to a highly focussed high peak power, low order mode gaussian beam ( $TEM_{00}$ ). This is because the uniform intensity distribution generates uniform case depth. If the surface treatment area is wider, requiring overlapping of beam run, it may cause problem of back tempering. A broader beam covers the large area with relatively small back tempering.

There are different methods of beam manipulation that can be used to obtain a broad beam with uniform intensity distribution. Figure 7 shows some of the methods, which are used to produce suitable beam patterns at the workpiece. The beam integrator consists of a focussing mirror with several segments of individual mirror focussed on the same focal plane. The greatest advantage of this system is that it can start with a beam of any spatial distribution and convert it into a uniform intensity beam of the required size. The rastering of a finely focussed beam to cover a larger area (figure 7b) is another technique. Here two mirrors are vibrated at a very high frequency to create the required pattern. Both these techniques ultimately produce a rectangular beam pattern with uniform intensity. The most recent method of forming a square or rectangular beam is to use a device known as an optical integrator. This device, shown in figure 7c, is an array of flat mirrors mounted on a spherical surface placed to intercept the output laser beam. Each mirror forms an image of the part of the output beam that it intercepts, and all of the images from the array will be formed in the same position. In this way, the output beam is reshaped to form the desired

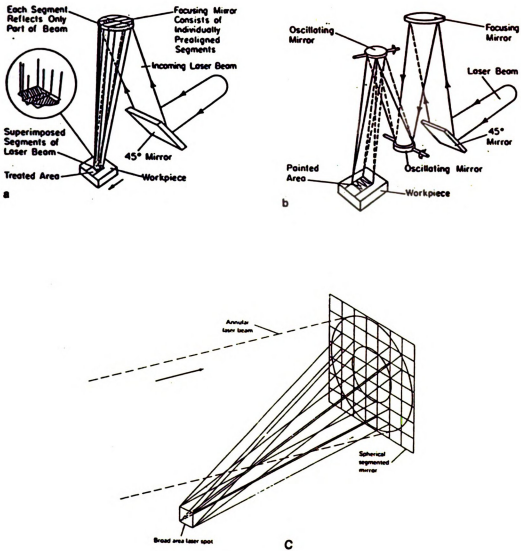


Figure 7. Beam manipulation techniques:  
 (a) segmented mirror system [33],  
 (b) two-axis vibrator system [33] and  
 (c) optical integrator. [12]

square or rectangular spot in the focal plane of the integrator, having uniform power density over the illuminated area on the workpiece surface. Both scanning optics and integrator optics form beams that can be redirected by flat mirrors or refocused by appropriately curved mirrors.

### 2.2.3 Absorptivity

The efficiency of laser heat treatment depends on the absorption of laser energy by the work piece. Any heat transfer calculation for laser processing is based on the absorbed laser energy. The infrared absorption of metal largely depends on conductive absorption by free electrons. Therefore, absorptivity is a function of the electrical resistivity of the substrate material. Arata et al.[37] measured the absorptivity of polished surfaces of various materials and concluded that absorptivity is proportional to the square root of the electrical resistivity. This agrees closely with the following expression: [37]

$$A = 112.2 (\rho_r)^{1/2} \quad (\text{EQ 2.2.3.1})$$

where A is absorptivity; and  $\rho_r$  is electrical resistivity.

A temperature dependent relationship between the electrical resistivity and emissivity of the metal was derived by Bramson [38]. Bramson's formula can be used for theoretical calculation of the absorptivity from the electrical resistivity. However such a calculation will be valid only for metals heated in vacuum without a surface oxide layer. The presence of an oxide layer will increase the absorptivity. The relationship between the emissivity and the electrical resistivity of a substrate, for perpendicular incidence of radiation of long wavelength, derived by Branson [38] is,

$$\epsilon_\lambda(T) = 0.365 \left( \frac{\rho_r(T)}{\lambda} \right)^{1/2} - 0.667 \frac{\rho_r(T)}{\lambda} + 0.006 \left( \frac{\rho_r(T)}{\lambda} \right)^{3/2} \quad (\text{EQ 2.2.3.2})$$

Where  $\rho_r(T)$  is the electrical resistivity at absolute temperature  $T$  expressed in  $\Omega\text{cm}$ .  $\epsilon_\lambda(T)$  is the emissivity of the substrate at  $T$   $^{\circ}\text{C}$  temperature for radiation having a wavelength of  $\lambda$ .

The value of absorptivity is a function of optical properties of the materials such as surface finish, the temperature, and the wavelength of the laser light. Generally the absorption decreases, as one goes to longer wavelength radiation, higher electrical conductivity, and smoother surface of the metal. This can be expressed mathematically as below:[163]

$$A = \frac{c}{R} \quad (\text{EQ 2.2.3.3})$$

$$R = \left( \frac{n_1 - n_2}{n_1 + n_2} \right)^2 \quad (\text{EQ 2.2.3.4})$$

where 'A' is absorptivity; 'c' is constant of proportionality; 'R' is reflectance;  $n_2$  and  $n_1$  are the refractive indices of the substrate material and incidence medium respectively. For conducting or absorbing dielectric materials,  $n_2$  is a complex number and the square in above expression for R is an absolute square. The magnitude of the refractive index for good conductors (metals) is proportional to  $(s/(2\pi\mu f))^{1/2}$  where  $s$  is electrical conductivity,  $\mu$  is the magnetic permeability, and  $f$  is the frequency of light. Consequently metals like gold, copper and aluminum have high reflectance, that increase with decreasing frequency of radiation (hence increasing wavelength), as compared to ferrous alloys.

Figure 8 shows schematically the absorptivity of iron as a function of wavelength and temperature. The reflectivity at lower temperature is high. In the region of melting point, metal can absorb much higher amounts of laser energy. Although metals are poor absorbers of infra-red energy at room temperature, above a certain threshold (approximately  $10^6 - 10^7 \text{ w/cm}^2$ ) energy transfer via the "key hole" leads to much higher effective absorptivity. It absorbs nearly the total amount of incident energy [40].

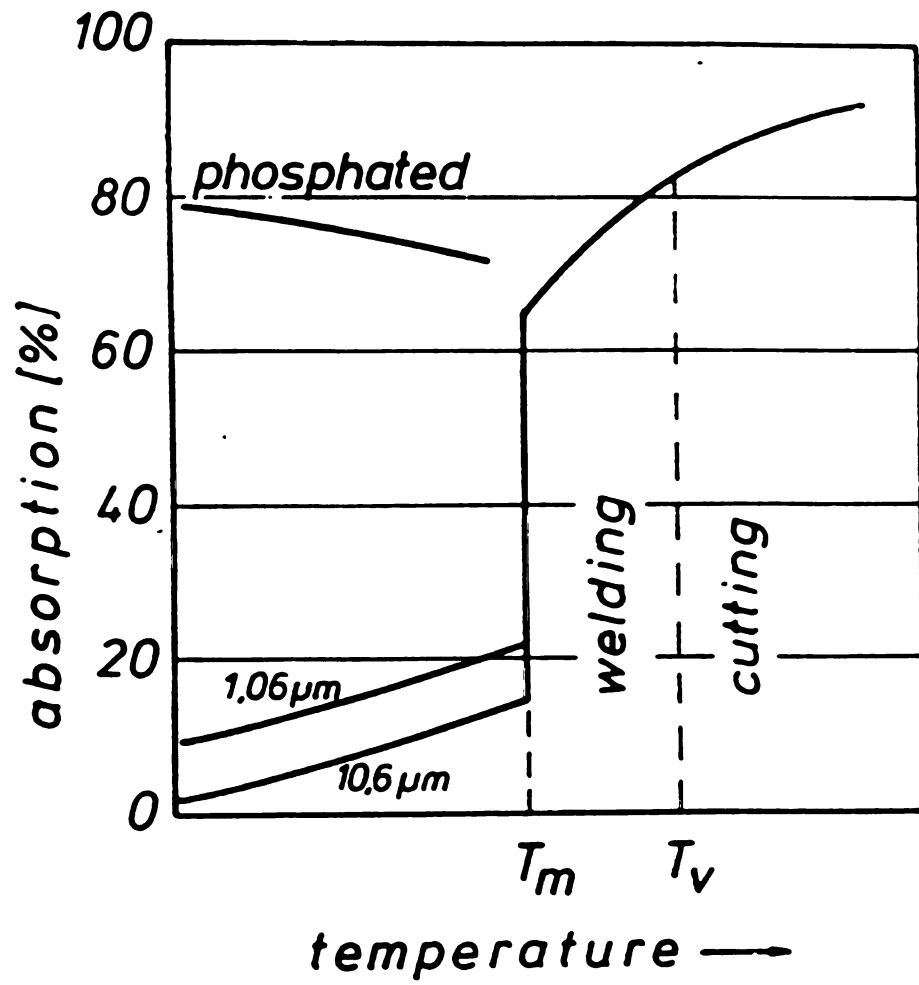


Figure 8. Absorption of laser light in iron as a function of wavelength and temperature. [166]

Absorptivity can be increased by the use of some absorbent coatings[ 33]. The most commonly used absorbent coatings are colloidal graphite, manganese phosphate, zinc phosphate, and black paint. A mixture of sodium and potassium silicate is also known to produce very high absorptivity. Nonetheless, exact absorptivity of any of these coatings is a matter of debate. Arata[41] quoted 50-90% absorptivity for phosphate coating without melting the substrate, whereas Trafford et al [42] quoted a value around 70-80% for no melting situations depending on the traverse speed. For colloidal graphite coating Trafford et. al. reported a value around 70% for colloidal graphite coating.

#### **2.2.4 Traverse Speed**

Traverse speed determines the laser interaction time with specimen surface. It is inversely proportional to the depth of hardening as shown in figure 9. The correlation of penetration depth with laser welding speed is discussed by Duley[43 ] and Locke et. al.[27 ]. Figure 10 shows the variation of penetration depth versus weld speed for 304 stainless steel. Increasing efficiency tends to be obtained at high velocity, since low incident power is lost by conduction into the workpiece [45,46].

#### **2.2.5 Shielding Gas**

The plasma produced during laser welding absorbs and scatters the laser beam. It is necessary, therefore to remove the plasma. The plasma of this type can be removed by supplying a shielding gas such as He. In addition to removing the plasma, shielding gas also protects the surface from oxidation. The effect of the composition of shielding gas on depth of penetration was studied by Seaman [47]. Figure 11 shows the comparison of effectiveness of various gases as shielding gas during laser welding. From figure 11 it can be seen that

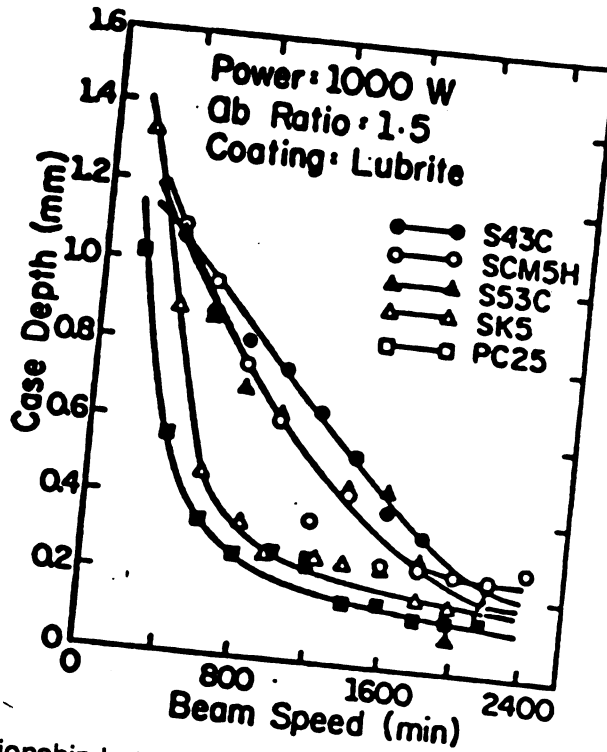


Figure 9. Relationship between the traversal speed and case depth in various materials. [33]

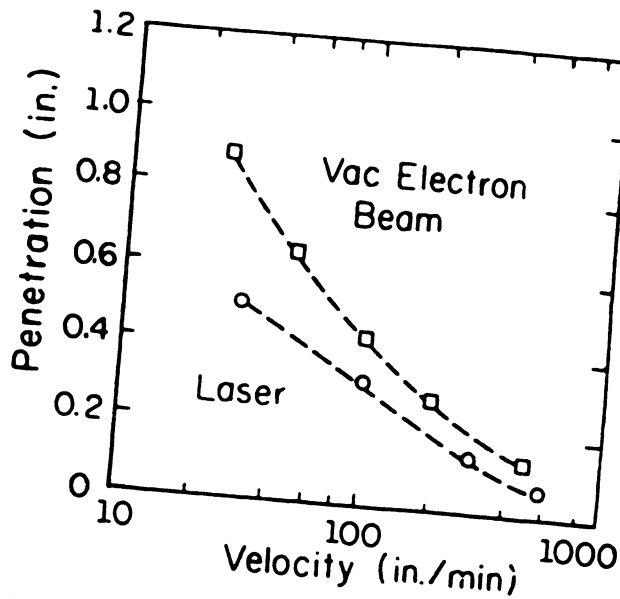


Figure 10. Weld penetration versus weld speed for 304 steel welded with a 10 kW CO<sub>2</sub> laser. [27]

Helium, as shielding gas, serves best for maximum penetration depth as compared to argon or air. Helium gas was found to improve transmission whereas argon caused severe beam blockage[47]. This is probably due to the lower ionization potential of argon as compared to that of helium. This hypothesis is further substantiated by the data from the addition of 1% hydrogen to helium as shielding gas. Since hydrogen has even higher ionization potential than helium, the hydrogen-helium mixture improves the transmission of the beam.

The ionization potential of the shielding gas is not the only consideration in choosing one for laser materials processing, especially at higher speeds. This is because gases with higher ionization potential have lower atomic numbers and lower masses. Thus lighter gases are less effective in displacing air from laser material interaction area, in the short time available in high speed welding. Heavier gases are better able to displace air in a short time. Therefore, a mixture of heavier and lighter gases will result in optimum penetration[36]. Figure 12 shows that, as speed increases, the improvement resulting from the addition of small amount of argon to helium (10% argon-90% helium) becomes more noticeable.

### **2.3. Laser Surface Treatment**

Erosion, wear and corrosion play an important role in determining the effective life of most of metallic structures. All of above three phenomena occur at the surface of parts. Wear resistance and corrosion of surface can be improved by various means such as, organic coatings or painting, designing the entire part with a wear resistant material, and cladding, metallizing or surface alloying. While coating or painting can provide a protection (at least temporarily) against corrosion, they have very little effect, if any, in improving mechanical properties of the surface. The second option, i. e., designing the entire structure with a high strength and wear resistant metal or alloy, is economically and strategically

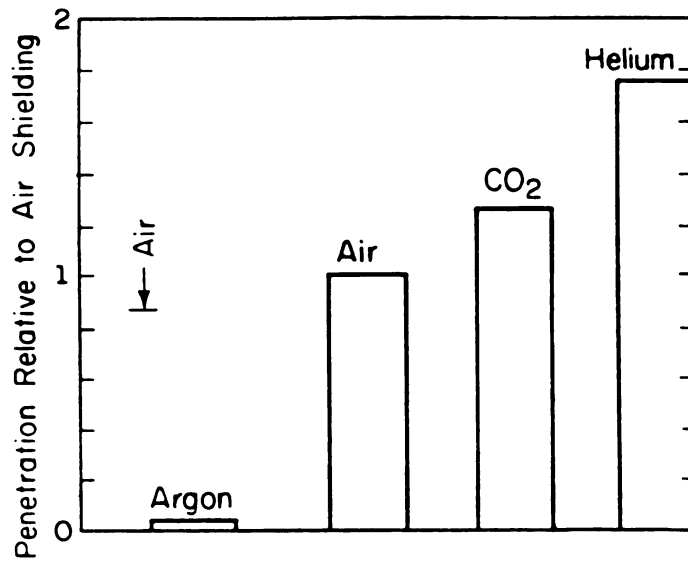


Figure 11. Achievement of welds in different gases. [47]

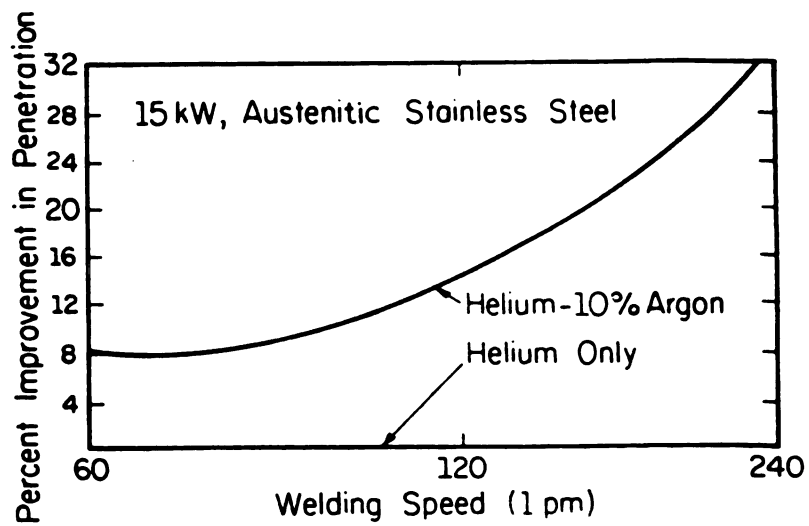


Figure 12. Blanketing effect of an addition of 10% argon to a helium shielding gas. [47]

unrealistic in most cases. Thus improvement of the surface properties by cladding or metallizing is a more realistic approach. It is in this area that laser surface treatment has the most potential. Laser surface treatments can be of various kinds such as those involving heating, melting or shocking. Figure 13 shows various laser surface treatments. Operation regimes for various laser surface treatments, currently used are illustrated in Figure 14.

The low power density processes such as transformation hardening [50], annealing, and grain refining [51] rely on surface heating without surface melting. Processes which rely on surface melting [53] require higher power density to overcome the conduction heat losses. Such processes include simple surface melting to achieve greater homogenization or very rapid self quench processes as in laser glazing [55] for the formation of metallic glasses in certain alloys. The melting processes also include those where a material is added either with a view to mixing into the melt pool as in surface alloying [54] or with a view to fusing on a thin surface melt as in cladding [57,58]. Laser shocking [59,75,76] involves the impingement of a very short pulse laser of high intensity, which sends mechanical shock waves through the material (generated by fast heating rate), resulting in surface hardening similar to shot peening. This last process of laser shock hardening has so far been little explored, but may eventually find a few special cases where it could compete industrially.

Most of the laser surface treatments ideally require uniform power density, unlike welding and cutting where a focused beam is preferred. But in practice, a defocussed gaussian beam ( $TEM_{00}$ ), which has a maximum power density at its centre, or  $TEM_{10}$  which has maximum power density at outer portions of the beam, can be used for surface treatment. A more complex beam handling system can be utilized to give a uniform power density [60], but this usually is reflected in higher cost optical components, together with less flexibility.

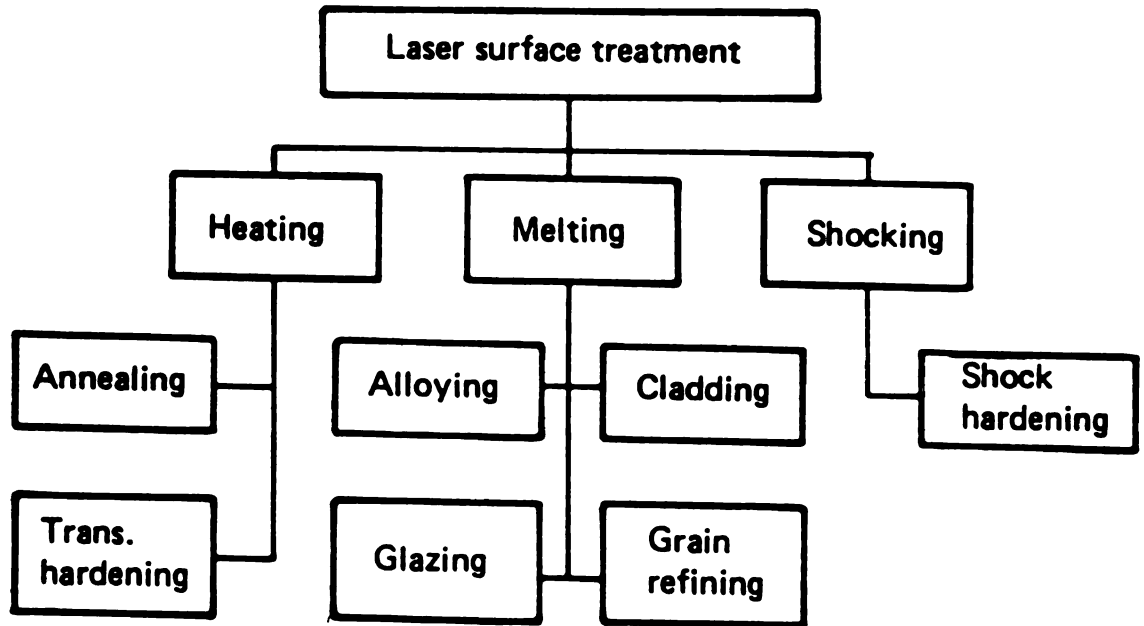


Figure 13. Methods of laser surface treatment of materials. [48]

10<sup>10</sup>  
10<sup>9</sup>  
10<sup>8</sup>  
10<sup>7</sup>  
10<sup>6</sup>  
10<sup>5</sup>  
10<sup>4</sup>  
10<sup>3</sup>  
10<sup>2</sup>  
10<sup>1</sup>  
POWER DENSITY — W/CM<sup>2</sup>

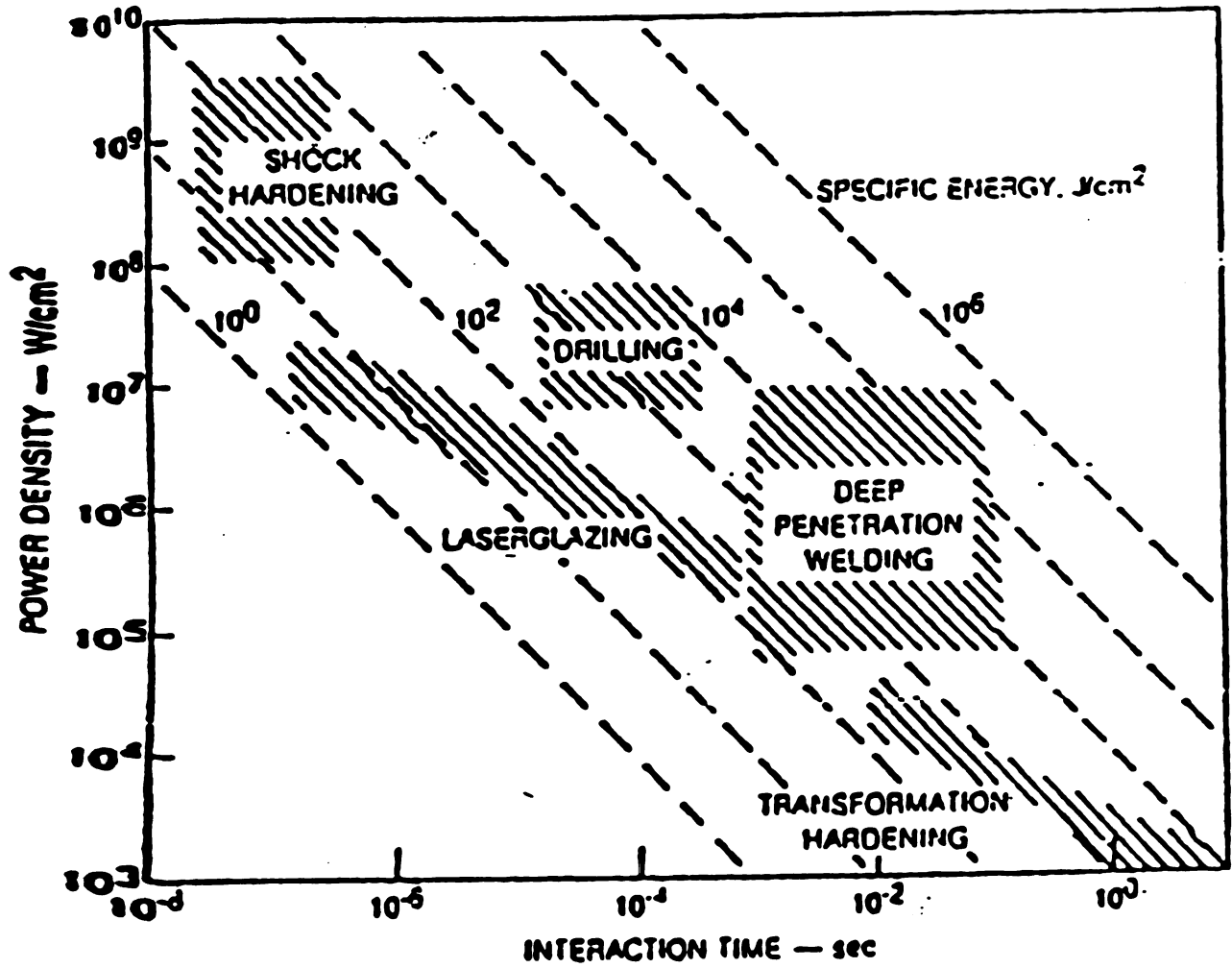


Figure 14. Operational regimes for various laser materials processing techniques [49].

### **2.3.1 Laser Surface Alloying**

**Laser surface alloying is a material processing method, which utilizes the high power density available from focused laser source to melt metal coating and a portion of the underlying substrate. Since the melting occurs in a very short time and only at the surface, the bulk of the material remains cool, thus serving as an infinite heat sink. Large temperature gradients exist across the boundary between the melted surface region and the underlying cold substrate. This results in rapid self-quenching and resolidification. Quench rate as high as  $10^{11} \text{ KS}^{-1}$  and concomitant resolidification velocity of  $20 \text{ ms}^{-1}$  has already been achieved [61]. What makes surface alloying both attractive and interesting is the wide variety of chemical and microstructural states that can be retained because of the rapid quench from the liquid state. The types of microstructures observed include extended solid solutions, metastable crystalline phases and metallic glasses.**

**Laser surface alloying of iron based metal or alloys will be described in detail in the section dealing with laser surface treatment of steel. In this section surface alloying of only non-ferrous metal or alloys has been outlined.**

**Most of the Laser surface alloying (LSA) studies have been carried out on the technically important elements (or alloys of) Al, Cu, Ni and Ti. Among these there are relative advantages and disadvantages from the standpoint of ease of laser processing, thermophysical constants and post-treatment analysis. For example, high purity Cu, and Al have very high thermal conductivity and thermal diffusivity. This, in combination with high reflectance, make it more difficult to melt these metals. On the other hand, larger conductivity and diffusivity will result in more efficient quenching. The lower thermal conductivity and diffusivity of Ni and Ti make it much easier to laser processing them.**

If sufficiently high cooling rates are achieved then both epitaxial regrowth and crystalline nucleation from the melt may be suppressed and a metallic glass may result. Continuous, pulsed (ms), Q-switched(ns), and mode-locked (ps) lasers have been used with the intent of retaining the amorphous surface layer of melt puddles. Both multiphase crystalline substrates and multilayered thin films have been used to provide melts with required compositions.

Lin and co-workers [66,67] have reported using the picosecond output of a mode-locked Nd:Yag laser to make amorphous thin film multilayer structures of Ni-Nb[66] and Mo-Ni, Mo-Co, and Nb-Co binary systems [67]. In the Ni-Nb system the glass forming range was determined to cover the range 23-82 at% Ni with supersaturated fcc and bcc solid solutions outside of the glass forming region. The authors point out that the glass formation range in the Ni - Nb system, when produced by conventional splat - cooling method [68], is only 40-70 at. % Ni. In the case of Mo- Ni system reported studies were performed at three compositions 30, 50, and 60 at. % Ni. In all instances amorphization took place as a result of laser alloying and melt quenching of the homogeneous liquid. Lin et al. [67] found, in case of the 30 at. % Ni sample some bcc microcrystallites at the edge of the melt spot. They pointed out that the laser fluence is spatially gaussian, and may produce only a partially melted region around the perimeter of the spot, thus providing a site for epitaxial growth.

Bonora et al. [69,70] reported the successful production of an amorphous layer, while melting Aluminium with a 15ns Q-switched ruby laser. He found that the this amorphous aluminium layer significantly improved electrochemical corrosion behaviour of the treated specimens. Another example of corrosion resistant behaviour of laser treated surface is the recent work on the Pd-Ti system. Commercial available bulk alloys of Ti, containing fractions of a percent Pd, are widely used by chemical processing industries. Protection against the reducing- acid environments is required only at the metal/corrosive interface, rather

than throughout bulk, hence surface alloying appears to be reasonable approach, particularly to save cost in reduced consumption of Pd. Surface alloying of Ti with Pd has been accomplished by thermal solid-state diffusion of thin Pd-electroplates [71] and by laser alloying [72]. Laser surface alloying of Pd in Ti offers several advantages over thermal diffusion. The thermal diffusion (solid state) suffers from concentration irregularities [71] associated with block or grain boundaries. The rapid diffusion and intermixing associated with laser melting has been shown, to produce homogeneous surface alloyed regions. Normally the long times at elevated temperatures associated with furnace diffusion require an inert atmosphere to protect Ti from embrittlement by oxygen, nitrogen or hydrogen. The reduced time, required during Q-switched laser alloying, enables the processing to be done in air. Another advantage of laser processing, over furnace treatment, is the smaller distortion caused during processing.

### 2.3.1.1 Alloy Deposition Systems

Deposition methods may be broadly classified as predeposition (laying powder on substrate, in a separate step before the laser treatment) or codeposition (injection of powder into the melt at the time of laser treatment). The very thin films (less than 500 nm) used, when surface alloying with a Q-switched laser pulses, are invariably put down with predeposition methods such as vacuum evaporation [62] or ion implantation. Thicker predeposited films are more commonly electroplated [61] or sprayed [63]. The ideal predeposited film would be of uniform thickness, be low in porosity, possess a clean substrate/film interface, and have an optically clean surface.

The codeposition method is more popular in laser surface alloying, because it implies single step processing and allows better automation and control. Codeposition method includes the particle injection directly into the laser melts [64] and wire feeding [65]

The o

man

po

### **2.3.2 Laser Cladding**

The objective in laser cladding is to fuse an alloy on to the surface of a substrate with the minimum of dilution. As in surface alloying, cladding can be done by either preplacing a powder on the substrate, or injecting the powder into the laser generated melt pool. In pre-  
place powder cladding, described by Powell [57] the laser sends a melt wave through the powder bed. Since the powder bed has a low thermal conductivity, the pool is almost thermally insulated until it reaches the substrate surface. At that moment it will freeze back forming only a solid/liquid bond, which is relatively weak compared to a full fusion bond. In injected powder cladding [58], the powder in an inert gas stream, is injected into the laser generated melt pool as illustrated in figure 15. The leading edge of the melt pool will incorporate the substrate. Particles arriving in this area will be solid. If the leading edge of the substrate is also solid then the particle will not stick and cladding will not occur. If however the leading edge is molten then the particles will stick and will melt instantaneously and thus forming a fusion bond. The level of dilution is controlled by the powder feed rate determining the size of the substrate leading edge.

The first industrial use of laser in cladding was done by investigators in Rolls Royce [73] in 1981. They clad turbine blade shroud interlocks on the RB211 engine. Since then many companies are applying or considering applying this process. Eboo [74] lists the laser cladding activities in table 2.1.

### **2.3.3 Laser Glazing**

The laser glazing involves melting a thin layer of metal, using high laser power density, and short interaction time (high traverse speed). Rapid surface melting, which allows almost

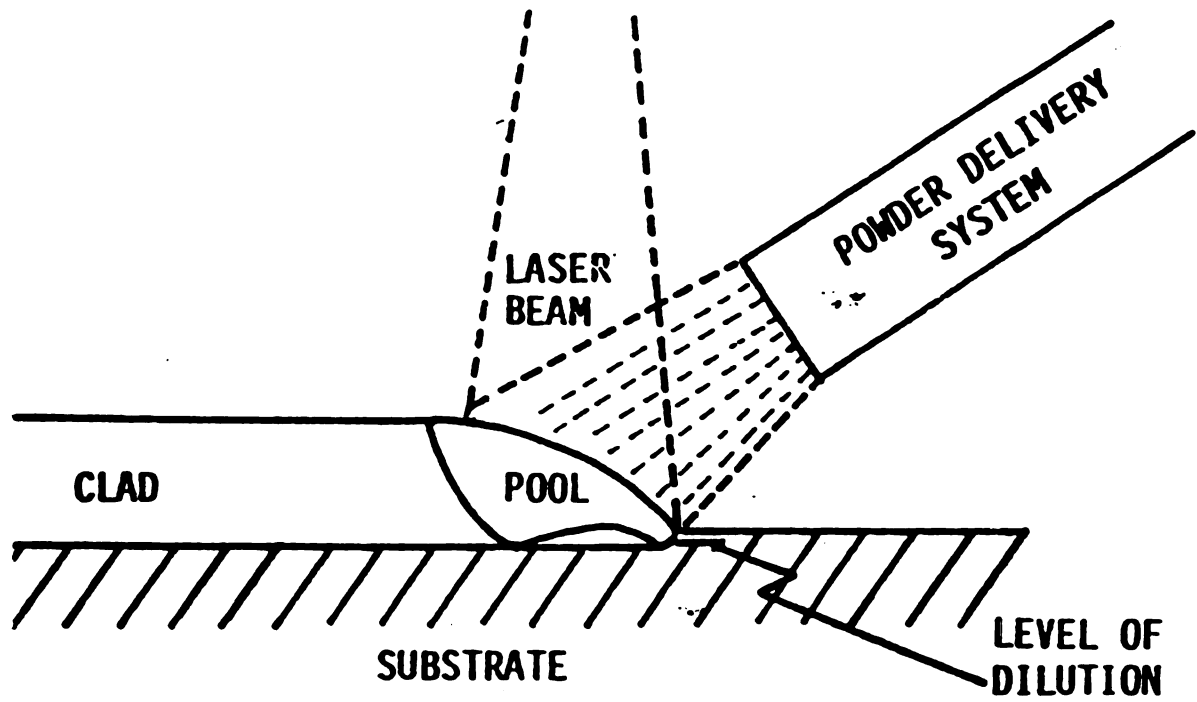


Figure 15. Laser cladding with blown powder. [48]

**Table 1. Laser cladding activities[74]****Production stage**

<b>Company</b>	<b>Component</b>	<b>Comments</b>
<b>Rolls Royce</b>	turbine blade shroud interlock	triballoy/nimonic powder feed
<b>Pratt &amp; Whitney</b>	turbine blade	PWA 694/nimonic preplaced chips
<b>General Electric</b>	proprietary	reverse machining with Ti powder feed

**Pilot Demonstration Stage**

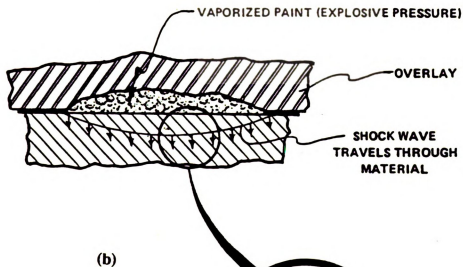
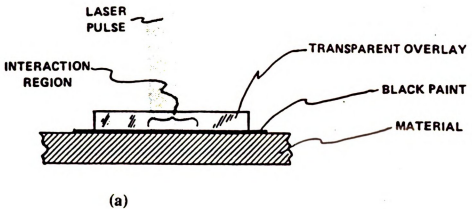
<b>Company</b>	<b>Component</b>	<b>Comments</b>
<b>Combustion Eng.</b>	offshore drilling & production parts valve components boiler firewall	stellites, Colmonoys powder feed
<b>FIAT</b>	valve stem valve seat aluminium block	Cr C, Cr, Ni, Mo/C.I
<b>General Motors</b>	automotive	cast iron system
<b>Rockwell</b>	aerospace	T-800, Stellites powder feed
<b>Westinghouse</b>	turbine blades	stellites, Colmonoys preplaced beds

negligible amount of thermal energy to pass into the base metal, produces sharp temperature gradients between the solid and the liquid. The sharp temperature gradient leads to very rapid quenching ( $\sim 10^6 \text{ }^\circ\text{C s}^{-1}$ ) [55] of melt, producing a fine homogeneous structure. This structure is often harder and more corrosion resistant than the untreated part [55]. Superficial melting and high traverse speed results in little thermal penetration, thus the laser glazing can be used quite close to thermally sensitive components.

#### **2.3.4 Laser Shock Hardening**

In this technique the effect of high amplitude stress waves on microstructure and stress state of metal and alloys is exploited [75]. When an intense laser beam strikes the metal surface ( $\sim$ pulsed duration of  $20\text{-}40 \times 10^{-9}$  s), the surface layer is instantly vaporized. The rapidly expanding high temperature vapor exerts pressure on the target surface, which then propagates into the specimen as a stress wave. High surface pressures are obtained by placing on the target an overlay, transparent to the laser beam, such as fused quartz or water, which continues the 'blow off' material between it and the specimen surface for the duration of the laser pulse. The rapid thermal expansion of this confined vapor produces the enhanced peak pressures necessary for plastic deformation of the target specimen, which causes dislocations to nucleate, in situ, in the submicrostructure of the materials. The altered dislocation density increases the hardness and tensile strength of material [59,76]. The specimen surface can be protected, and peak pressures be further modified by applying a thin layer of black paint between the transparent overlay and the specimen surface as shown in figure 16. Black paint serves in two ways; protects the surface and causes explosive pressure by getting vaporized, when struck by the laser.

#### **2.4 Laser Heat Treatment of Steel**



HARDNESS INCREASES

YIELD STRENGTH INCREASES

MICROSTRUCTURE SHOWS HIGH DISLOCATION DENSITY



Figure 16. The laser shock process [90]

(a) laser shocking setup

(b) Schematic of the vaporization and pressure reactions at the metal surface during laser irradiation.

Laser surface treatment of steel can be classified into three categories; transformation hardening, laser alloying, and cladding of steels.

#### **2.4.1 Transformation Hardening**

In laser transformation hardening [ 78,79] the temperature of steel specimen surface is raised to austenitic temperature with laser beam. The sharp temperature gradient between the surface and core causes sharp cooling rate, thereby producing martensite. The cooling rate has to exceed the critical cooling rate for martensite formation. Ashby and Easterling [50] transformation hardened a Nb microalloyed steel, a medium carbon steel and low carbon steel. They found steels, with a carbon content of below about 0.1 wt. %, do not respond to transformation hardening. The low carbon content of martensite gives a hardness, which is hardly changed by the process. Shiue and Chen [81] hardened the surface of AISI 4340 steel specimens. By TEM studies they found that microstructures in the hardened zone consisted of mainly lath and twinned martensites. In the transition zone of laser treated specimens, they found partially dissolved carbides with austenite envelopes, and/or austenite islands in a matrix of martensite. The limitation of laser transformation hardening was pointed out by Sandven[12], after his experience with laser transformation hardening of cast iron with a high content of free ferrite. He pointed out that under certain conditions, laser processing may occur too rapidly to allow for complete carbon diffusion. This problem is obviously most prevalent where carbon distribution in the starting material is non-uniform, such as in coarse pearlite structures, structures containing proeutectoid cementite, spheroidized materials, and cast iron, particularly cast iron with a high content of free ferrite. Cast iron housing bores, in Saginaw Steering Gear Div. have been successfully hardened [2]. Crystalline coating of manganese phosphate was used as a preprocessing coating to improve absorption of laser beam.

In laser hardening, the surface coating plays a very important role. Normally a polished iron surface will reflect a large percentage of the 10.6 micron laser energy. Absorption can be enhanced to more than 90% by coating the surface with a thin layer of a high absorbing materials, such as lamp black [3], zinc phosphosphate [10], cuprous oxide, and polycrystalline tungsten [1].

A comprehensive study of laser transformation hardening of nodular cast iron by Gnana-muthu et. al [63] has investigated fatigue behavior and the wear rate of laser hardened samples. They observed significant increase in the fatigue life of samples. Wear rate was decreased by a factor of ~2.5 when compared to untreated steel. Laser hardening has been recently used to treat cylinder liners for diesel engines [82,91] and to treat camshaft [83].

#### **2.4.2 Laser Alloying and Cladding of Steel**

Principles of alloying technique has been described in surface alloying section. Extensive work has been done on laser steel [84-88]. Molian [85] has investigated the compositional uniformity of electroplated Cr alloyed into high purity iron, as function of CW-CO<sub>2</sub> laser incident power density. Figure 17 shows the Cr concentration depth profile. This particular melt stripe may be physically described as semicircular and has a uniform 38% Cr over the entire 250 micron melt depth. Molian and Wood [87] have also reported the results of microstructural investigation on Cr surface alloys produced with CW-CO<sub>2</sub> laser in both low carbon (.2% C) steel [89] and high purity Iron [86-87]. The laser surface alloyed microstructure consisted of austenite in a dislocated ferritic matrix. The austenite contained a high density of twins.

Moore et. al. [84] have described the surface alloying of Cr into low carbon (.18% C) steel. Cr was electroplated to thickness of 15  $\mu$ m and melting was accomplished with CW-CO<sub>2</sub>

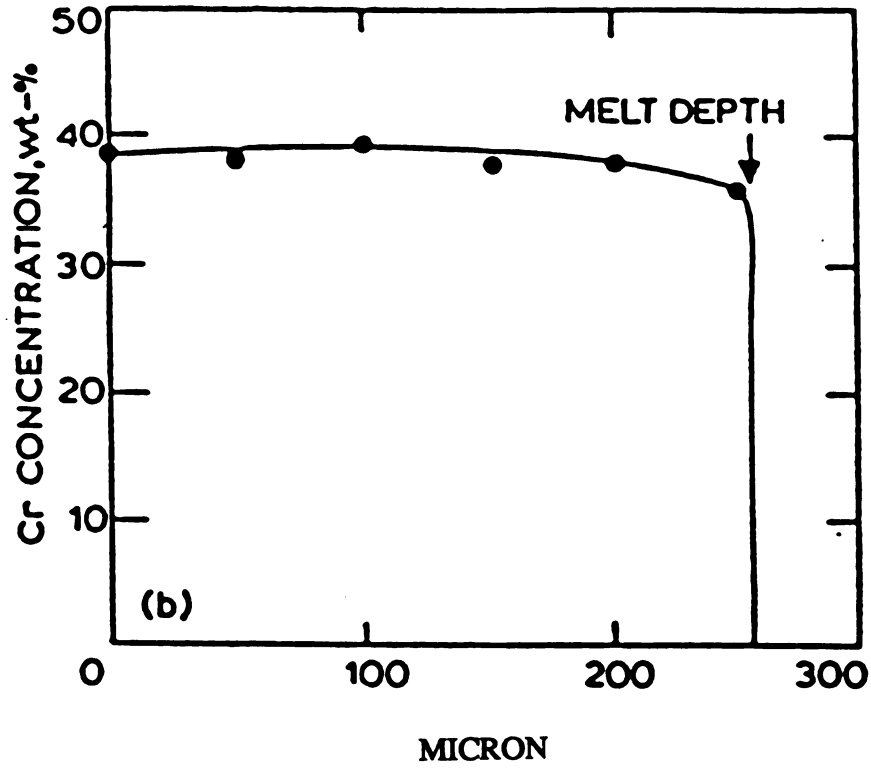


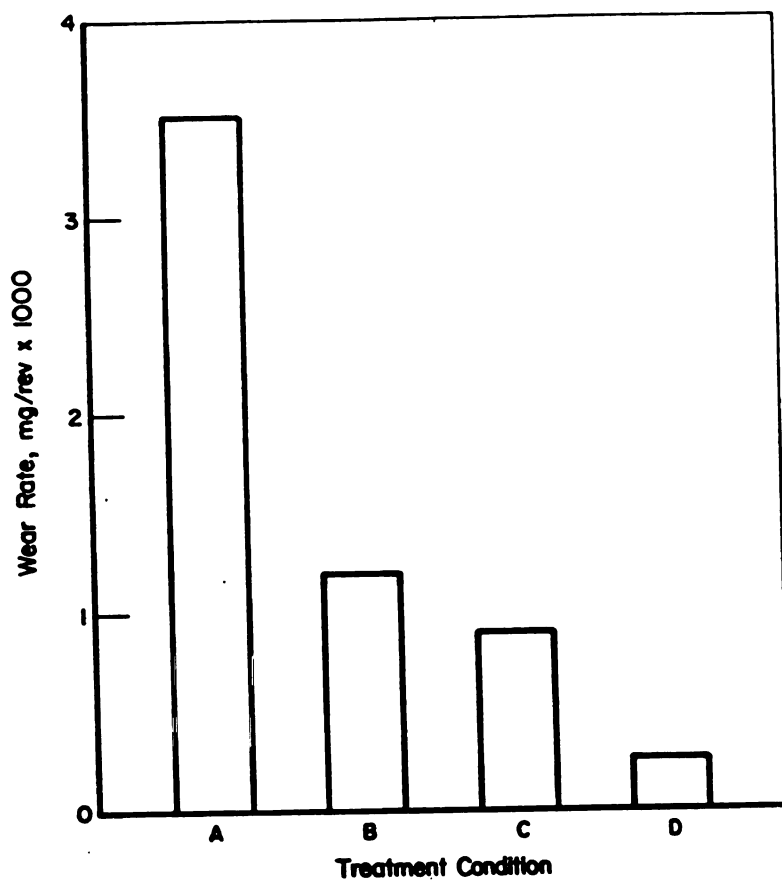
Figure 17. Cr concentration profile on cross-section of melt trail (250 micron) for Cr on Iron scanned with CW CO<sub>2</sub> laser. [96]

laser over a wide range of traverse speeds and incident power density. Since one of the main interests in laser surface alloying of iron based substrate is the production of a stainless steel surface equivalent, these investigators have sought to characterize the electrochemical behavior of laser surface alloyed steels. Laser surface alloyed (stainless steel) were subjected to anodic polarization scans in deaerated .1M Na<sub>2</sub>SO<sub>4</sub> solution. With increasing Cr content, both the critical current density and passive current density decreases. Under above environment AISI 1018 steel, without the Cr surface alloying, gets corroded at all anodic potential.

Glaeser et. al [90] observed that laser treated, TiB<sub>2</sub> plasma coated, AISI A-6 steel (.7 % C; 2.0% Mn; .3% Si; 1.0% Cr; 1.3% Mo) surfaces displayed significant abrasion resistance, when compared with the hardened steel surface. A wide range of microstructures were obtained by controlling the energy input to TiB<sub>2</sub> plasma sprayed steels surfaces. Abrasion tests were performed on samples having three different microstructures described in figure 18. The wear resistance of laser treated TiB<sub>2</sub> coated AISI A-6 steel specimens were found, on the average, 3-4 time better than untreated steel (hardened A-6 tool steel). The fused TiB<sub>2</sub> coating attached to steel by a melt zone demonstrated a superior abrasion resistance to all other structures. It was about an order of magnitude better than the uncoated steel. Ayers et al. [92] laser surface alloyed 304 stainless steel by injecting fine particles of WC and TiC into a shallow laser melted zone. They found that the process of injecting wear resistant particles into a laser melted surface, is quite versatile, being applicable to a wide range of materials combinations.

## 2.5 Heat Transfer in Laser Surface Treatment

An accurate description of the temperature distribution that occurs on the surface of specimens, treated by laser, is essential for predicting distortion and stresses. In addition, a



A - Untreated Steel

B - TiB<sub>2</sub> Completely Dissolved in Steel

C - TiB<sub>2</sub> Partially Dissolved in Steel

D - TiB<sub>2</sub> Intact, Infused with Steel Matrix, Meltzone Bonding

Figure 18. Comparison of abrasive wear resistance of various laser treated structures, TiB<sub>2</sub> coated.

knowledge of the heating and cooling rates is useful in predicting metallurgical reactions and microstructural transformation in laser treated zone and heat affected zone. But accurate measurement of puddle temperature and cooling rates during laser welding are extremely difficult due to the large temperature gradients and cooling rates involved.

Hence a number of investigations [93-118] have addressed the heat flow problems in a semi infinite substrate material subjected to stationary and moving high intensity heat fluxes. Perhaps the earliest attempt to calculate the heat flow in above situation was by Carslaw in 1921 [93]. A simple analytical solution was derived to describe the thermal response of a semi infinite work piece subjected to a stationary, instantaneous point heat source. Of significantly greater practical applications, however was the work of Rosenthal in 1941 [94]. Numerous investigators have tried either to modify mathematically or to verify experimentally Rosenthal's analytical solution. Being the pioneer work, Rosenthal model is presented below in detail.

The major assumptions made by Rosenthal were (1) a point heat source, (2) no heat of fusion and no melting, (3) no surface heat losses due to convection and radiation, and (4) constant thermal properties. Under the above assumptions the differential equation of heat at a point is written as follows:[94]

$$\frac{\delta^2 T}{\delta X^2} + \frac{\delta^2 T}{\delta Y^2} + \frac{\delta^2 T}{\delta Z^2} = \frac{2\lambda \delta T}{\delta t} \quad (\text{EQ 2.5.1})$$

Where the thermal diffusivity  $= 1/2 \lambda = K/\rho C_p$ ,  $t$  is time and  $X, Y, Z$  are the coordinates of the point.

Above equation has been derived for a stationary source of heat. The laser material processing requires a source moving with a constant velocity. It is known from experiments

that when such treatment is performed over a sufficient length of time, a state is reached in the material, which is called “quasi-stationary”; the temperature distribution due to the moving heat source is stationary with respect to the moving heat source. Figure 19 shows that the isotherms move at the same velocity as the heat source, and hence are stationary with regard to it. This knowledge enables the longitudinal ordinate of equation above to be transposed, thus

$$\epsilon = X - Vt \quad (\text{EQ 2.5.2})$$

Where  $V$ = Velocity of heat source;

$X$ =Longitudinal ordinate;

$\epsilon$  =Longitudinal ordinate with respect to moving heat source.

Performing the transposition, equation 2.5.1 becomes:

$$\frac{\delta^2 T}{\delta \epsilon^2} + \frac{\delta^2 T}{\delta Y^2} + \frac{\delta^2 T}{\delta Z^2} = \frac{2\lambda \delta T}{\delta t} - \frac{2\lambda V \delta T}{\delta \epsilon} \quad (\text{EQ 2.5.3})$$

But the new coordinate system has specified that the temperature is independent of time

(the isotherms are stationary with respect to the heat source), hence equation 2.5.3

becomes:

$$\frac{\delta^2 T}{\delta \epsilon^2} + \frac{\delta^2 T}{\delta Y^2} + \frac{\delta^2 T}{\delta Z^2} = -\frac{2\lambda V \delta T}{\delta \epsilon} \quad (\text{EQ 2.5.4})$$

The following assumptions are made for the solution of equation 2.5.4

- (1) The heat losses from the surface of plate are negligible,
- (2) The heat source is a point source,
- (3) The temperature at a far distance from the source of heat remain unchanged
- (4) and the physical properties of the material are constant.

With these assumptions, the analytical solution of Rosenthal to such a steady state (with

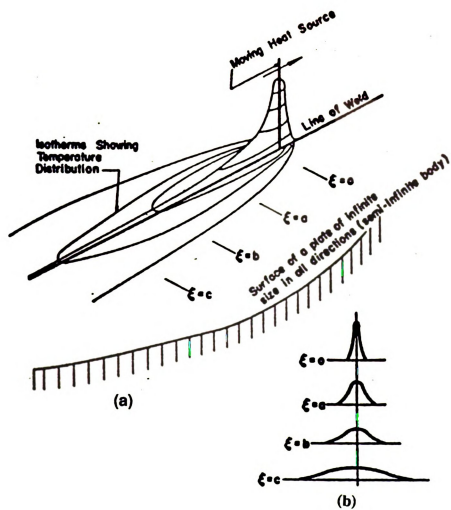


Figure 19. (a) Temperature distribution due to a moving source of heat. [95]  
 (b) Temperature distribution at cross-sections shown in (a).

respect to moving coordinate system), 2-dimensional heat flow equation can be given as follows:

$$T = T_o + \left(\frac{Q_p}{2\pi Kh}\right) e^{-\lambda V \epsilon} K_0(\lambda VR) \quad (\text{EQ 2.5.5})$$

Where  $R = \sqrt{\epsilon^2 + Y^2}$

$h$  = thickness of plate,

$K_0$  = modified Bessel function of second kind and zero order,

$Q_p$  = total heat transferred to workpiece per unit of time by point source,

$K$  = thermal conductivity, and

$T_o$  = initial temperature of plate

The graphical representation for the temperature distribution around heat source, based on equation 2.5.5 is provided in figure 20 [96]. A family of isotherms are developed around heat source. The rise of temperature in front of the heat source is steeper than the fall of temperature behind source. The points on the workpiece passing through maximum temperature at the same instance are located on a line (locus)  $n$ , (figure 20c&d), which is curved backwards. This is due to finite speed of heat flow in metals, which delays the occurrence of the maximum temperature in volume elements parallel to the direction of workpiece motion. The more distant the volume elements from the heat source, the greater the delay. For the same material with identical geometry, the speed of scanning effects mostly the shape of the isotherms. Higher the speed, more elongated are the isotherms and the more pronounced is the lag of the curve (figure 20 c & d).

Equation 2.5.5 is Rosenthal's solution for 2-Dimensional case. Analytical solution of Rosenthal to a steady state, 3-D heat flow problem is given by[97,98]

$$T = T_o + \frac{Q_p}{2\pi KR} e^{-(\epsilon + R) V \lambda} \quad (\text{EQ 2.5.6})$$

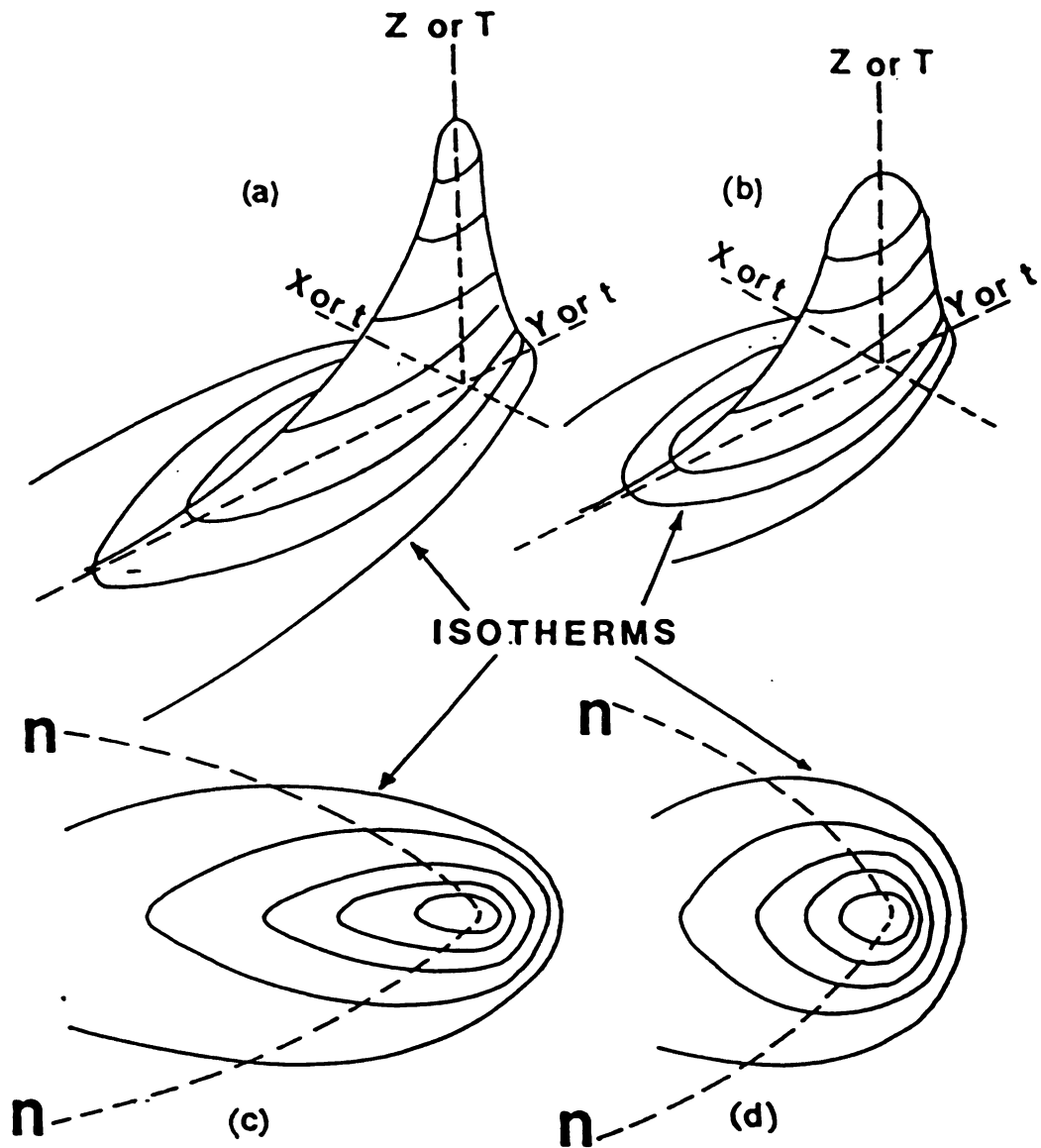


Figure 20. Schematic of temperature distribution around heat source. (a) and (b) are the representation in the form of a hill, (c) and (d) are the representation in topographic projection. Temperature distribution shown in (a) and (c) is in a plate treated with higher traversal speed whereas the temperature distribution in (b) and (d) is in a plate treated with comparatively slower traversal speed. [96]

where 'R' is the distance of heat source from the point of reference.

From Equation 2.5.5 and 2.5.6 Rosenthal obtained expressions for the center line cooling rate. Since this could be regarded as the representative of the fusion zone. For 2-D case the cooling rate is given by:

$$\frac{dT}{dt} = 2\pi K \rho C_p \left(\frac{Vg}{Q}\right)^2 (T_0 - T)^3 \quad (\text{EQ 2.5.7})$$

For 3-D case the cooling rate is given by:

$$\frac{dT}{dt} = \frac{2\pi K}{\rho C_p} \left(\frac{V}{Q}\right) (T - T_o)^2 \quad (\text{EQ 2.5.8})$$

Due to some of the rather unrealistic assumptions mentioned above, heat flow and solidification in a molten pool cannot be predicted, and poor agreement exists between calculated and experimental thermal history in heat affected area, immediately adjacent to molten pool. As a consequence, many investigators [99-108] have tried to modify Rosenthal's analytical solution. For example Swift-Hook [101] considered the temperature dependence of the thermal properties, Jhaveri [102] took into account the surface heat loss. Trivedi [103] considered the finite size of the heat source. However, due to the complex nature of the problem, the modified analytical solutions, so far have had rather limited success. Recently with the help of digital computers, numerical methods have been applied to the studies of heat flow in welding or laser processing. Numerical methods remove many of the limitations that apply to the analytical methods. For example:

- (1) the heat source does not have to be concentrated in point, line or plane;
- (2) the geometry of the workpiece may be taken into account;
- (3) physical properties of the substrate may be considered temperature dependent without much difficulty;

- (4) truncation error from series expansion of different functions associated with analytical solution is absent; and
- (5) the difficulty of application of the analytical solution of the heat flow equation to real boundary conditions eliminated.

Due to the above mentioned advantages, some of the numerical models have made significant contribution in modeling thermal behavior during welding or laser processing. Based on the measured shape of the weld pool, Pavelic [104] calculated the temperature distribution in a thin plate of steel, using the finite difference method (FDM). Freidman [105,106], on the other hand, used the finite element method (FEM) to calculate the temperature distribution in a thin plate, being welded. The heat conduction in the welding direction was neglected. More recently Sharier [107] employed the FDM method to calculate the unsteady heat flow during the fusion welding of thin tantalum sheets. The heat conduction in the welding direction was taken into account, which is an improvement over Friedman's study.

The 3-dimensional quasi steady state heat transfer model for laser welding, developed by Mazumder and Steen [46], and later modified by Chande and Mazumder [108] is the most practical model for laser welding application, reported to date. This model allows for temperature dependent thermo-physical properties, spatial distribution of the heat source, radiative heat losses, convective heat losses and latent heat of transformation.

## **2.6 Solidification During Laser Surface Treatment**

Not many people have tried to analyze the solidification during laser surface treatments involving melting; but the theoretical background can be related to that involved in welding process. Microstructure can be expressed in terms of grain and subgrain structures.

### 2.6.1 Grain Structure

The grain structure in the laser melted zone can strongly influence its susceptibility to solidification cracking. The grain structure of the fusion zone develops by epitaxial growth and competitive growth. In autogeneous welding, the liquid metal of the weld pool is in intimate contact with a substrate of identical composition (the unmelted part of the base metal). Therefore, grain growth initiates from the substrate at the fusion boundary and proceeds towards the weld centerline. Such a growth initiation process is called epitaxial growth (some time epitaxial nucleation) [120-121]. In this process, grain growth is initiated by arranging atoms from the liquid phase on the existing crystalline substrate, thereby extending it without altering the crystallographic orientation. The continuity of crystallographic orientation across the fusion boundary was first confirmed by Savage and Aronson[2] from Laue X-ray back-reflection studies.

Although the grain structure near the fusion boundary of fusion zone is dominated by the epitaxial growth mechanism; it is however, governed by the different mechanism known as competitive growth, in the bulk of the fusion zone. During solidification, grains tend to grow in the direction perpendicular to the solid/liquid interface, since this is the direction of the maximum temperature gradient and thus the maximum driving force for solidification. However, grains also have their own preferred direction of growth called the easy growth direction [119]; for example  $\langle 100 \rangle$  in face centered cubic (f.c.c) and body centered cubic (b.c.c) metals, and  $\langle 1010 \rangle$  in hexagonal closed packed (h.c.p) metals. Therefore, during solidification, grain with their easy growth direction parallel to the direction of the maximum temperature gradient will grow more easily and crowd out those other grains whose easy growth direction deviates significantly from the direction of the maximum temperature gradient, as shown schematically in figure 21.

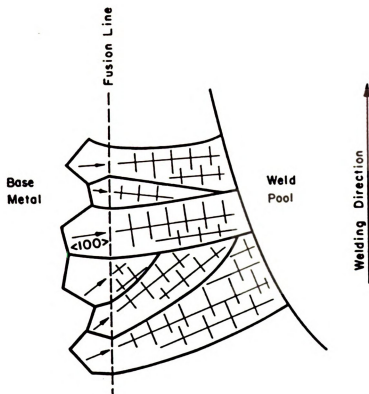


Figure 21. Competitive growth in the fusion zone. The arrows in the grains of the base metal indicate the easy growth direction, say  $\langle 100 \rangle$  in f. c. c or b. c. c metals. [122]

The experience gained from welding about the columnar grain structure [120,123], can be extended to fusion zone involved in laser surface melting. It has been observed that at high welding speed, the weld pool tends to be elongated (figure 22c), whereas at low welding speeds it tends to be nearly circular. In figure 22a, the columnar grains grow in the direction of the thermal gradient produced by the moving heat source. The grains grow epitaxially from the base metal towards the energy source. Because the direction of maximum temperature gradient is constantly changing from approximately  $90^{\circ}$  to the weld interface at position A to nearly parallel to the weld axis at position B, the grains must grow from the position A and continuously turn towards the position of the moving heat source.

The shape of the molten zone tends to become more elongated with increasing traverse speed. In figure 22b, the direction of maximum temperature gradient is perpendicular to the weld interface at position A and B, but because the molten pool is trailing a greater distance behind the heat source, the temperature gradient at position B is no longer strongly directed toward the heat source. Therefore, the columnar grains do not turn as much as in the case of a nearly circular pool.

Finally the molten pool takes on a tear drop shape at a faster traverse speed which is usually encountered during a commercial welding process. The pool is elongated so far behind the heat source that the direction of the maximum temperature gradient at position A and B in figure 22c have changed only slightly. As a result, the grains grow from the base metal and converge abruptly at the centerline of the pool with little change in direction. Pools that solidify in a tear drop shape have the poorest resistance to centerline hot cracking because low-melting constituents tend to segregate at the centerline.

### 2.6.2 Subgrain Structure



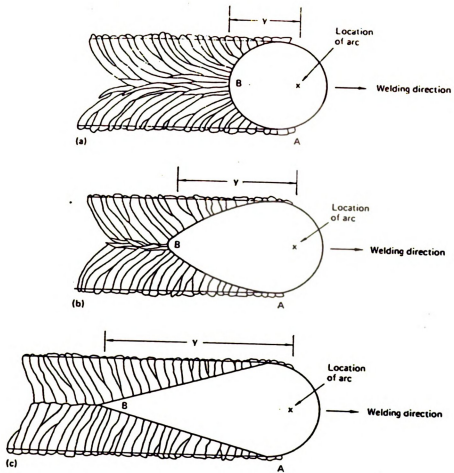


Figure 22. Comparison of weld pool shapes due to different scan speed, [164]  
(a) slow, (B) intermediate, and (c) fast.

Each fusion zone columnar grain contains a solidification substructure. Substructure can be planar, cellular, dendritic, and equiaxed dendritic, depending on the solidification conditions and the material system involved. The structure varies from the planar to equiaxed dendritic depending on the stability of the solid/liquid interface [124]. Many theories [124,127] have been proposed to quantitatively describe the break down of a planar solid/liquid interface during solidification. The constitutional supercooling theory by Chalmers et al. [126] seems to match closely to the experimental observations during solidification [128-132]. Constitutional supercooling theory will be considered in the rest of this section.

Figure 23 shows a portion of a binary phase diagram. The solid/liquid interface of an alloy (of composition  $C_0$ ) is assumed at temperature  $T^*$  at a certain moment during solidification. As shown in figure 23b, solidification takes place from left to right at a rate  $R$ . Because of the lower solubility of the solid phase (S), solute atoms are rejected into the liquid phase (L) during solidification, and consequently a solute enriched boundary layer is formed in front of the advancing solid/liquid interface, as shown in figure 23b. The composition profile in the liquid is  $C_1(X)$  and the compositions of the liquid and the solid at the interface are  $C_L^*$  and  $C_S^*$  respectively. With the help of the equilibrium liquidus temperature line of the phase diagram (defined as  $T_1 = f(C_1)$ ) in figure 23a, the equilibrium liquidus temperature profile in the liquid  $T_1(X)$  can be obtained, as shown in figure 23c. Assuming that the local equilibrium exists at the solid/liquid interface and that there is no diffusion in the solid phase, it can be shown [122] that the gradient of the equilibrium liquidus temperature profile at the interface is as follows:

$$\left. \frac{dT_1(X)}{dX} \right|_{X=0} = \frac{-Rm_l}{D_L} (C_L^* - C_S^*) \quad (\text{EQ 2.6.1})$$

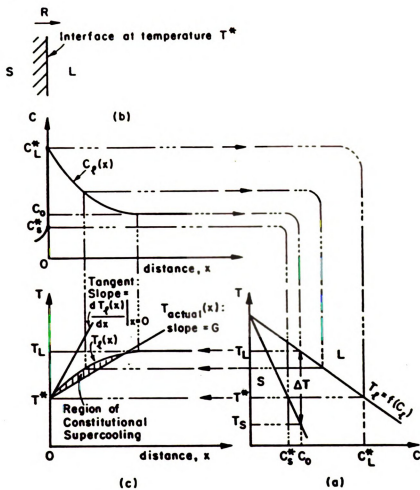


Figure 23. Constitutional supercooling in alloy solidification [133]  
 (a) phase diagram;  
 (b) solute-enriched layer in front of the solid/liquid interface;  
 (c) constitutional supercooling.

where  $m_l$  is the slope of the liquidus line of the phase diagram  $\left(\frac{dT_l}{dC_l}\right)$  and  $D_L$  is the diffusion coefficient of solute in the liquid.

If the actual temperature of the liquid near the solid/liquid interface,  $T_{\text{actual}}(X)$ , is such that its gradient,  $G$ , is less than  $\left.\frac{dT_l(X)}{dX}\right|_{X=0}$ , there exists in front of the solid/liquid interface, a region in which  $T_{\text{actual}}(X)$  is lower than the equilibrium liquidus temperature,  $T_l(X)$ , as shown by the shaded area of figure 23c. In other words, this region is constitutionally supercooled. To avoid constitutional supercooling and therefore to maintain a planar solid/liquid interface, the following criterion, should be met:

$$\frac{G}{R} \geq -\frac{m_l(C_L^* - C_S^*)}{D_L} \quad (\text{EQ 2.6.2})$$

In the above equation,  $C_L^*$  and  $C_S^*$  are related to each other by the equilibrium partition ratio  $k$ :

$$k = \frac{C_S^*}{C_L^*} \quad (\text{EQ 2.6.3})$$

Under the steady-state solidification, the composition of the solid at the solid/liquid interface becomes the composition of the bulk liquid:  $C_S^* = C_o$  and  $C_L^* = C_o/k$ . Therefore, Equation (2.6.2) becomes:

$$\frac{G}{R} \geq \frac{-m_l C_o (1 - k)}{k D_L} \quad (\text{EQ 2.6.4})$$

It is interesting to note that  $-m_l C_o \left(\frac{1}{k} - 1\right)$  is the equilibrium freezing range which is the difference between the equilibrium liquidus temperature,  $T_L$ , and the equilibrium solidus temperature,  $T_S$ , as can be seen in figure 23a. Equation (2.6.4) can be rewritten as follows:

$$\frac{G}{R} \geq \frac{\Delta T}{D_L} \quad (\text{EQ 2.6.5})$$

Where  $\Delta T$  is the equilibrium freezing range of the alloy, that is,  $T_L - T_S$ . The constitutional supercooling theory has been experimentally verified by many investigators [128-132]. In general, this theory predicts, fairly closely, the conditions required to initiate the breakdown of a planar interface in alloys with isotropic surface energy. Unfortunately, none of the present theories can predict quantitatively the transition from the cellular to the columnar dendritic mode of solidification or the transition from the columnar dendritic to the equiaxed dendritic mode. However, it has been found [128] that the greater the degree of constitutional supercooling (the smaller the ratio of  $G/R$ ), the greater the tendency for a given material to switch from the cellular to the dendritic mode of solidification. In fact, when  $G/R$  is very low, the region of constitutional supercooling is so wide that solid nuclei form in front of the advancing solid/liquid interface and grow into equiaxed dendrites, as solidification proceeds.

## 2.7 Thermal and Residual Stresses Involved in Surface Treatments

Thermal stresses generated during any surface treatment are very crucial. They can cause cracking in the surface treated zone during treatment or promote fracture of the surface treated part during service. They can also enhance fatigue fracture and stress corrosion cracking in weldments [134]. Thermal stresses are the transient stress, occurring during the surface treatment due to the non-uniform temperature change. Residual stresses, also referred to as internal stresses (reaction stresses, locked in stresses) are stresses that continue to exist in a body after the completion of the process (treatment) [135].

Residual stress at the surface of an object is of particular importance because most failures start there [136]. A stress field can cause a crack to propagate rapidly, but it can also squeeze a crack shut. If the surface stresses are tensile and tend to pull the material open,

they accelerate crack growth and assist in the destruction of the object. On the other hand, if the stresses are compressive, any small cracks opened by corrosion or local deformation do not grow as quickly as they otherwise would. They are literally forced closed by the compressive stress field.

Residual stresses in the surface heat treated part have been recognized and studied since 1950[137,138]. The residual stress issue, in case of welded structures, is an age old issue yet to be resolved completely. Residual stresses may occur during forging and shaping of metal parts by processes such as shearing, bending, machining, and grinding. Various heat treatments also give rise to variety of residual stress distributions in parts. In any of the above processes, the resultant overall residual stresses are superpositions of stresses such as quenching stresses, shrinkage stresses, and phase transformation stresses.

**(a) Quenching Residual Stresses:** Typically, these stresses are set up between surface layers and core of a part, during the cooling period of a process. These stresses are set up due to sharp temperature difference between the surface and the core during cooling, particularly in the case of thicker plates. Figure 24 shows the steps in which residual stress arise, during quenching of a slab. The edges of such a slab cool faster than the center. The thermal contraction associated with this drop in temperature gives rise to a mismatch between the edges and center of the ingot which would result in a longitudinal tensile stress (among other stresses) in the edges and longitudinal compressive stresses in the center (figure 24b). The low yield strength of the hot center, however, cannot withstand the action of the compressive stresses and the center shrinks plastically. When the center of the slab finally cools and contracts, the total contraction is greater than that suffered by the outer skin, since the center also shrank some by plastic flow, in addition to a contraction during cooling. The center will then be in tension and the edge will be in compression. These stresses will be maintained because the metal is now cold throughout the slab and the yield

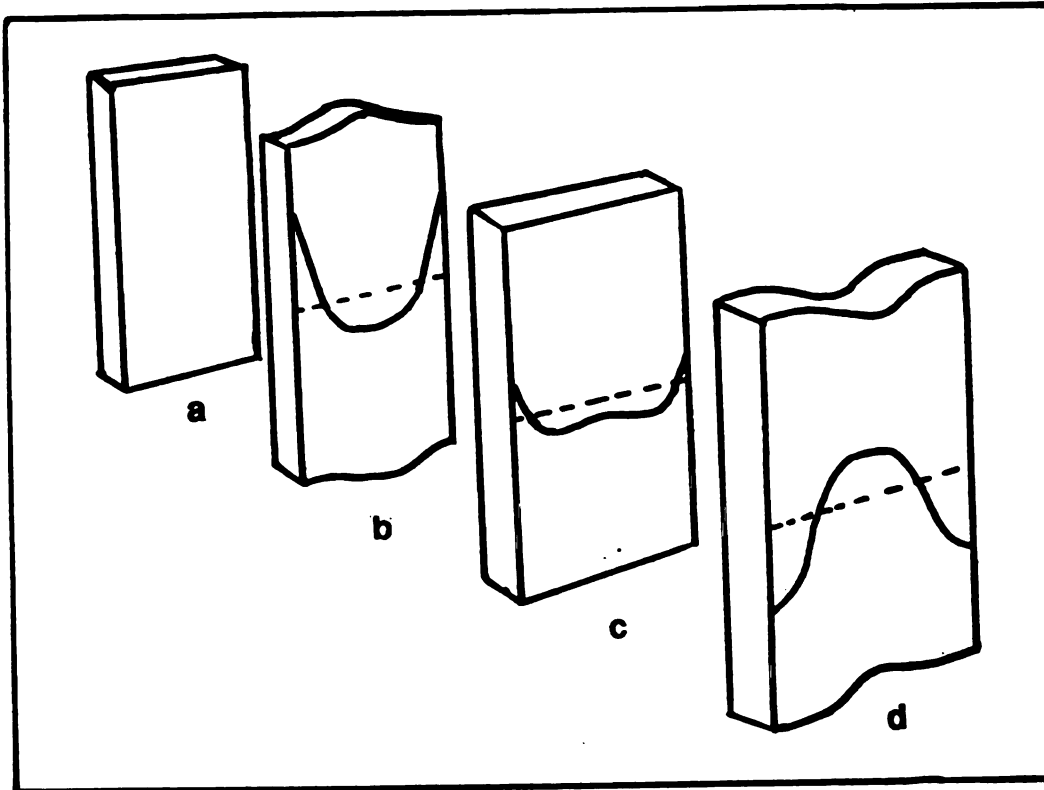
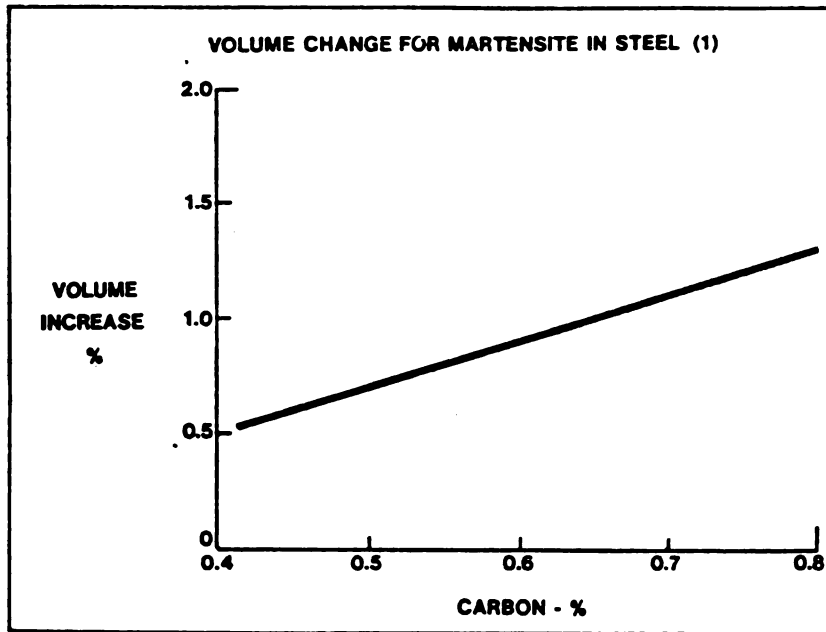


Figure 24. Crude representation of development of residual stresses in a cooling hot ingot. [137]

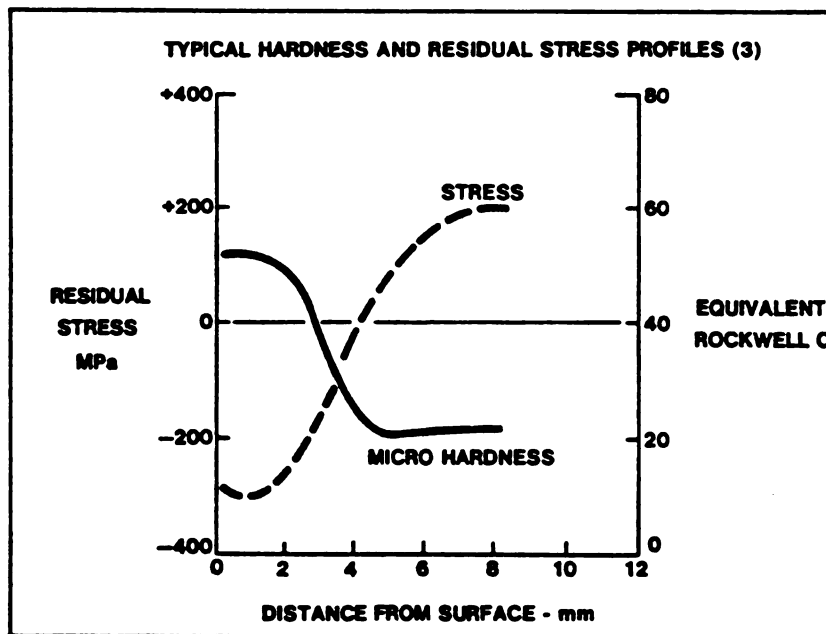
strength is high. Thus, in general, if quenching effects were solely responsible for the formation of residual stresses, compressive residual stresses would have to be anticipated in the surface layers (which attain room temperature at first) and tensile residual stresses in the core (which attains room temperature last).

**(b) Transformation Residual Stresses:** Phase transformations associated with a change in volume can give rise to residual stresses if surface of a section, which reached a high temperature, undergoes phase transformation during the course of cooling whilst the cold region around do not. In an induction hardened steel parts, a residual compressive stress is produced when a microstructure of lower density (martensite) is formed on the surface of a section while the non-hardened core remains essentially unchanged (figure 25) [139-141]. When the hardened material in the surface is constrained in its expansion in an elastic manner by the underlying core material, the result is a residual compressive stress at and near the surface. A fairly sharp stress transition to a tensile condition occurs in the vicinity of the hardness drop off between the hardened and the unhardened section (figure 25b).

**(c) Shrinkage Residual Stress:** An important source of residual stresses, which is present in all weld and in all surface treatments involving localized heat and melting, is the shrinkage of very hot zones, which is restrained by colder zones which shrink scarcely or not at all. Maximum possible residual stress would arise if the shrinkage could be accommodated purely elastically, but in reality plastic flow [140,142,143] occurs as a consequence of the shrinkage and the residual stress can only attain the yield point. In case of a fusion welded sheet [143], the constrained longitudinal shrinkage of the weld results in the longitudinal and transverse residual stress distribution along the weld line (y axis) and along a line perpendicular to the weld line (x axis) which are schematically shown in figure 26. The longitudinal residual stresses, i.e. the stress components parallel to the weld line are tensile stresses in the fusion zone and in the heat affected zone directly bordering on it. These are



(a)



(b)

Figure 25. (a) Volume change for martensite in steel;  
(b) Typical hardness and residual stress profiles. [139]

maintained in equilibrium by the compressive longitudinal stresses in zones farther from the center of the weld line ( $x$  axis). The longitudinal stress distribution along the weld line is responsible for the distribution of transverse strains represented schematically on the far left side of figure 26. This shows that the transverse strains are constraints along the length of the weld and thus, even if no external forces or restraints impede the transverse shrinkage, residual stresses must arise transverse to the weld. The distribution of these transverse residual stress is also schematically shown in figure 26.

A whole range of publication [144-147], particularly older ones, assume, based either on simple calculations or on experimental results obtained by mechanical methods, that the schematic representation in figure 26 can be considered as the basic stress pattern for welding processes or surface treatment involving melting. It should, however, be emphasized that in reality the interaction between shrinkage, quenching and phase transformations has been taken into account to predict the distribution of stresses precisely around a weld or surface melted zone.

### **2.7.1 Measurement of Residual Stresses**

Residual stresses are never measured directly. Residual stresses are, instead, measured indirectly through the strains that exist in a stressed metal. Residual strains can be measured by several methods [148-159]: destructive and non-destructive. Non-destructive methods include acoustic techniques and x-ray diffraction technique, where as destructive methods include methods such as the center hole method and the deflection method.

#### **2.7.1.1 Center Hole Method**

The center hole method is a semi-destructive method of measuring residual stress [154]. In

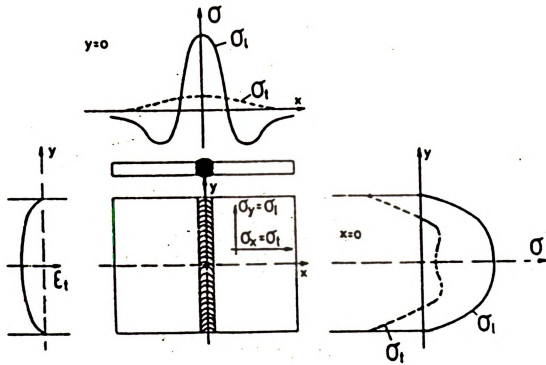


Figure 26. Distribution of longitudinal and transverse residual stresses and of transverse strains along the  $y$  and  $x$  axis in a single pass welding. [140]

this me  
ual stre  
The dri  
stresse  
gauges  
equatic

$$\sigma_{1,2} =$$

Where  
stress  
sette e  
strain.

A larg  
when  
The la  
comp  
hole t  
may b

27.1.

this method a strain gauge rosette (figure 27) is attached to the surface on which the residual stress will be measured. A hole is then drilled at the center of the strain-gauge rosette. The drilling causes a redistribution of stresses in the vicinity of the hole. The change in stresses causes a change in the internal strain distribution, which may be detected by the gauges. The change in strains can be related to the residual stresses in the material by the equations (elastic unloading assumed) [155,156]

$$\sigma_{1,2} = -\frac{E}{2k_1} \left( \frac{\varepsilon_1 + \varepsilon_2}{1 - \nu \frac{k_2}{k_1}} \mp \frac{1}{1 + \nu \frac{k_2}{k_1}} \left( (\varepsilon_1 - \varepsilon_2)^2 + (2\varepsilon_2 - (\varepsilon_1 + \varepsilon_3))^2 \right)^{1/2} \right) \quad (\text{EQ 2.7.1})$$

$$\alpha = -\frac{1}{2} \text{atan} \left( \frac{\varepsilon_1 - (2\varepsilon_2 + \varepsilon_3)}{\varepsilon_1 - \varepsilon_3} \right) \quad (\text{EQ 2.7.2})$$

Where  $k_1$  and  $k_2$  are constants obtained by calibration using a specimen free of internal stress but with a uniaxial stress applied to it;  $\lambda$  is the angle measured clockwise from rosette element 1 in figure 27 to the maximum principal stress.  $\varepsilon_1, \varepsilon_2, \varepsilon_3$  are the relaxed strains;  $\sigma_1, \sigma_2$  are the in-plane principal stresses, where  $\sigma_1 < \sigma_2$  and  $\nu$  is the Poisson ratio.

A large hole gives a greater sensitivity (larger values of  $\varepsilon_1, \varepsilon_2$  and  $\varepsilon_3$ ) than a small hole. when the center hole is formed with a drill, some strain is induced due to the machining. The larger the hole diameter, the greater this strain due to machining becomes. Thus a compromise has to be found between using a large hole for greater sensitivity and a small hole to minimize the machining strains. To minimize the machining strains, the drilling may be substituted by a stream of abrasive in a jet of air [1].

### 2.7.1.2 Curvature Method

Fig

T  
S  
K

Figure

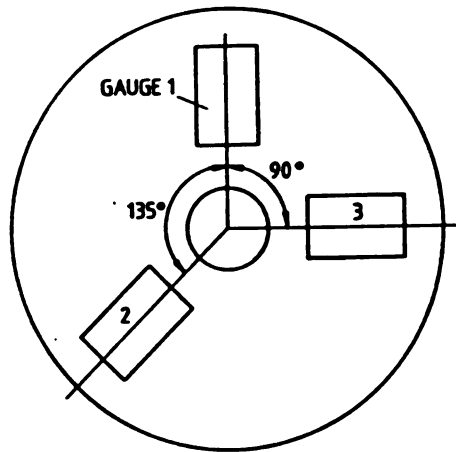


Figure 27.  $45^\circ$  rectangular rosette for residual stress measurement. [149]

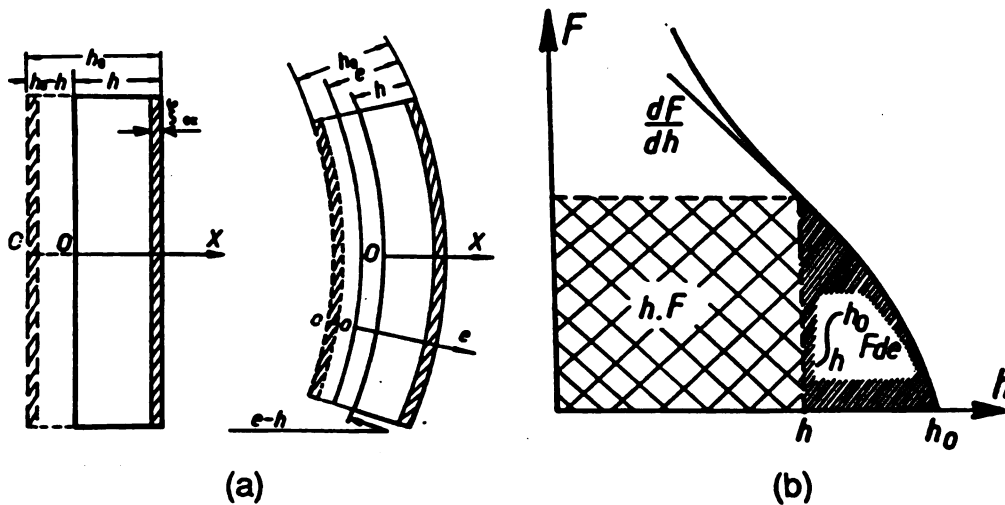


Figure 28. (a) Schematic of the sample, after a mechanical sputtering of one of its large faces, the symmetry is broken and the sample bends. (b) Variation of the sample curvature with the residual thickness  $h$ . [159]

The cu  
acting  
technic  
sive me  
imen is  
change  
suring  
to deta

Where  
residua  
The cu  
imens.  
tations  
no pra  
materi

2.7.1.3

There  
divide  
materi  
sure d

One n

The curvature method [158,159] is based on the fact that if stresses of different values are acting on the opposite sides of a thin strip, the resultant moment may bend the strip. The technique consists of measuring the curvature evolved in the specimen during a progressive mechanical (or chemical) polishing of one of its large faces. In the beginning the specimen is flat, but due to progressive polishing of one of its faces, the stress distribution changes, the sample bends in order to maintain equilibrium (figure 28). By accurately measuring the sample thickness and its curvature during the progressive polishing, it is possible to determine stress distribution by using the following equation [158]

$$\sigma(h) = \frac{E}{6} \left( h^2 \frac{dF}{dh} + \int_h^{h_0} F de + hF \right) \quad (\text{EQ 2.7.3})$$

Where 'E' is the elastic modulus of the sample; 'F' is the radius of curvature; 'h' is the residual thickness as shown in figure 28.

The curvature method is a fast emerging method for measuring residual stress in thin specimens. Both the curvature method and the center hole method, in general, have two limitations. First, they can not be used to determine the microscopic stresses because there is no practical means of measuring the changes in the dimensions of the separate phases of a material. Second, these methods are destructive in nature.

### 2.7.1.3 Non-Destructive Methods

There are several non destructive methods of measuring residual stresses. They can be subdivided into direct and indirect methods. The indirect methods deduce the stresses in the material from measurements of some property other than strain. The direct methods measure displacements and then use equations of elasticity to calculate strains and stresses.

One non destructive technique that is currently generating great interest is the acoustic

[160]method. In this method, the velocity of acoustic waves passing through the specimen is measured. The wave velocity depends on the state of strains in the material, and as long as the material is in its elastic regime, the strain is proportional to the residual stress. Thus the stress can be calculated from the wave velocity. Acoustic wave velocity ( $V$ ), strains ( $\epsilon$ ) and stresses ( $\sigma$ ) are related by [[160],

$$V = K\sqrt{M + C\epsilon} \quad (\text{EQ 2.7.4})$$

$$\sigma = M\epsilon + C\epsilon^2 + D\epsilon^3 \quad (\text{EQ 2.7.5})$$

Where  $K$  is a constant;  $M$ ,  $C$  and  $D$  are higher order constants.

Another most commonly used method relies on the diffraction of x-rays or of neutrons. When residual stress exist in a material, the lattice spacing differ from a stress free value. These internal strain gauges are the basis for residual stress measurement by x-ray diffraction in crystalline materials. A minimum of two measurements of lattice spacings, one typically being normal ( $d_n$ ) and other inclined to the sample surface, are required to calculate surface residual strain. The strain values are converted to stress values using a proper elastic constant. It has been shown [152,161], using elasticity, that the residual stresses are related to the difference in d-spacing or alternatively the diffraction angles as expressed in following equations:

$$\sigma_\phi = \frac{E}{(1 + \nu) \sin^2\Psi} \left( \frac{d_i - d_n}{d_n} \right) \quad (\text{EQ 2.7.6})$$

$$\sigma_\phi = K\Delta\theta \quad (\text{EQ 2.7.7})$$

$$K = \frac{E \cot\theta}{2(1 + \nu) \sin^2\Psi} \frac{\pi}{180} \quad (\text{EQ 2.7.8})$$

where

Normal

the slope

the  $\sin^2$

29a. A

stresses

ponent

indicate

X-ray d

only a v

resolved

metals,

where  $\phi$  is the direction of the residual stress and  $\psi$  is the tilt angle.

Normally this technique involves 3 to 4 tilt angles and uses linear regression to solve for the slope of the  $\sin^2\psi$  against  $\frac{d_i - d_n}{d_n}$  from above equations. Four basic variations of the  $\sin^2\psi$  curve are illustrated in figure 29. A common  $\sin^2\psi$  plot is depicted in figure 29a. A positive slope represents tension and a negative slope indicates compressive stresses. Figure 29b shows the behavior associated with the existence of shear stress component normal to the surface. A non linear  $\sin^2\psi$  plot, showing oscillations (figure 29 d) indicate the presence of strong crystallographic texture.

X-ray diffraction has inherent limitations in the depth of penetration. The stress state of only a very shallow layer of specimen can be determined. This limitation of x-ray can be resolved by using neutrons. Whereas x-rays penetrate only about 20 micrometers in most metals, neutrons can go through several centimeters of steel.

Figure

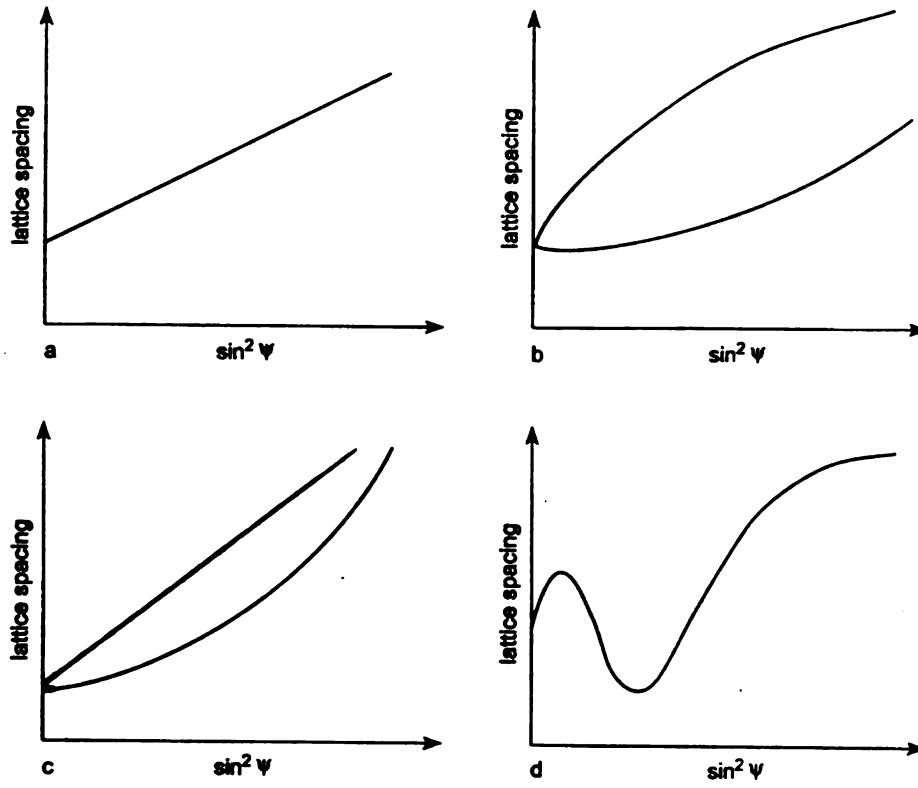


Figure 29. Lattice spacing variation with  $\sin^2(\psi)$ , in four different cases. [154]

### III EXPERIMENTAL WORK

A Raytheon Nd:YAG laser of 500 watts output power, was used for the present work. AISI 1018 steel samples in the shape of a rectangular plate (2.5 cm X 2.5 cm X 0.625 cm) were used for laser carburizing and boriding studies. AISI 1045 steel samples, with same shape and dimensions, were used for laser transformation hardening studies. Initially all the samples were in annealed condition, containing pearlite and proeutectoid ferrite. The microstructure of as received AISI 1018 and AISI 1045 steels is shown in figures 30 and figure 31 respectively. The chemical composition of two steels (supplied by Bethlehem steel) is given in table 3.1

**Table 2. Composition of steels in weight percentage**

Steel	C	Mn	P	S
AISI 1018	0.19	0.51	0.034	0.017
AISI 1045	0.48	0.77	0.026	0.016

Typical sample designs, used for laser transformation hardening, are shown in figure 32. Samples with grooves were laser hardened at the edges and at the root of the groove. Samples with holes, were laser treated around the circumference of the hole. These sample configurations (shown in figure 32) were chosen because they simulate typical locations in many automobile components which require selective hardening. Two types of CNC positioning tables were used to move the samples under the laser beam. A microprocessor controlled linear motion table was used to move the samples with straight grooves. A circular motion table was used to rotate the sample axially with the hole. The traverse speed used was in the range 1-10 mm/s. Laser power used was in the range 20-100 watts. A defocused







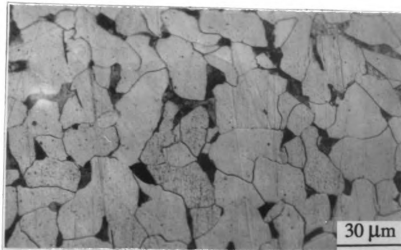


Figure 30. Microstructure of AISI 1018 steel before laser treatment.

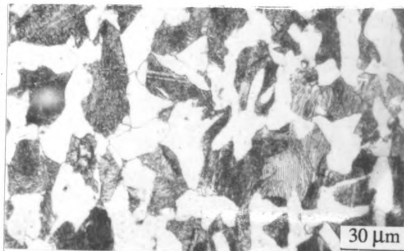
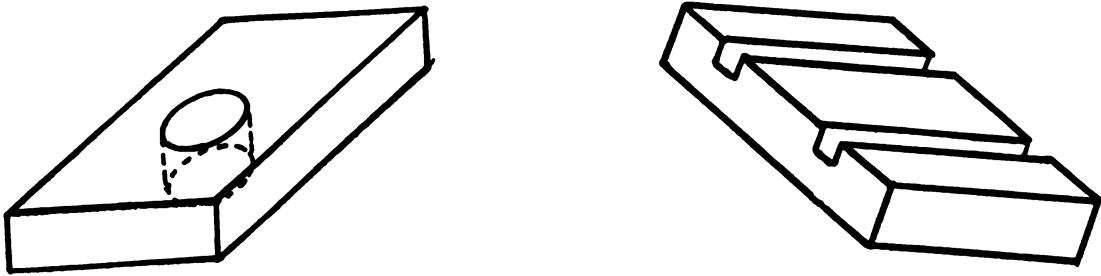


Figure 31. Microstructure of AISI 1045 steel before laser treatment.



**Figure 32. Sample design used for laser transformation hardening.**

beam was always used for hardening and heat treatment. By varying the laser power, traverse speed and the position of the sample surface with respect to the focal plane of the laser optics, hardened layers of various thickness were obtained. Care was taken to avoid melting at the surface, which is normally undesirable during hardening. Samples with varying surface conditions, including metallographically cleaned surfaces were used for laser hardening, to study to effect of surface conditions on the coupling of Nd:YAG laser with steel. Various surface conditions used were: graphite coated (in amyl acetate), fine polished (600 grit), and polished and etched (1 hr in 10% HNO<sub>3</sub> acid) surfaces.

For laser carburizing studies a graphite coating was applied on to the AISI 1018 steel samples before laser treating. The binder used for the graphite coating was amyl acetate. For Boriding studies boron powder was put on to the AISI 1018 steel specimens and no binder was used. The experimental configuration for carburizing and boriding is shown schematically in figure 33. By varying laser power, traverse speed, focusing conditions, and coating thickness carburized zones and borided zones of various thickness were obtained.

After each of the laser surface treatments (hardening, carburizing and boriding) both longitudinal and transverse sections of the samples were cut, polished and etched with nital (3% HNO<sub>3</sub> acid in methanol) for microstructural examination. Samples were mounted on epoxy resin before polishing to ensure edge retention of the surface treated layers. The magnitude of hardening and hardness distribution of laser treated zones were measured using a micro-hardness tester (manufactured by Buehler). Microstructural investigations of transverse and longitudinal sections were carried out by using an Olympus optical microscope and scanning electron microscopes (Hitachi S-415 and S-2500). Phases present in the laser hardened, carburized, and borided layers were examined by using a Scintag x-ray diffractometer (XRD). A wave length dispersive chemical analysis, of carburized and borided zones, was done by using an electron microprobe (Applied Research Laboratories,





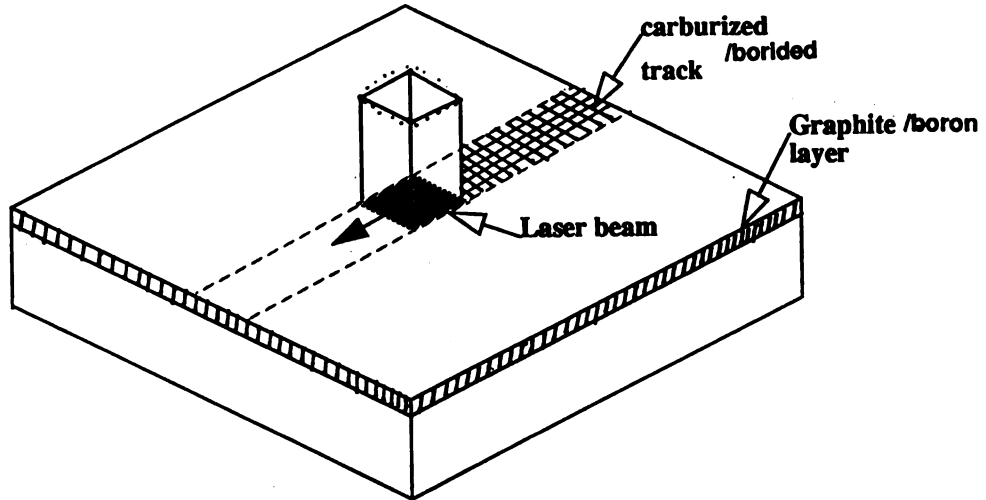


**Figure 33. Schematic of laser carburizing / boriding. Note that an idealized square cross section laser beam is drawn. This geometry simplifies heat conduction analysis as discussed later.**

Inc.), to map the distribution and concentration of B,C and Fe in the laser surface treated zones.

Pt./Pt 13% Rh thermocouples were spot welded on to the surface of some specimens at various locations, away from track, to monitor the temperature variation with time. The temperature data was used for determining the boundary conditions utilized in the temperature distribution model.

## IV RESULTS AND DISCUSSION

### 4.1 Laser Hardening

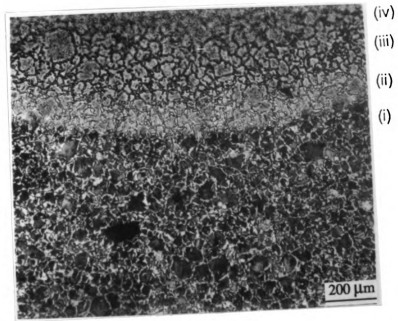
#### 4.1.1 Microstructural Study

Figure 34 shows a typical microstructure of heat affected zone (HAZ) of laser hardened specimen. Figure 35 illustrates the formation of various subzones in the HAZ hardened zone. Middle of the figure 34(a) is the boundary of the HAZ. A magnified view of the HAZ shows 4 distinct zones spreading outwards from the HAZ boundary as follows:

**(i) Mixture of Martensite and virgin ferrite:** The temperature in this zone was above  $A_1$  but below  $A_3$ , where  $A_1$  and  $A_3$  are eutectoid and austenisation temperatures respectively. Pearlite colonies transformed into austenite, which upon subsequent cooling transformed into martensite. Due to the very high heating rate, these pearlite colonies did not have sufficient time to interact with their neighbouring ferrite and hence their carbon content remained essentially unchanged.

**(ii) Mixture of Martensite and curly ferrite:** In this zone both the peak temperature and diffusion time increased. As a result the prior pearlite colonies expanded while austenized and formed martensite colonies of slightly lower carbon content during subsequent cooling. Since the ferrite grain size in this zone is significantly smaller than that of base metal, the peak temperature at position (ii) in figure 34 must have exceeded the eutectoid temperature.

**(iii) Mixture of Light and dark- etching martensites:** This zone can be seen at position (iii) in figure 34. The dark etching martensite is low in carbon content and has a hardness of  $\sim 470$  Hv. It originated from ferritic regions. The light etching martensite is high in car-



(a)

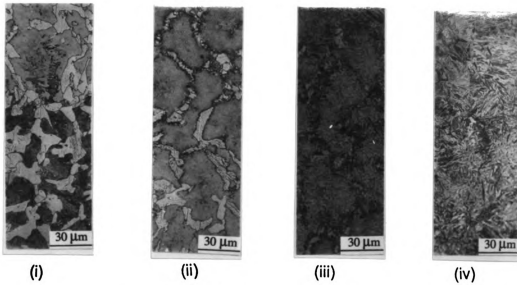


Figure 34. Typical HAZ of laser hardened sample (a) (x75): (i), (ii), (iii) and (iv) are the magnified (x500) views of the 4 sub-zones respectively.

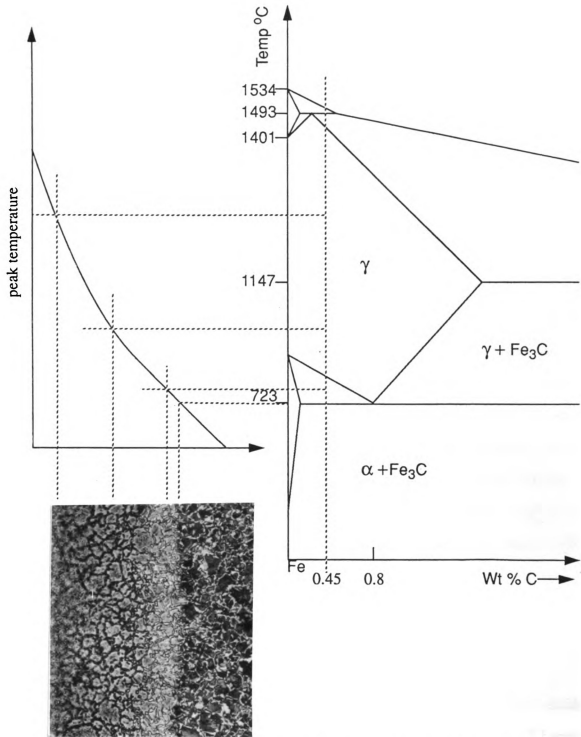


Figure 35. Subzones in HAZ corresponding to AISI 1045 temperatures in the Fe - Fe<sub>3</sub>C equilibrium diagram.



bon content and has a higher hardness of  $\sim 780$  Hv. The time above  $A_3$  temperature was insufficient for much carbon to diffuse from the high carbon austenite (from pearlite) to the austenite which formed from the ferrite.

**(iv) Nearly homogeneous martensite:** Nearly homogeneous martensite structure was observed at the surface. At the surface the temperature is maximum and, since diffusion coefficient is a strong function of temperature, almost complete homogenization is achieved at the surface, with respect to carbon concentration.

No unusual phase changes were observed in laser hardened specimens as compared to the furnace treated specimens. However the rapid heating and cooling rates in laser hardening resulted in the fineness of the martensite. The hardness of the martensite formed in laser treated specimens was found to be  $\sim 50$  Hv higher than the hardness of the martensite formed in furnace treated specimens. Nutting's [165] review about factors controlling the martensitic substructure, where the composition and cooling rates are considered, seems to be significant in the laser hardening. His prediction about fineness of martensite with increasing cooling rate, proves to be true in case of laser hardening, where a high cooling rate ( $\sim 10^4$  K/s) is achieved [6,50]. Figures 36 (a) and (b) show the martensite formed in the laser treated samples and in furnace treated samples respectively.

#### **4.1.2 Effect of Surface Conditions**

Figure 37 shows the effect of surface conditions on the hardness profile, at HAZ, during laser hardening. The same settings of laser power (135 watts), traverse speed (2.5 mm/s), and focal condition (17 mm) were used for studying the effect of surface conditions on coupling of Nd:Yag laser with steel. No significant variation was observed in the hardness profiles obtained from specimens treated under different surface conditions. Significant effect

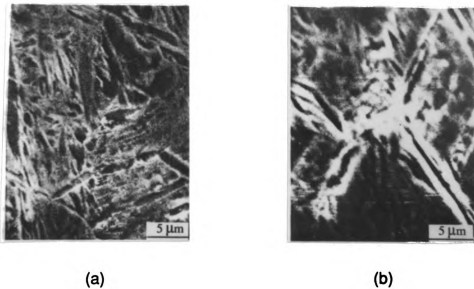


Figure 36. Micrographs comparing martensite (a) from conventional (furnace) hardening, and (b) from laser hardening.

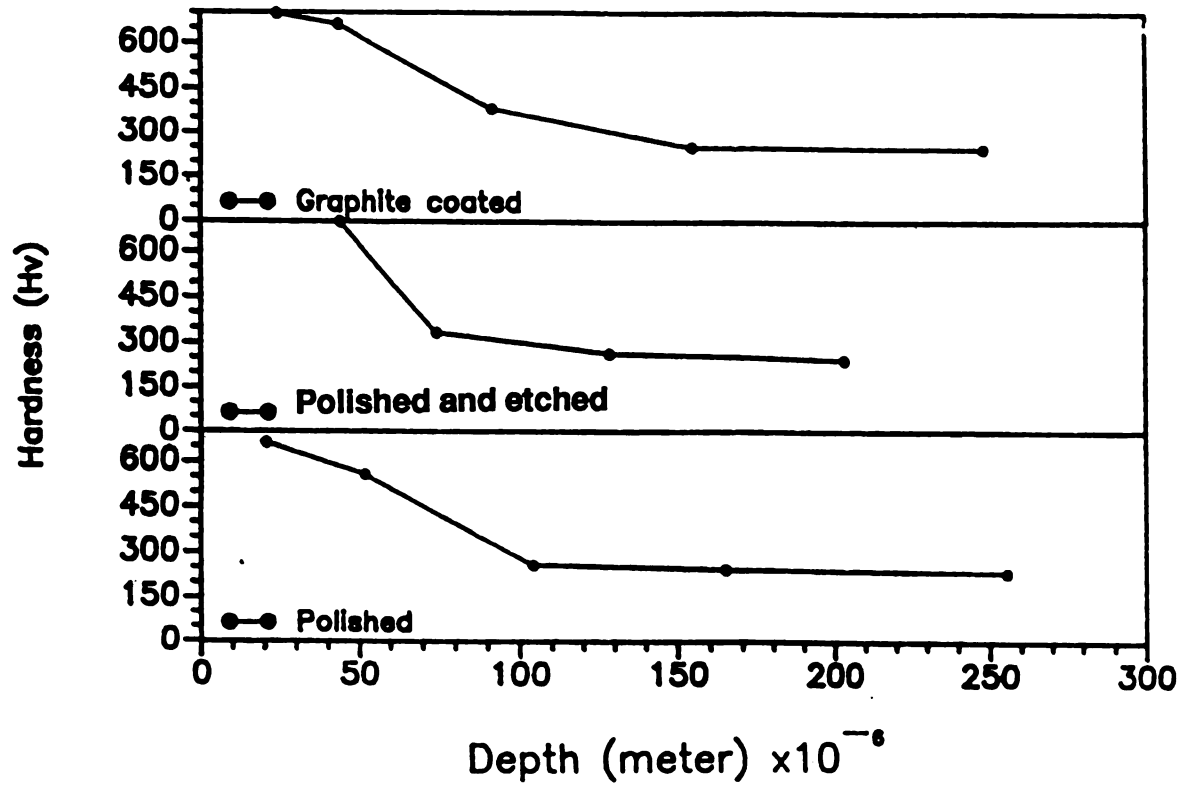


Figure 37. Influence of surface conditions on the hardness profiles at the HAZ of laser hardened samples.

of graphite coating on the absorption coefficient of CO<sub>2</sub> laser, shown in the past [28,42], was not observed in our experiments. The reason for this, we believe, is due to the fact that the coupling of Nd:Yag laser with steel is quite high even without any coating [6]. However, some hardness increase at the surface and spread of HAZ is evident from the hardness profile in case of graphite coated specimens.

#### **4.1.3 Effect of Laser Power, Traverse Speed and Laser Focusing Conditions**

It has been reported [33] that the magnitude of surface hardness and the width of the HAZ are directly proportional to the laser power, but this is only true as long as the austenization is not complete. Our hardness results for input energy less than that for complete austenization are shown in figure 38. At laser powers higher than threshold for completion of austenization, the hardness does not increase with increasing power. This can be seen from figure 39. Figure 38 and figure 39 show the influence of laser power on the hardness profiles and depth of HAZ. The results shown there are obtained by varying laser power and keeping other process parameters the same. It is evident from figure 37 that the maximum of hardness increases with power. This is because a higher temperature causes a higher carbon dissolution and a better homogenization of the austenite. This trend of increasing hardness with increasing power, does not, however, continue indefinitely as shown in figure 39. It shows a decrease in hardness with further increase in power. This is because after complete austenization, additional energy input produces overheating of austenite, which impedes the formation of martensite [166]. Hence a coarse martensite forms, which is known to have a lower hardness [165]. Figure 40 confirms the nonlinear variation of hardness depth and surface hardness with increasing power density. Figure 40 shows the influence of focusing conditions on the hardness of HAZ. When the specimen surface is 1.3 cm away from the focal plane, maximum surface hardness is obtained as shown in figure 40. Reducing the distance between the focal plane of the laser and the surface of the spec-

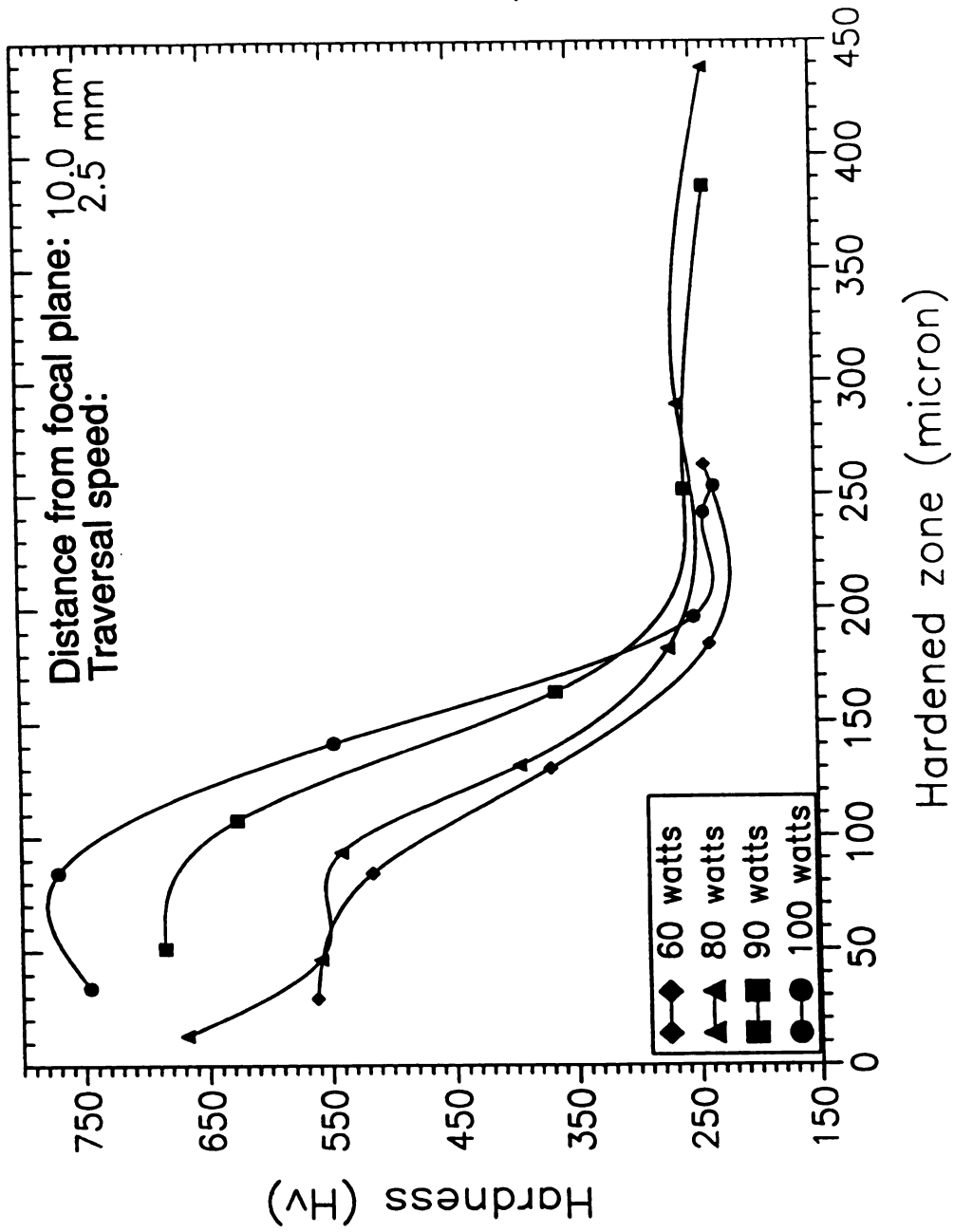


Figure 38. Hardness profiles at the HAZ of laser hardened samples, with increasing laser power (just upto austenization).

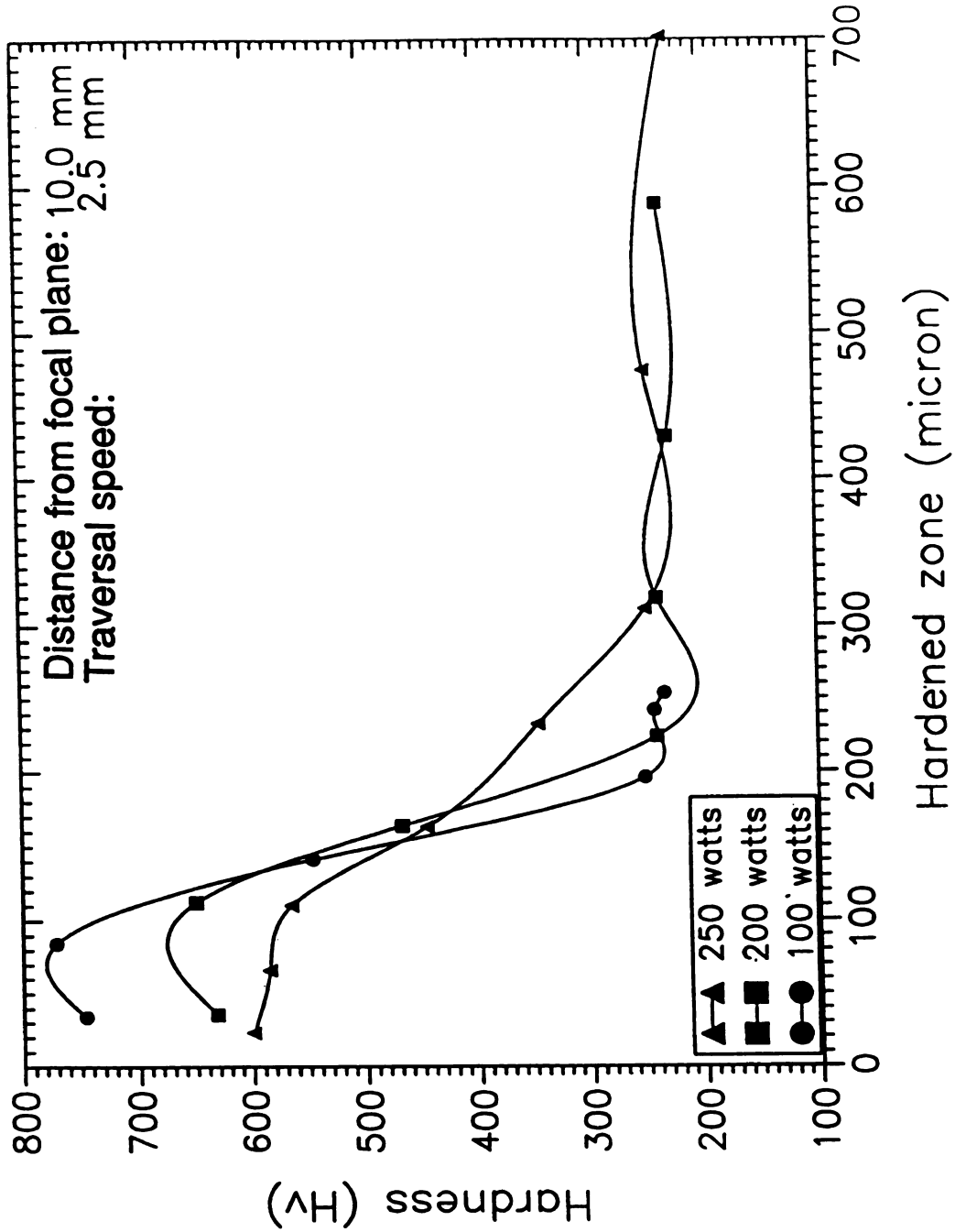


Figure 39. Hardness profiles at the HAZ of laser hardened samples, with increasing laser power (beyond austenization).

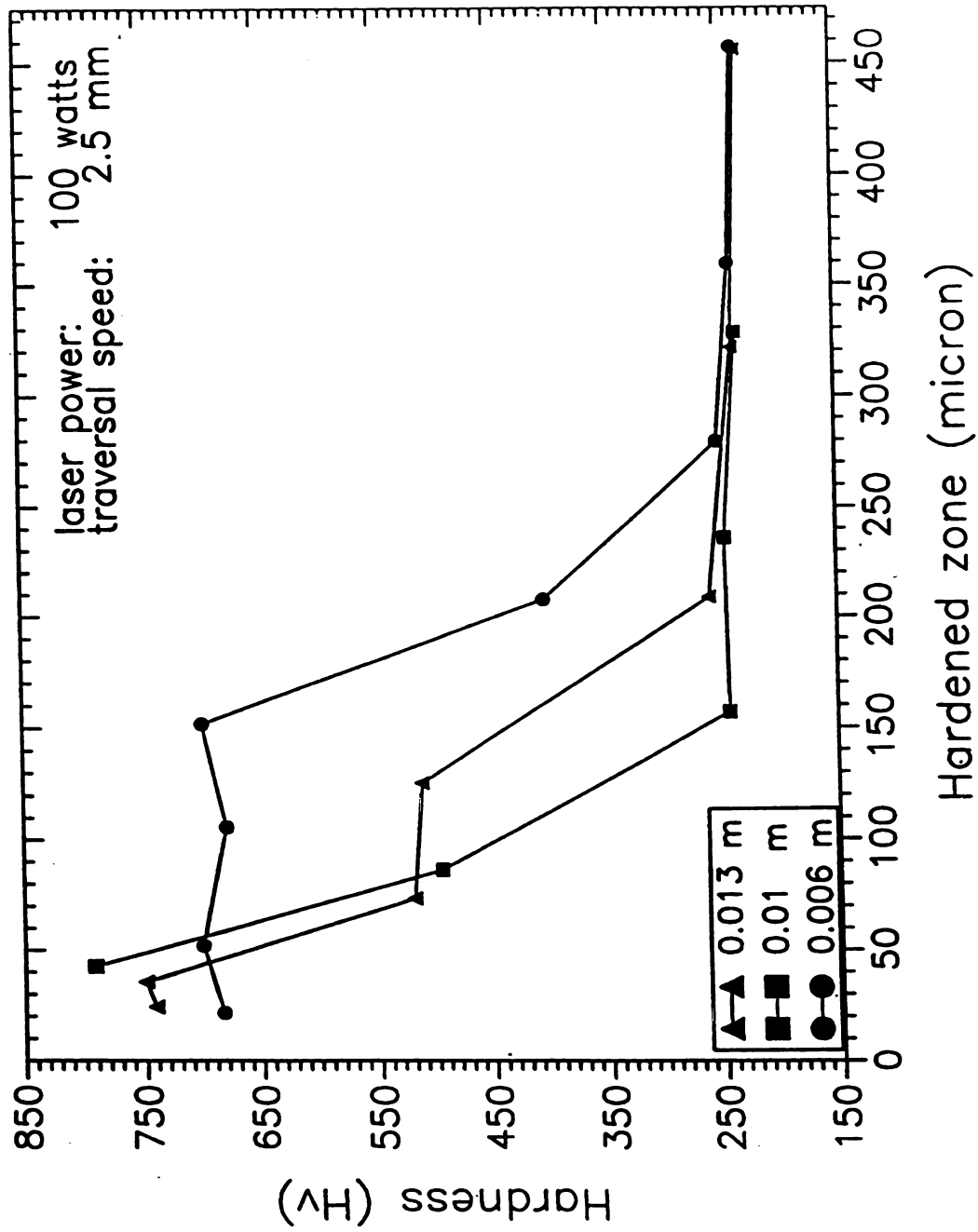


Figure 40. Influence of focal conditions on the hardness profiles at the HAZ of laser hardened samples.

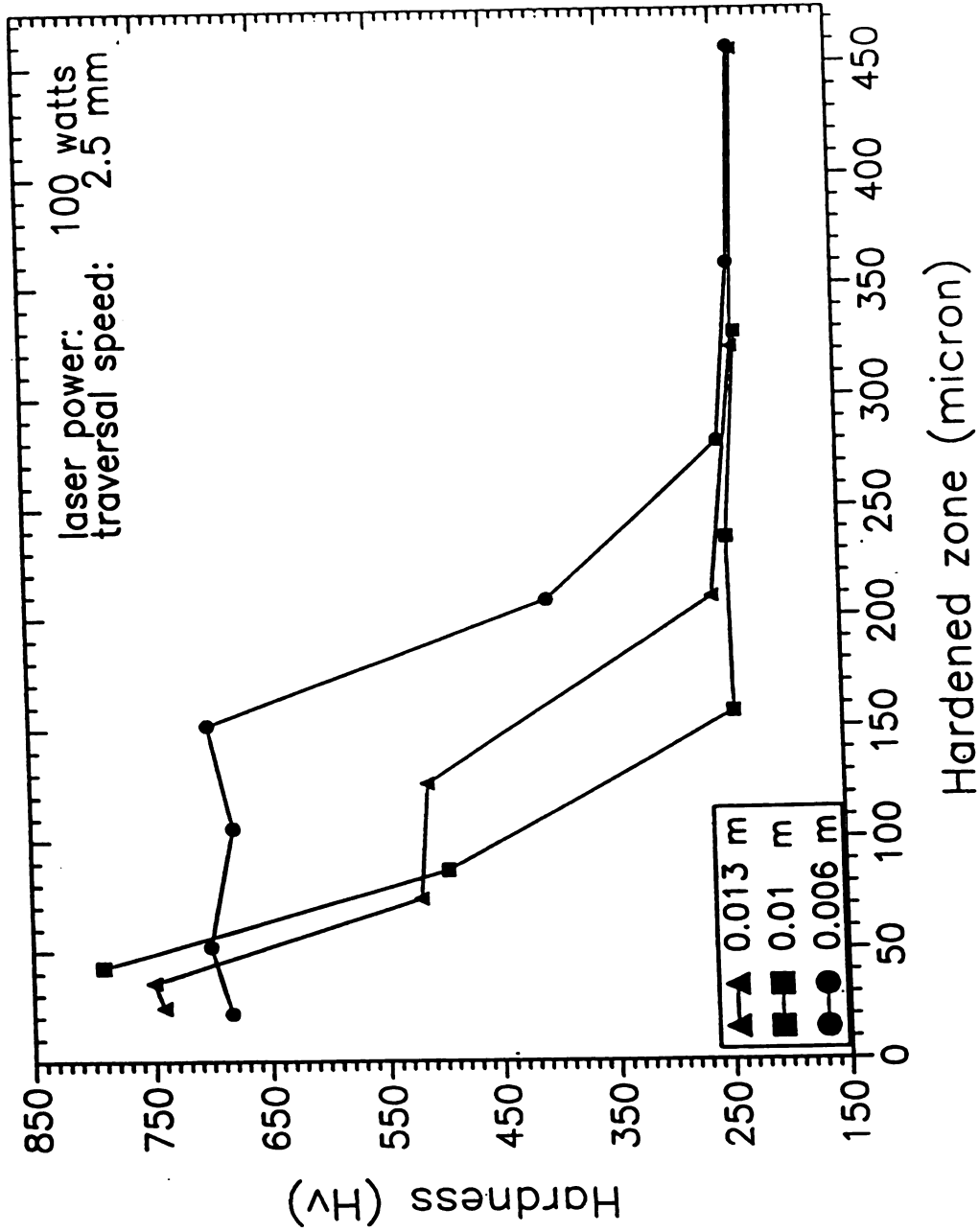


Figure 40. Influence of focal conditions on the hardness profiles at the HAZ of laser hardened samples.

imen increases the power density and hence a higher temperature is attained. Higher temperature (above austenization) induced larger austenite grain size, which resulted in a less hard martensite upon cooling. It has been established [167,168] that larger prior austenite grains would result in less hard martensite

The above results show that although the depth of HAZ increases with increasing laser power, the maximum hardness produced in the HAZ does not necessarily follow the same trend. For hardening purpose both parameters are equally important. Hence a combination of laser parameters is required, which will achieve optimization of hardness and the HAZ depth by achieving:

- (a) high enough temperature at the surface for complete austenization, and
- (b) a high enough interaction time for complete homogenization.

In addition to the consideration of maximum hardness, the problem of melting at the surface has to be kept in mind. We cannot indefinitely increase HAZ depth by increasing laser power density, because at certain case depth limit, the surface will start showing partial melting. Thus the maximum case depth, which can be achieved during laser hardening will always be less than the case depth achieved in conventional hardening.

#### 4.1.4 Experimental Model

To correlate various laser parameters with maximum HAZ depth during laser hardening, a simple first order model can be proposed based on the approach, which has been used for weld parameters [169]. The relation between temperature and energy is controlled by the specific heat of metal thus:

$$\frac{E}{V} = C_p \rho (T - T_o) \quad (\text{EQ 4.1.1})$$

where  $E/V$  is the energy per unit volume,  $C_p$  is the specific heat of metal,  $\rho$  is the specific density and  $T_0$  and  $T$  are initial and final temperatures respectively.

Approximating uniformity of energy density in the hardening depth, one gets:

$$\frac{E}{V} = \frac{\text{energy}}{\text{volume}} = \frac{\text{energy}}{\text{area}} \left( \frac{1}{\text{depth}} \right) \quad (\text{EQ 4.1.2})$$

Now combining equations 4.1.1 and 4.1.2 and putting energy = watt X s, one gets

$$\text{depth} = \frac{\text{energy}}{\text{area} (C_p \rho (T - T_0))} = \frac{\text{Watt X s}}{\text{area} (C_p \rho (T - T_0))} \quad (\text{EQ 4.1.3})$$

Where 's' is the interaction time. Interaction time can be calculated from:

$$\frac{\text{laser beam diameter}}{\text{traversal speed}} = \frac{\text{mm}}{\frac{\text{mm}}{\text{s}}} = \text{s} \quad (\text{EQ 4.1.4})$$

Above model was used for determining starting trials for laser hardening. Obviously the model has inherent limitations, but it can be a handy tool for starting trials for heat treatments. It can calculate the maximum depth without considering the energy variation (temperature variation) in depth and on the surface. Since this model does not consider the conduction losses, the predicted HAZ depth has been found to be higher than experimentally observed depths. More complicated models have been developed by Ashby et. al [50], which take into consideration the temperature variation in the source and within the case depth.

#### 4.1.5 Hardness in the Case Depth

As discussed previously (discussion in the section, on microstructure), the carbon in martensite is maximum at the boundary of the HAZ and the parent metal, but still a lower hardness is observed at the boundary than at the surface layers. This can be explained by the mixture rule. The hardness (H) at any depth in HAZ can be given by:

$$H = f_m H_m + (1 - f_m) H_f \quad (\text{EQ 4.1.5})$$

Where  $H_m$  = Hardness of martensite phase,

$H_f$  = Hardness of ferrite phase and

$f_m$  = Fraction of martensite in the microstructure

The hardness of ferrite phase is approximately 160-180 Hv [170]. Hardness of martensite is a function of its mean carbon content. Leslie's result [170] can be used for our purpose, which is the equation of variation of hardness of martensite with its mean carbon content.

The equation is given by:

$$H(C_{\text{mean}}) = 1667C_{\text{mean}} - 926C_{\text{mean}}^2 + 150 \quad (\text{EQ 4.1.6})$$

The mean carbon content ( $C_{\text{mean}}$ ) of martensite can be related to its volume fraction by:

$$C_{\text{mean}} = \frac{C_{\text{total}}}{f_m} \quad (\text{EQ 4.1.7})$$

Combining equations 4.1.5, 4.1.6 and 4.1.7:

$$H = 1667C_{\text{total}} - \frac{926C_{\text{total}}^2}{f_m} + 150 \quad (\text{EQ 4.1.8})$$

This equation predicts a little lower hardness at the surface, when compared with the observed hardness, during laser hardening. This could be mainly due to the fineness of martensite produced during laser hardening, and fineness is not a factor considered in the

model. For example at the surface of laser hardened specimens (AISI 1045), the fraction of martensite can be approximately unity. The model predicts the hardness of  $\sim 712$  Hv, but in practice the maximum hardness achieved at the surface, in this research, was  $\sim 780$  Hv.

## **4.2 Laser Carburizing**

Surface hardness of AISI 1018 carbon steel can be increased to some extent, by laser hardening; for example up to  $\sim 400$  Hv. To increase the hardness further in such a steel, carbon saturation is required at the surface. In the past, solid state carburizing has been quite popular. But to treat a part selectively through conventional technique, proves to be cumbersome and time consuming. Hence laser carburizing has been attempted. Figure 41 compares the hardness profile at the transverse section of specimens, surface treated by laser hardening and laser carburizing respectively. It shows that maximum hardness achieved during laser carburizing is more than twice that achieved in laser transformation hardening. Detailed study of laser carburizing of AISI 1018 steel is shown in the following subsections

### **4.2.1 Microstructural and Hardness Profile Studies**

Microstructures (in the laser carburized zone), which evolve by laser carburizing of 1018 steel can be explained by using Fe-Fe<sub>3</sub>C diagram ( figure 42). Basically the amount of carbon in surface layer will control the type of microstructure, that can be expected. Various microstructures which have been observed in laser carburized layers can be seen in figures 43, 44, 45 and 46. These microstructures are from the surface of the laser carburized zone. Figure 43 shows the hypoeutectic structure; cellular primary austenite in the eutectic matrix (austenite and iron carbide). Figure 43 shows the transverse sections of austenite dendrites growing perpendicular to the laser carburized zone interface. The average pri-

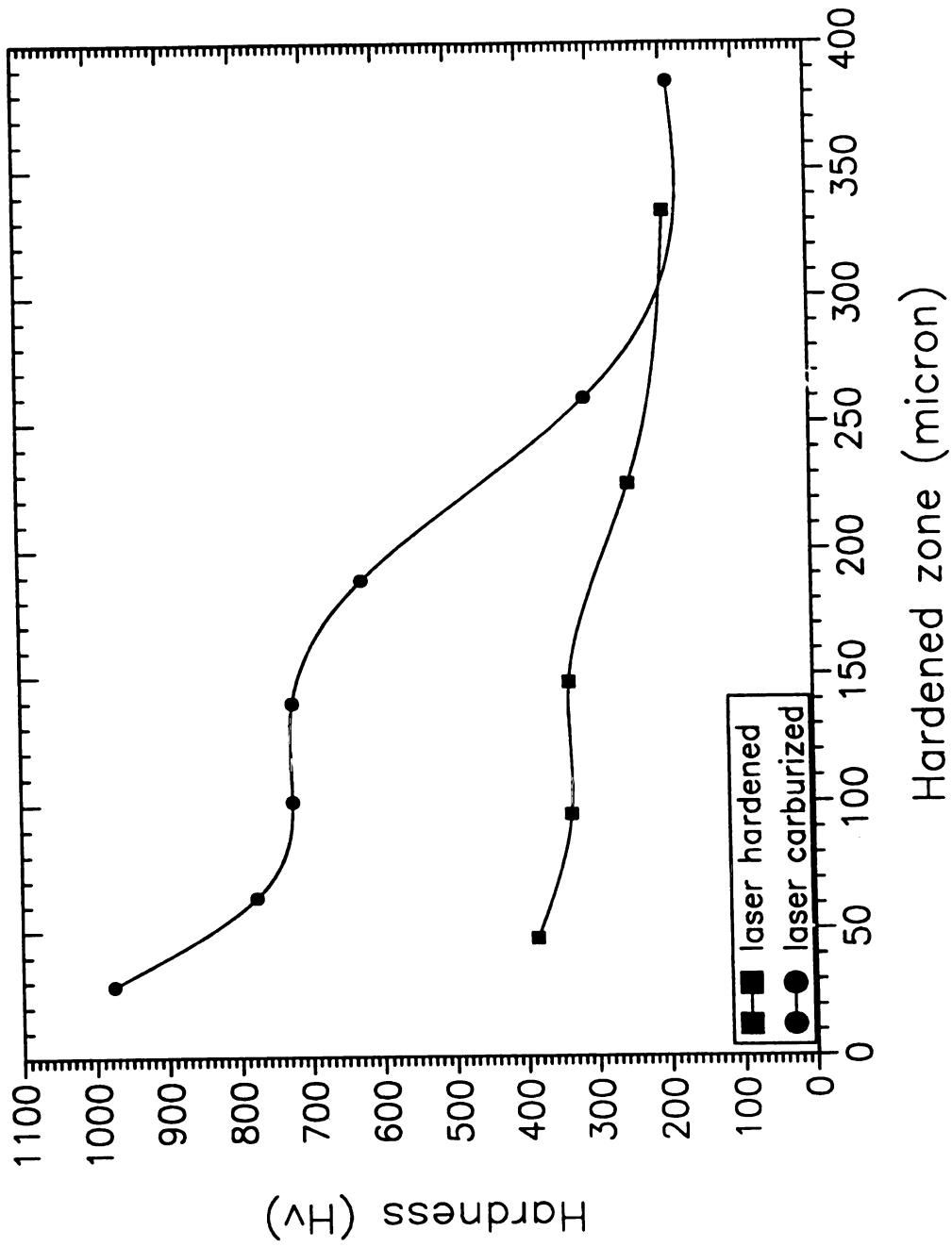


Figure 41. Comparison of hardness profiles at the transverse section of samples, surface treated by laser hardening and laser carburizing.

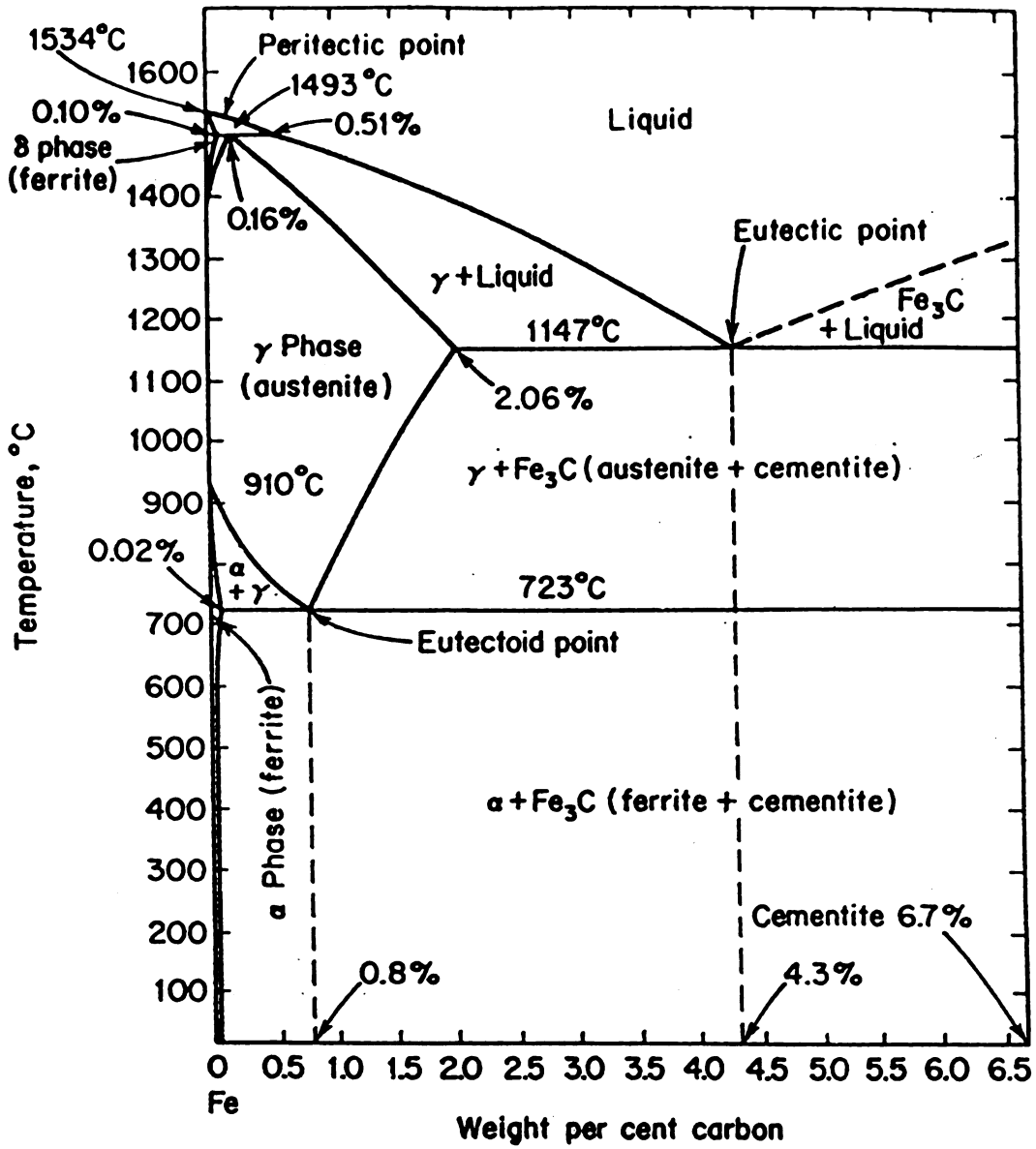


Figure 42. Fe - Fe<sub>3</sub>C equilibrium diagram. [185]

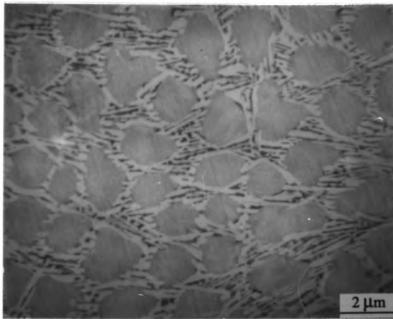


Figure 43. SEM micrograph showing hypo-eutectic structure. Laser power 200 W, traverse speed 3.88 mm/s and graphite layer thickness 0.41 mm.

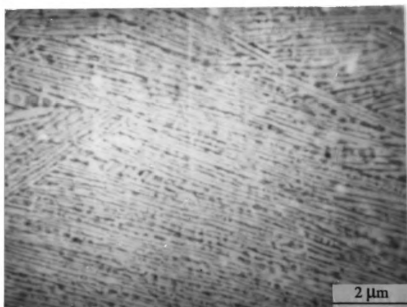


Figure 44. SEM micrograph showing eutectic structure. Laser power 150 W, traverse speed 3.88 mm/s and graphite layer thickness 0.41 mm.

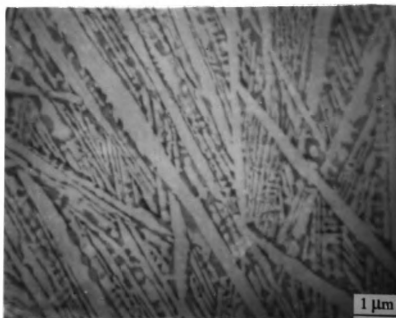


Figure 45. SEM micrograph showing hyper-eutectic structure. Laser power 200 W, traverse speed 3.88 mm/s and graphite layer thickness 0.41 mm.

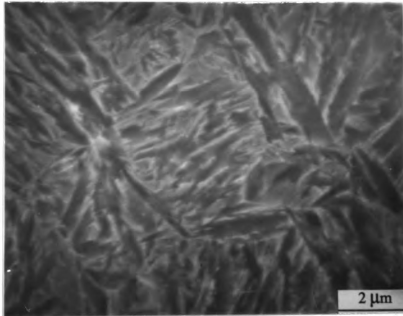


Figure 46. SEM micrograph showing martensite structure. Laser power 250 W, traverse speed 3.88 mm/s and graphite layer thickness 0.13 mm.

mary arm spacing was found to be ~1 micro-meter and the average secondary arm spacing was approximately 0.25 micro-meter. The volume fraction of eutectic increases with carbon content of the zone until at a carbon composition approaching the equilibrium eutectic (4.3 wt% C), a lamellar type eutectic solidification occurs without any primary solidification (figure 44). The lamellar structure has apparent spacing in the range of 0.3-0.8 micro-meter. Over 4.3 wt% carbon content, the hypereutectic microstructure evolves (figure 45) (lamellar primary carbides with interlamellar eutectic). This structure is harder than the eutectic structure, because of the inherent high hardness of iron carbide phase ( $\text{Fe}_3\text{C}$ ).  $\text{Fe}_3\text{C}$  phase is known to be the hardest phase in Fe-C system. The high fraction of primary  $\text{Fe}_3\text{C}$  in the microstructure (figure 45) shows, that during laser carburizing, a very high level of carbon solution can be achieved. This corresponds to approximately 5.5 wt % of carbon. Under certain conditions (shown in caption of the figure) of laser parameters and graphite coating thickness, martensitic structure (figure 46) also evolved. Such a structure was formed when the dilution (with respect to carbon) in the molten zone was high enough to keep the martensite start ( $M_S$ ) temperature of the structure above room temperature. Microhardness of such a martensite was found to be approximately 650 Hv.

Figure 47 shows the scanning electron micrograph of a longitudinal section of laser carburized samples. It shows the hypoeutectic structure at the center of the zone followed by a single phase austenite and eventually a martensite at the interface of the molten zone and the parent metal. This variation of microstructure from the center of the molten zone to interface indicates the increasing dilution of carbon at the interface of the molten zone and the substrate. Figure 48 shows the transverse section of a laser carburized specimen, showing the hardest structure obtained during trials of laser carburizing. The carburized zone consists of a hyper-eutectic structure. It shows the acicular morphology of primary carbides in the matrix of a fine eutectic (austenite & iron carbide). Microhardness in this region fell in the range of 950 to 1050 Hv. A distinctive feature seen in figure 48, is the

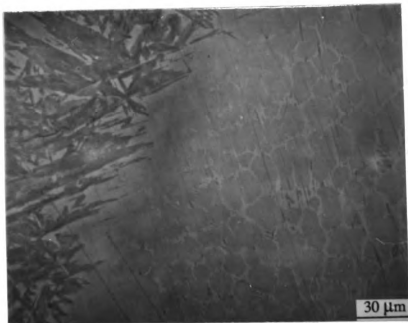
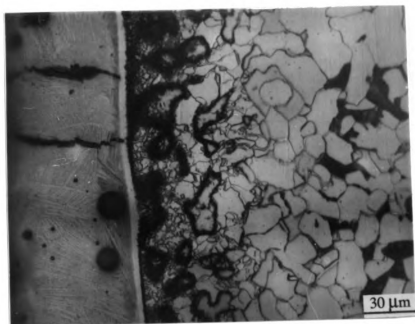


Figure 47. SEM micrograph showing the variation of microstructure from center line of carburized zone to fusion line of carburized zone. Laser power 200 W, traverse speed 3.88 mm/s, and graphite layer thickness 0.41 mm.



**Figure 48.** SEM micrograph of transverse section of laser carburized sample, showing hyper-eutectic structure. Laser power 100 W, traverse speed 3.88 mm/s, and graphite layer thickness 0.18 mm.

light etching region (~4 micro-meter thick) with a hardness in the range of 600 to 620 Hv, along the whole length of the interface between the melt zone and the martensitic HAZ. This interface region was interpreted as being mostly austenite with some martensite. This feature is due to the solid state diffusion of carbon, leading to the depression of the  $M_s$  temperature and austenite retention. The hardness of austenite in this region is unusually higher than the hardness of the austenite formed during conventional carburizing. The high hardness indicates a high saturation of carbon in the austenite phase. This speculation was also verified by the x-ray studies. This will be discussed in detail in the section dealing with the features of austenite. Similar observations have been reported for rapidly solidified cast iron produced by laser processing [171,172]. Through transmission electron microscopy, Walker et al [172] showed that this region consisted of heavily dislocated austenite with some very fine martensite plates.

Figure 49 shows the influence of laser power on the hardness profiles in the transverse section of carburized samples. The hardness profile for power level of 100 watts gives the highest hardness of 1050 Hv. This hardness corresponds to the hyper-eutectic structure. The depth of the molten zone is such that 0.41mm of graphite coating yields microstructure with carbon content more than the eutectic composition. As the power is increased, the depth of molten zone increased, but the amount of carbon remained the same. Hence the dilution of carbon yields the hypoeutectic structure. This corresponds to a power level of 150 watts in figure 49. Finally, when the power is increased further, a deeper molten zone results and it causes extensive dilution of the zone with respect to carbon. The extent of dilution is such that the  $M_s$  temperature is above room temperature. Hence the martensitic structure evolves. This corresponds to the hardness profile for power level of 250 watt in figure 49. Similar to the variation in power, one can vary traversal speed, focal conditions or thickness of graphite layer to adjust the composition of carbon in the carburized zone. Figure 50 shows the effect of graphite coating thickness variation in laser carburizing.

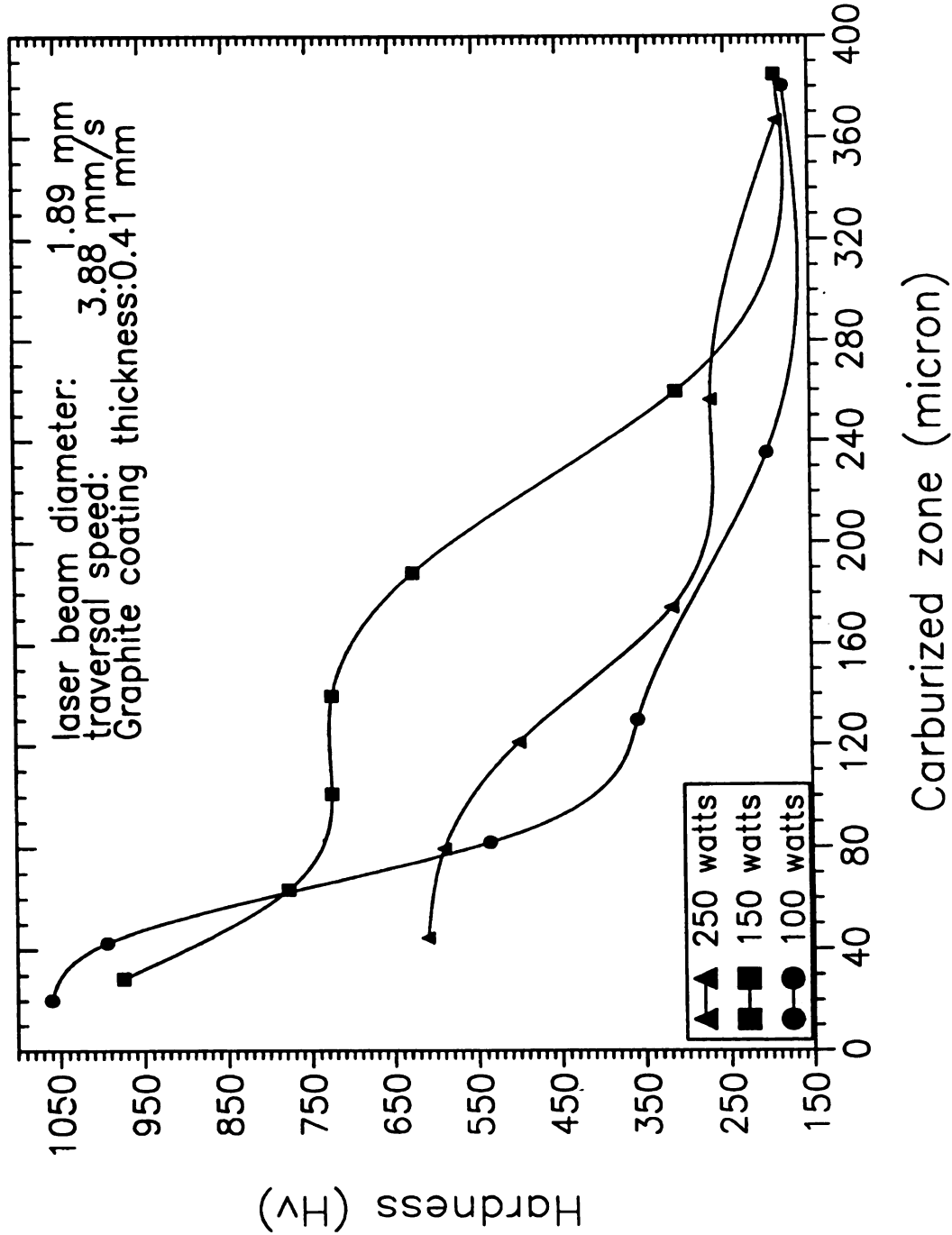


Figure 49. Influence of laser power on the hardness profiles in the transverse section of carburized zones.

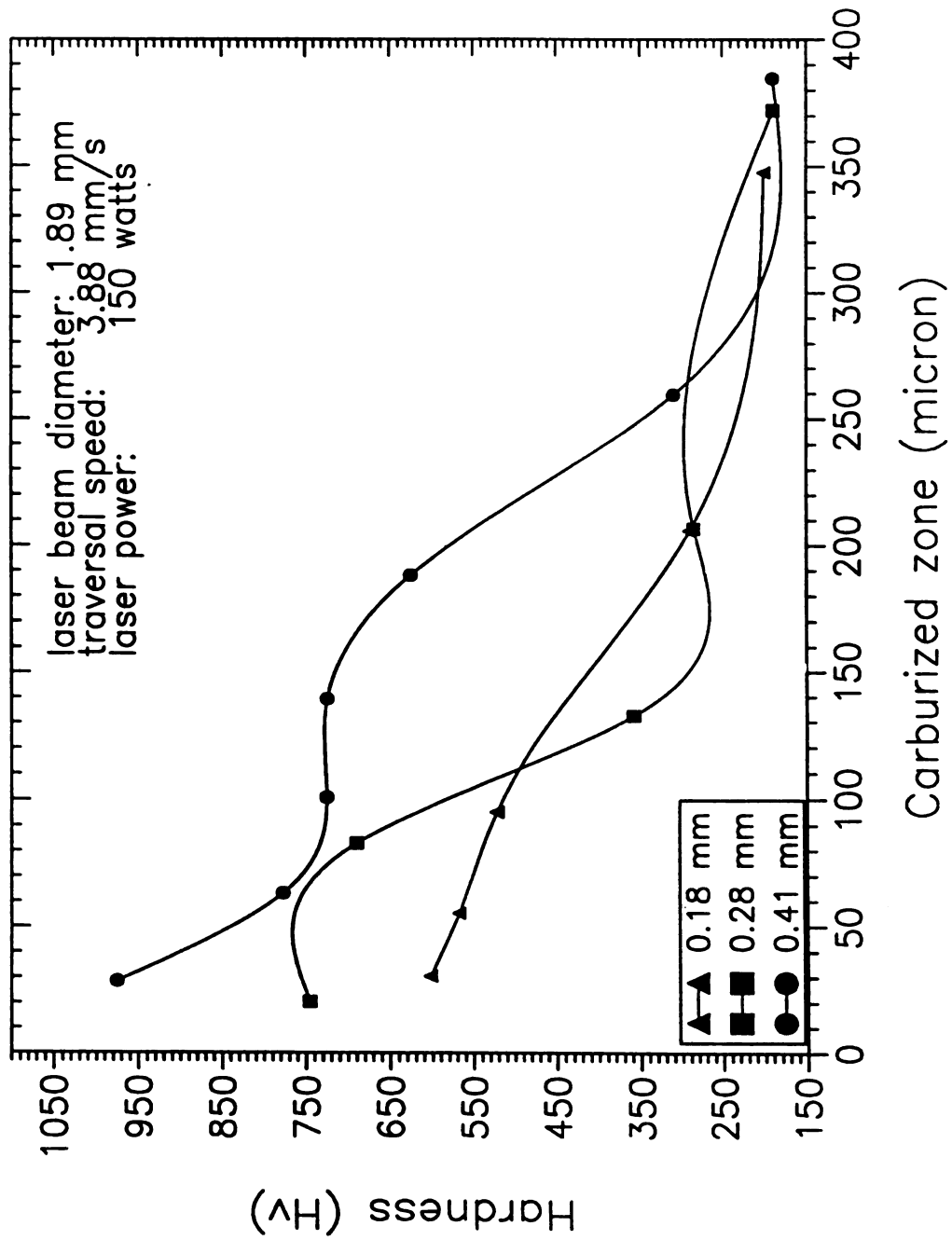


Figure 50. Influence of graphite layer thickness (level of carbon dilution) on the hardness profiles in the transverse section of carburized zones.

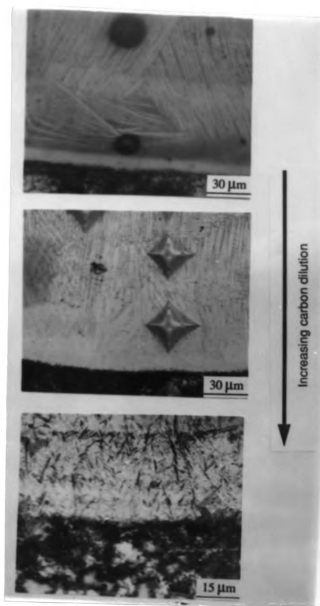


Figure 51. Micrographs showing the variation of microstructure, in carburized zone with increasing degree of dilution of carbon (top to bottom). (a) hyper-eutectic structure, (b) hypo-eutectic structure, and (c) martensitic structure.

Hardness profiles in figure 50 follows the trend explained for figure 49. Microstructures corresponding to trends in figure 48 and 49 are shown in figure 51. The microstructures seen in figure 51 ( top --> bottom) evolves with increasing carbon dilution.

#### **4.2.2 Solidification Morphology**

Microstructures with three distinct morphology have been observed in laser carburized zones:

- (i) Cellular morphology:** Microstructure in figures 52 and 53 consists of cellular morphology of primary austenite in the matrix of eutectic.
- (ii) Dendritic morphology:** Microstructure consists of primary dendrites of austenite in the midst of interdendritic eutectic (as shown in figures 54 and 55).
- (iii) Acicular or plate like morphology:** Microstructure consists of randomly oriented acicular  $\text{Fe}_3\text{C}$  plates in the matrix of fine eutectic (as shown in figure 56).

Typically every microstructure with hypoeutectic composition, obtained during laser carburizing, fell in the first or second category. But most of the time, at the surface of the carburized zone a mixed mode morphology (figure 57) was observed, due to the complexity of heat flow in the molten zone, resulting from the convection in the molten zone. Category 3 morphology is a unique one, observed during laser carburizing. Similar morphology has been reported by Chen et al. [173], while working with melting of cast iron with laser. Chen et al. reported that formation of such a morphology of  $\text{Fe}_3\text{C}$  is favored by marked superheating of the melt, having hypereutectic composition.

The evolution of above morphologies is largely defined by following parameters:

- (a) Thermal gradient G in the direction of solidification.**
- (b) Solidification rate or rate of advancement of solidification front:** For molten pool, like

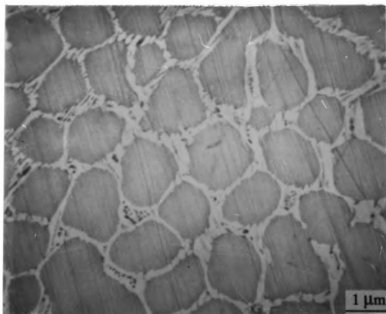


Figure 52. SEM micrograph from longitudinal section of carburized zone, showing cellular morphology. Laser power 200 W, traverse speed 3.88 mm/s, and graphite layer thickness 0.41 mm.

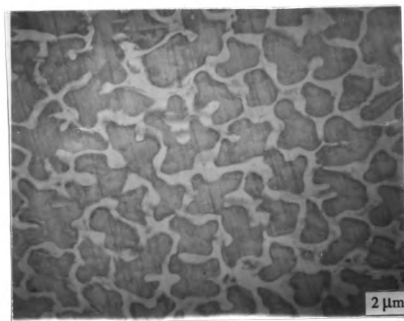


Figure 53. SEM micrograph showing degenerated cellular morphology.  
Process conditions same as in figure 52.

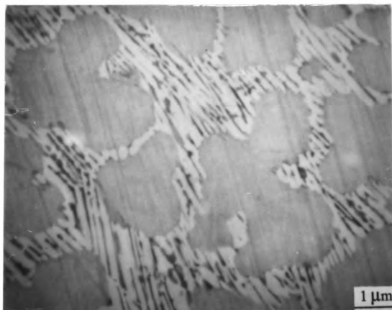


Figure 54. SEM micrograph showing dendritic morphology in the carburized zone. Laser power 200 W, traverse speed 3.88 mm/s and graphite layer thickness 0.41 mm.

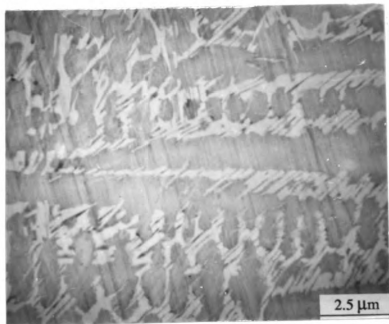


Figure 55. SEM micrograph showing dendritic morphology in the carburized zone. Laser power 200 W, traverse speed 3.88 mm/s and graphite thickness 0.41 mm.

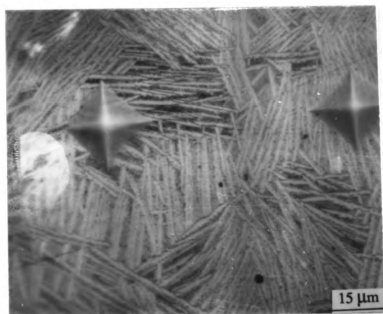


Figure 56. SEM micrograph from the carburized zone, showing acicular morphology. Laser power 100 W, traverse speed 4.25 mm/s and graphite layer thickness 0.22 mm.

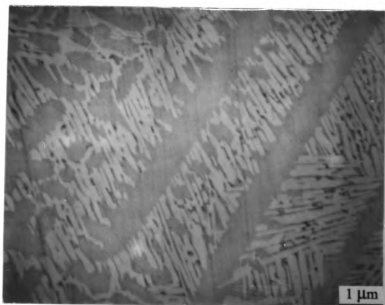


Figure 57. SEM micrograph showing cellular-planar structure. Laser power 150 W, traverse speed 3.88 mm/s and graphite layer thickness 0.41 mm.

the one in laser carburizing, the solidification rate is given by:

$$R = \frac{u \cos(\alpha)}{\cos(\alpha - \beta)} \quad (\text{EQ 4.2.1})$$

Where 'u' is the laser traverse speed,  $\alpha$  is the angle between the laser traversal direction and the normal to pool boundary and  $\beta$  is the angle between the traversal direction and the actual solidification direction (figure 58). The above expression for 'R' can be simplified by assuming solidification direction perpendicular to the tangent to the pool boundary.  $\beta$  becomes equal to  $\alpha$  and R can be given by  $u \cos \alpha$  or  $u \sin \phi$ , where  $\phi$  is the angle between the tangent to the molten pool boundary and the traversal direction, as is shown in figure 58.

(c) The carbon content in the solidifying molten zone.

Figure 59 shows the schematic illustration of morphology change from planar to cellular and cellular dendritic as the temperature gradient in the solidification direction decreases. By inducing an extremely sharp temperature gradient (figure 59a) no constitutional supercooling occurs and the solidified zone morphology becomes planar. When the gradient is decreased slightly (figure 59b), any protuberance of solid metal at the interface will grow faster than the remaining flat interface, because the solid is growing into supercooled liquid. As a result, a cellular substructure develops. The liquid ahead and alongside each cell contains greater solute content than the cell core. If the value of the temperature gradient is decreased further (figure 59c), constitutional supercooling becomes so extensive that secondary arms form and a cellular dendrite growth is observed.

Figure 60 shows the combined effect of G, R and carbon content on the evolution of various morphologies. Figure 60 shows that a large value of G/R combined with a very low concentration of carbon, results in a planar morphology, while a low value of G/R and a high

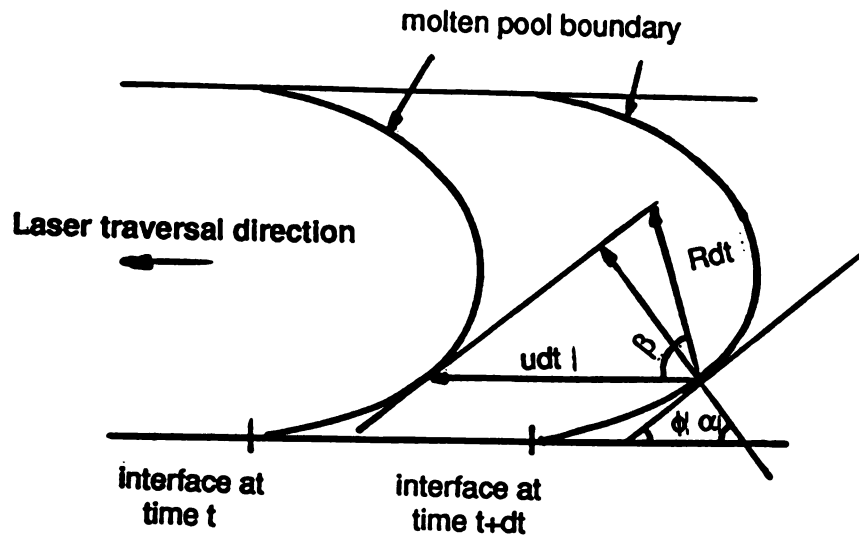


Figure 58. Schematic diagram, showing the relationship between laser traversal speed and actual growth rate. [133]

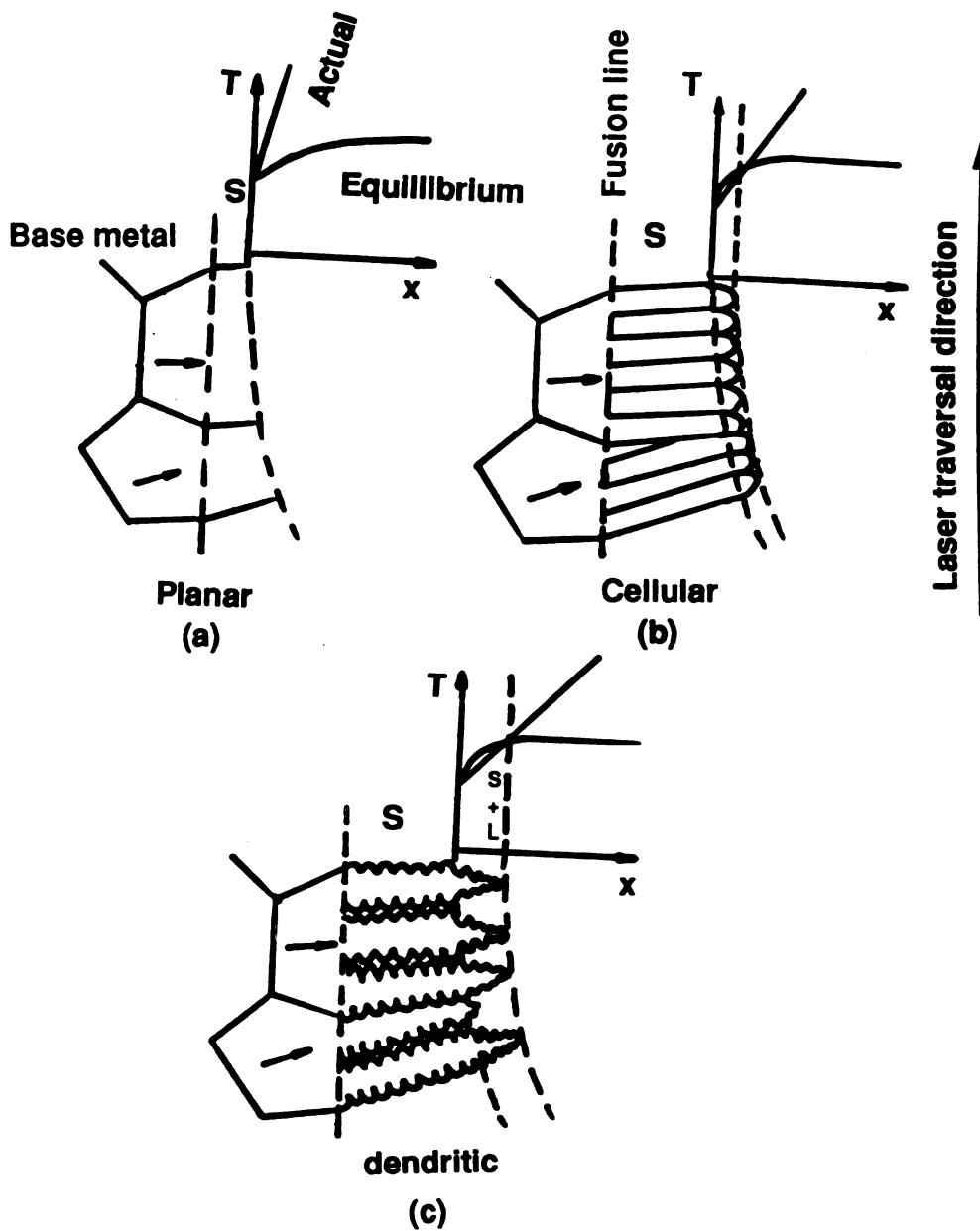


Figure 59. Schematic illustration of morphology change from planar to cellular and cellular dendritic as the temperature gradient, in the solidification direction, decreases. The temperature gradient decrease from (a) to (c). The arrows in the grains of the base metal indicate the easy growth direction.

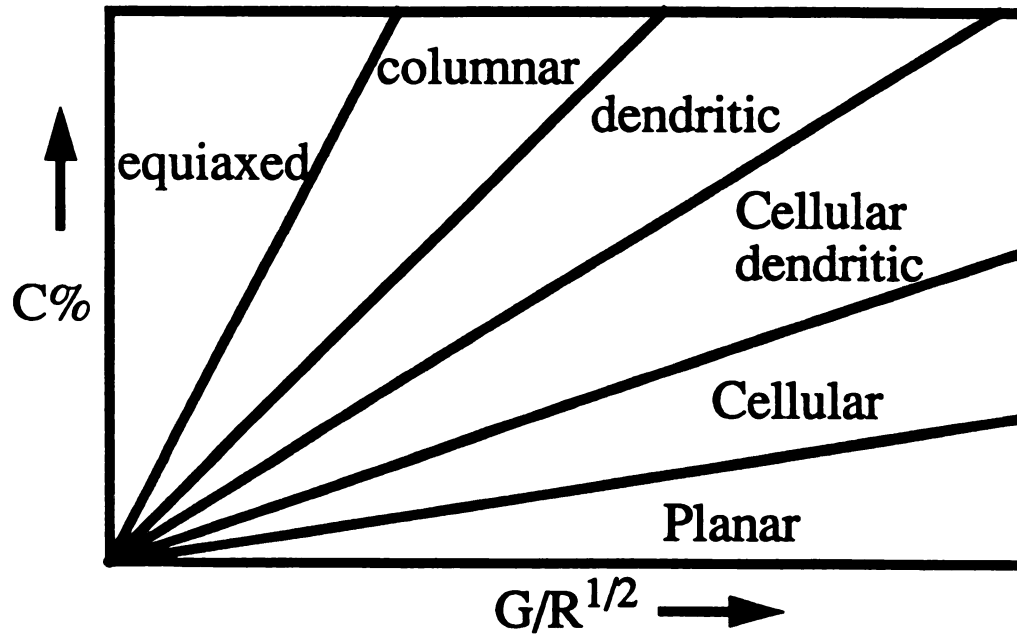


Figure 60. Schematic diagram illustrating the effect of  $G$ ,  $R$  and carbon content on the evolution of various morphologies.

carbon concentration produces a dendritic morphology. Figure 61 shows the transverse section of a laser carburized track. It shows three gradual morphologies: planar at the interface of HAZ and parent metal, cellular next to the planar towards the surface, and Cellular dendritic near the surface of the carburized zone. Similar morphology variations have been found on the surface of a carburized zone, from the fusion line to the center line of fusion. The gradual variation in morphology, from the interface to the surface, can be explained as discussed below.

Since angle  $\phi$  between the tangent to the molten pool boundary and the laser traversal direction varies from  $90^\circ$  to  $0^\circ$  from the center line of the zone to the fusion line, the solidification rate  $R$  is greatest at the zone center line and lowest at the fusion line ( $\sin(\phi) = 0$ ). Therefore  $G/R$  is theoretically infinite. The distance between the moving laser and the molten zone boundary is greater at the center line than at the fusion line because of the elongated shape of the molten pool as has been discussed in the literature survey. Therefore the temperature gradient is smallest at the center line and greatest at the fusion line. Above discussion, along with the schematic in the figure 60, explains the evolution of a planar morphology at the interface and dendritic morphology at the surface of the laser carburized zone, as is shown in figure 61.

The above mentioned simple qualitative model assumes unidirectional heat transfer, but in many cases, misoriented dendrites have been observed (figure 62) at the surface of a laser carburized zone. This is mainly due to the complexity of heat flow, during laser carburizing. Secondly the agitation, which occurs in the molten zone, due to the variation in the surface tension, may also influence the orientation of the dendrites in the laser carburized zone.

For hypereutectic structures, two types of morphologies have been observed: intercon-

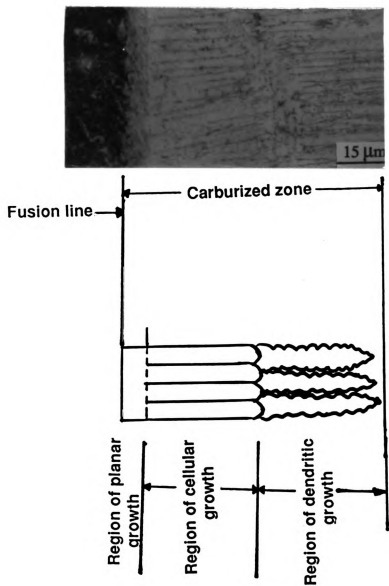


Figure 61. Planar -to- cellular -to-cellular dendritic transition in the laser carburized zone. (a) micrograph (x1000) and (b) schematic illustration.

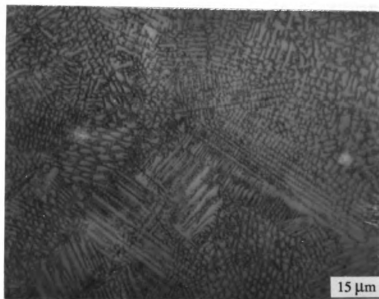


Figure 62. Micrograph from longitudinal section of carburized zone, showing multidirectional dendritic orientation. Laser power 250 W, traverse speed 3.88 mm/s, and graphite layer thickness 0.41 mm.

nected carbide network (figure 63) and individual carbide monoliths (64). Such morphologies have been seen in quenched cast irons during other rapid cooling processes such as melt spinning [56,174] and powder atomization [175,176]. This morphology variation in hypereutectic structure has been explained by Mordike [177] to be due to the rate of cooling. Increasing the rate of cooling replaces the inter-connected carbide network by individual carbide monoliths.

#### 4.2.3 Features of austenite in laser carburized zone

Since most of the laser carburized structures had austenite as a meta-stable phase, this phase deserves detailed study. X-ray diffraction studies (figure 65) showed well defined peaks of austenite phases. It is found from the diffraction peaks that austenite {200} peak intensity is much more intense than the {111} peak. Since, in a randomly oriented austenite material the {111} peak should have about twice the intensity of {200} peak, It can be inferred that there is a preferred <100> growth of austenite dendrites. Normally grains tend to grow in the direction of the heat. However, grains also have their own preferred direction of growth, called the easy growth direction, for example, <100> in face centered cubic (fcc). Therefore, during solidification, austenite with their easy growth direction <100> parallel to the direction of the maximum temperature gradient will grow more easily and crowd out those other grains whose easy direction deviates significantly from the direction of the maximum temperature gradient.

The austenite phase found in most of the microstructures in the laser carburized zones, did not transform to martensite upon liquid nitrogen quenching, which showed that the martensite start temperature ( $M_s$ ) for the austenite, under consideration must be below  $-196^\circ\text{C}$ . The  $M_s$  temperature of austenite in present case is solely controlled by carbon content. In order to calculate the  $M_s$  temperature, the carbon content in austenite was determined by

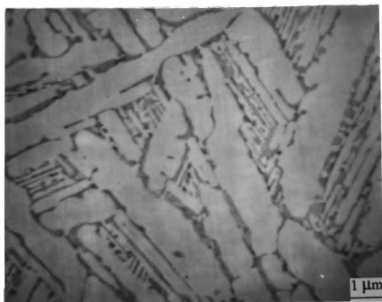


**Figure 63.** SEM micrograph showing interconnected carbide network in the hyper-eutectic structure. Laser power 150 W, traverse speed 3.88 mm/s, and graphite layer thickness 0.41 mm.

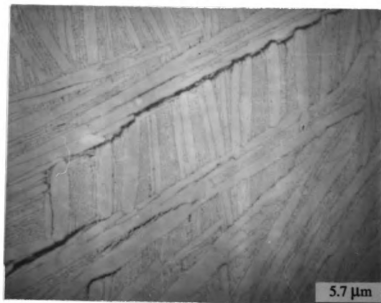


Figure 64. SEM micrograph showing carbide monoliths in hyper-eutectic structure.

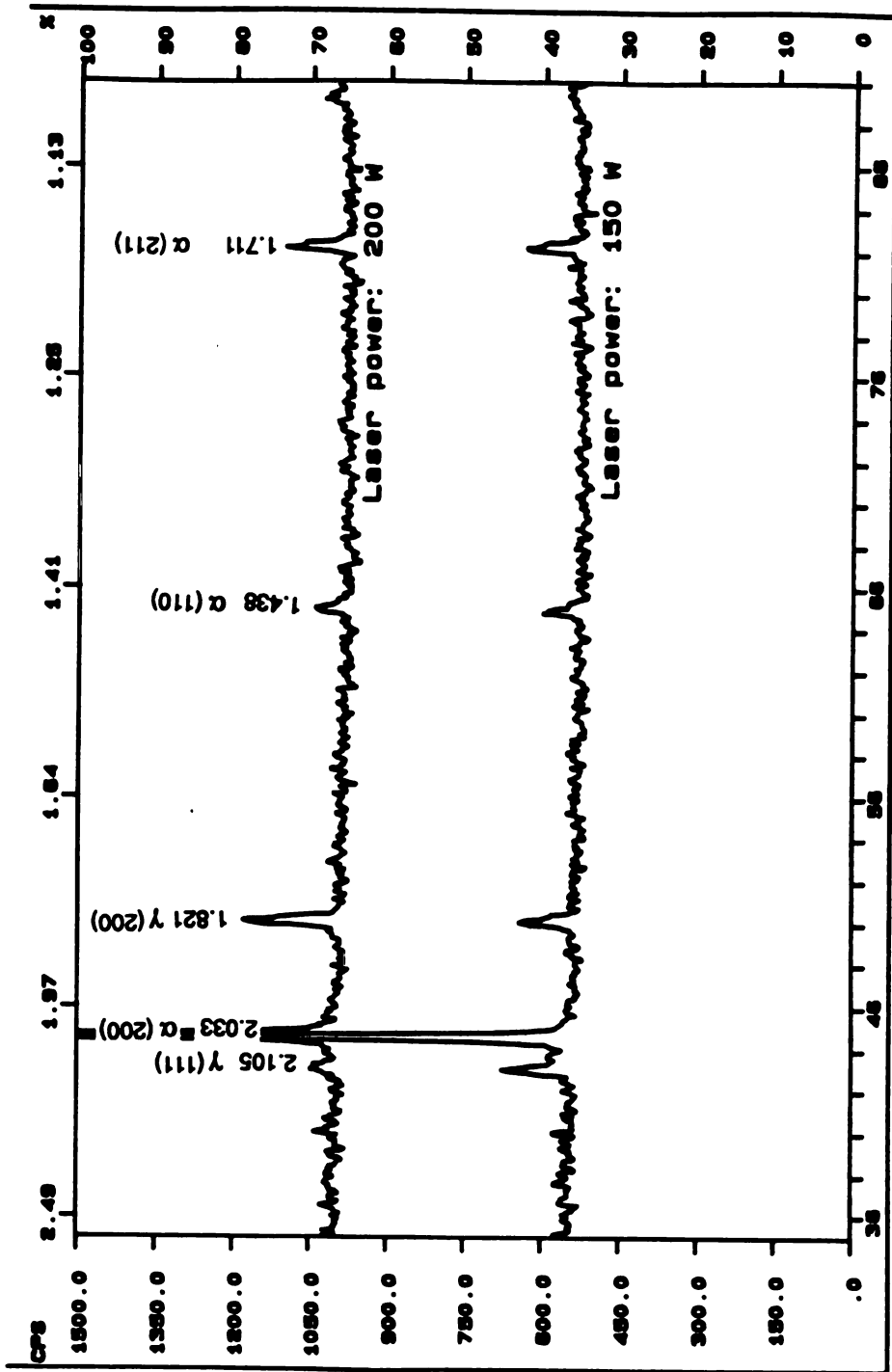


Figure 81. X-ray diffraction data from laser bordered zone, Process conditions for this sample are shown in figure 78.

analyzing x-ray diffraction peaks for austenite. X-ray analysis showed that the austenite contained approximately 2.16 wt % of carbon, as calculated from the following equation, relating austenite lattice parameter and carbon content [178].

$$a = 3.548 + 0.044X \quad (\text{EQ 4.2.2})$$

Where  $a$  is the lattice parameter in  $\text{\AA}$  and  $X$  is the weight percent of carbon in austenite. The  $M_s$  temperature for austenite containing ~2.16 wt % of carbon was estimated by using empirical formula, published by Kung et al [179], to be  $-218^\circ \text{C}$ . The calculated  $M_s$  temperature is thus, substantially below the liquid nitrogen temperature and therefore, no transformation of austenite occurred during liquid nitrogen quenching.

The secondary arm spacing of austenite dendrites were found to be in the range of 0.25-0.75 micro-meters. This data can be used to determine the cooling rate in the carburized zone, with the aid of data published by Morris [181] (for his work on laser melting of cast iron). The cooling rate  $\dot{T}$  (K/s) and the resulting secondary arm spacing ( $D$ ) (micron) are related by: [181]

$$D = 59 (\dot{T})^{-0.49} \quad (\text{EQ 4.2.3})$$

The above formula estimates the cooling rate, in laser carburizing, to be in the range of  $\sim 3 \times 10^4$  K/s. This rate was not high enough for amorphous solidification to occur [181]

#### 4.2.4 Limitations of laser carburizing

The problems encountered in laser carburizing are formation of pores and cracks in the laser carburized zones, under certain combination of process parameters. Figure 66 illustrates these problems. Pores are considered to be gas pores since the spherical geometry corroborates this argument. Binder emitted gas or air trapped in the pores of the powder (coating) caused such pores. This problem can be eliminated by using densely packed coating and drying the coating before laser carburizing. The more significant problem is the

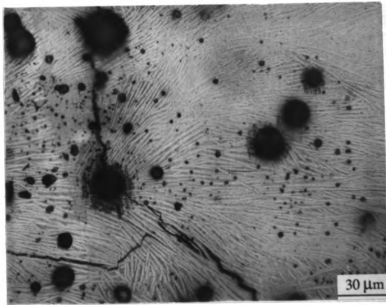
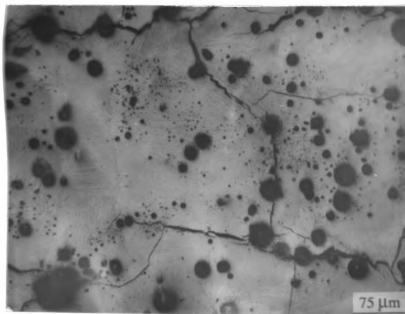


Figure 66. Micrograph showing the limitations of laser carburizing: porosity and cracks.

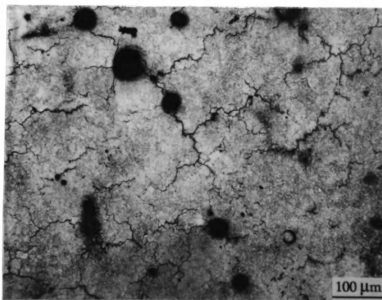
formation of cracks in some of the laser carburized microstructures. Two types of cracks have been observed: straight and wiggly cracks. Figure 67 shows typical straight and wiggly cracks.

**(a) Wiggly cracks:** Cracks referred in this section looks irregular at lower magnifications as shown in figure 67. Higher magnification micrographs (figure 68,69) show that these cracks are interdendritic or intergranular cracks. Figure 68 shows the crack around the dendrites of austenite, whereas figure 69 shows the cracks around martensitic packets. The following discussion explains the formation of such cracks. This type of crack forms at a temperature just above the solidus of the alloy. Normally the dendritically solidified metal is characterized by compositional difference between the dendritic core and the solute rich low melting interdendritic region. During last stages of solidification, a semi-rigid network of mechanically interlocked dendrites form with a small amount of, interdendritic, low melting point liquid. As the carburized zone shrinks during solidification, tensile stresses tend to pull the loosely bonded dendrites apart. This separation, if not filled up, results in wiggly cracks in the carburized zone.

The amount of interdendritic liquid is a critical factor in determining whether wiggly cracks will form or not. In the eutectic part of Fe-Fe<sub>3</sub>C diagram (figure 70), molten zone with carbon content C<sub>1</sub> solidifies in the portion of the phase diagram that is most susceptible to wiggly crack formation. This is because the amount of liquid remaining after an interdendritic separation or cracking is not sufficient to fill or heal the crack, as a riser would in a casting. If the molten zone with carbon content C<sub>2</sub> solidifies, a plentiful amount of liquid remains just before the eutectic temperature to heal any interdendritic crack that may form. Finally, the molten zone with carbon content C<sub>3</sub> is virtually immune to wiggly crack formation, because each dendrite is surrounded by the eutectic liquid that solidifies at one temperature and provides ample eutectic healing of any dendritic separation.



(a)



(b)

Figure 67. Micrograph showing typical (a) straight cracks, and (b) wiggly cracks.

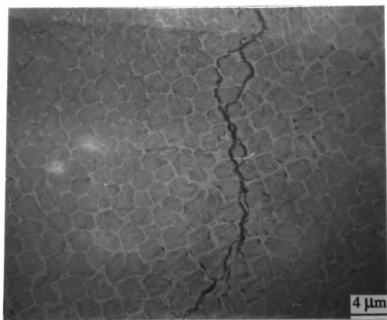


Figure 68. SEM micrograph showing wiggly cracks around austenite dendrites.

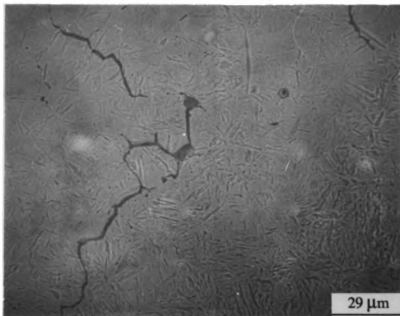


Figure 69. SEM micrograph showing wiggly cracks (intergranular, along prior austenite grain boundaries).

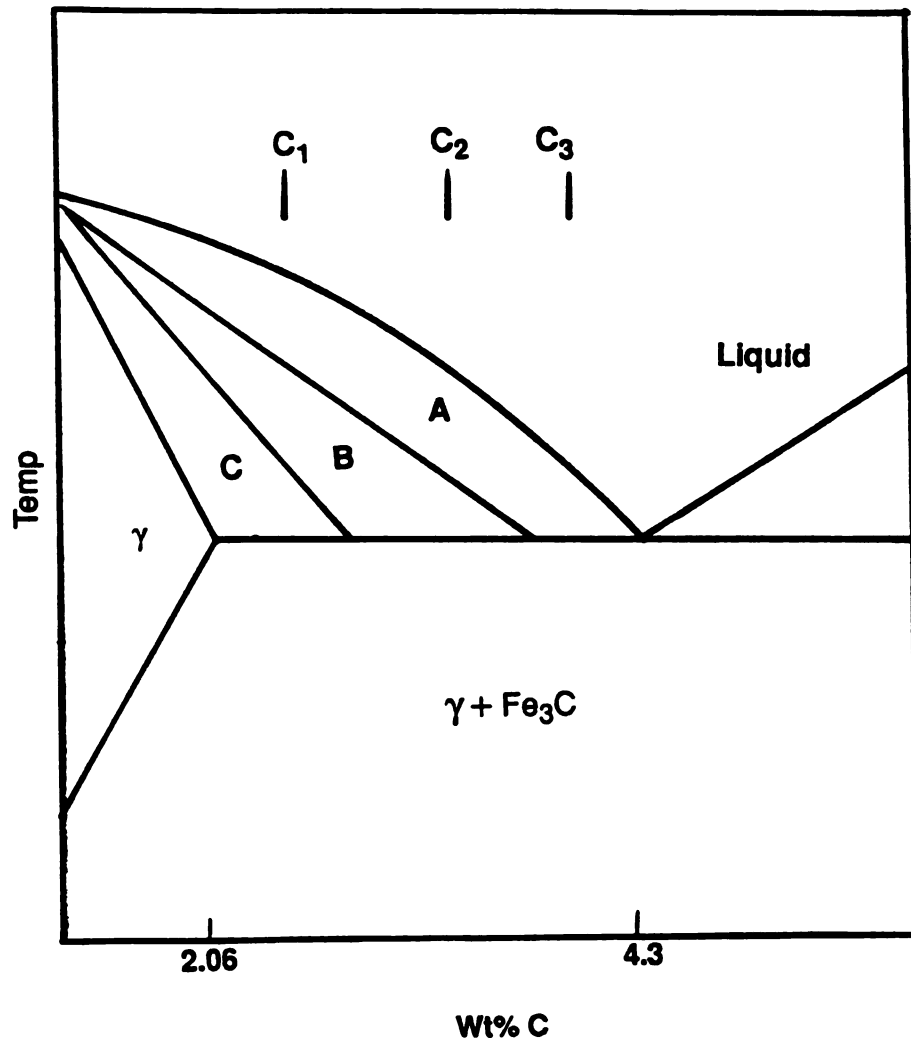


Figure 70. Effect of composition on wiggly cracking susceptibility of laser carburized zone. Regions of crack susceptibility: A no cracking; B liquid healing possible; C crack sensitive.

**(b) Straight Cracks:** This type of cracks have been predominantly observed in hypereutectic structures, developed by laser carburizing. These cracks are caused by thermal stresses after the formation of hypereutectic structure. The negligible ductility of  $\text{Fe}_3\text{C}$  plates makes them vulnerable to the thermal cracking. Both modes of cracking: intergranular or transgranular have been observed. Figures 71, 72 and 73 show the typical straight cracks produced in the laser carburized zone. Figure 71 shows the transgranular (trans-plate) crack where as figure 72 shows the intergranular crack. Figure 73 shows the mixed mode straight cracking. The crack's orientation in the carburized zone was such that they were caused by thermal stresses: in the direction parallel to laser traversal direction and in the direction transverse to the laser traversal. No cracks, parallel to surface, were seen in the transverse sections which indicated that thermal stresses in the depth direction of specimen were insignificant.

The generation of thermal stresses (tensile stresses) during laser carburizing can be understood by considering figure 74. As a laser carburized zone cools rapidly from melt temperature, the surface and interior (subsurface layers) contract at different rates (as illustrated in figure 74). Now since in laser carburizing the bulk of the sample stays at room temperature, the interior of the melted region cools faster because of the thermal sink of the bulk. At some time A (figure 74) this difference, coupled with the low material yield strength associated with the high temperature, induces plastic flow or permanent yielding. The difference in contraction of the surface and interior tend to be equalized by the plastic flow. The decrease in the length of the surface at time t can be noticed in figure 74. Continuing along the cooling curve (since the surface is warmer than the interior) its subsequent contraction during cooling is greater (time B). Since it is constrained by the interior, the tensile stresses arise at the surface of the carburized zone. Now these tensile stresses will cause straight cracks if the fracture strain of the surface microstructure is less than the

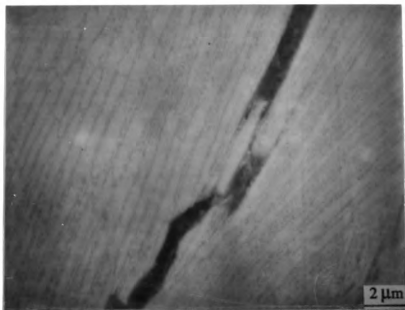


Figure 71. SEM micrograph showing intergranular cracking (straight) in iron carbide needles. Laser power 100 W, traverse speed 3.88 mm/s, and graphite layer thickness 0.41 mm.

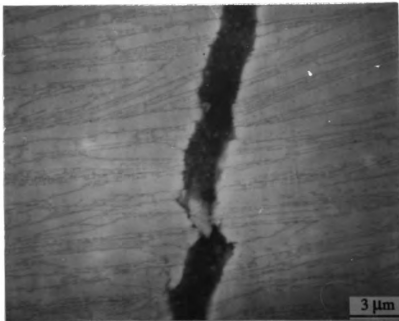


Figure 72. SEM micrograph showing transgranular cracking (straight) in iron carbide needles. Process conditions same as in figure 71.

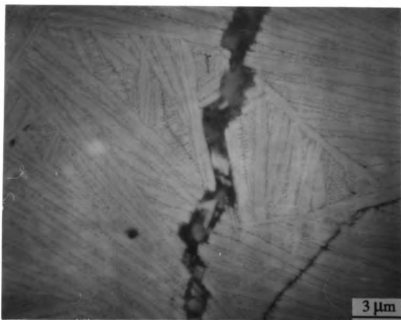


Figure 73. SEM micrograph showing the mixed mode cracking in iron carbide needles. Laser power 100 W, traverse speed 3.88 mm/s, and graphite layer thickness 0.41 mm.

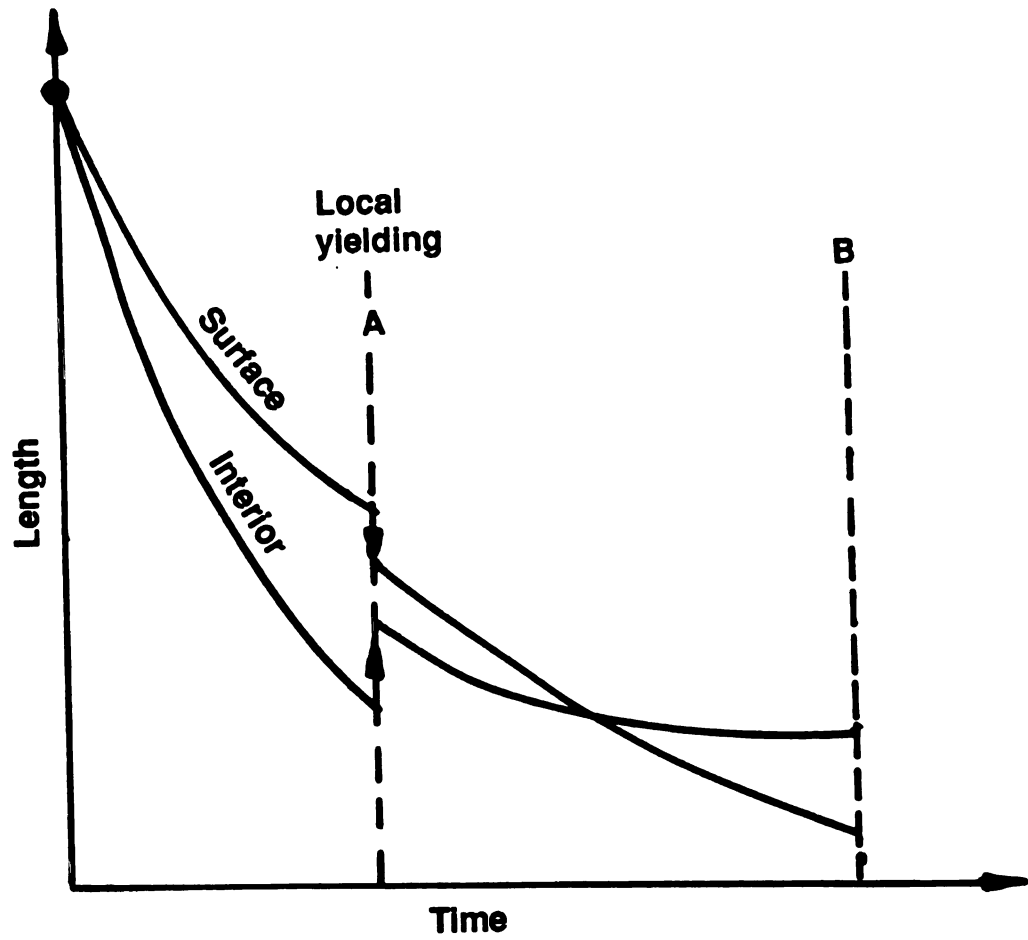


Figure 74. Schematic cooling curves showing the difference in contraction of the surface and interior.

stress caused by the tensile stress. For example if the carburized zone contains 100% Fe<sub>3</sub>C microstructure, the fracture strain will be ~.004, which is considerably lower than that for a ductile phase like austenite (fracture strain ~0.3).

From the above discussion, it is seen that straight cracks occur because of the brittleness of the hypereutectic structure (very low fracture strain), which cannot bear the thermal stress generated during cooling. The best microstructure (with respect to crack free and high hardness) which can form during laser carburizing is the mixture of the austenite dendrites with interdendritic eutectic. No cracks were observed because of the effective ductility of the composite structure of hardened (due to super saturation of carbon) but ductile austenite dendrites in the matrix of eutectic. A second approach to minimizing the straight cracks, in the carburized zone, can be preheating the substrate. In the past, investigators have minimized thermal stresses in the brittle coatings, such as TiC and SiC, by preheating the substrate [183].

### **4.3. Laser Boriding**

#### **4.3.1 Microstructural studies**

Although by laser carburizing of AISI 1018 steel, high hardness of 1050 Hv has been obtained, it was observed that further increase in hardness can be achieved by laser boriding. Figure 75 shows the comparison between the hardness profile at the HAZ, achieved during laser carburizing and laser boriding of AISI 1018 steel respectively. Laser carburizing (in figure 75) was carried out at a laser power of 150 watts, traverse speed of 4.32 mm/s was used, and a graphite coating thickness of 0.2mm was applied. Laser boriding (figure 75 ) was achieved by using 6 cycles of laser passes at a laser power of 150 watts on a boron powder coated surface. Figure 75 shows the evidence of formation of well docu-

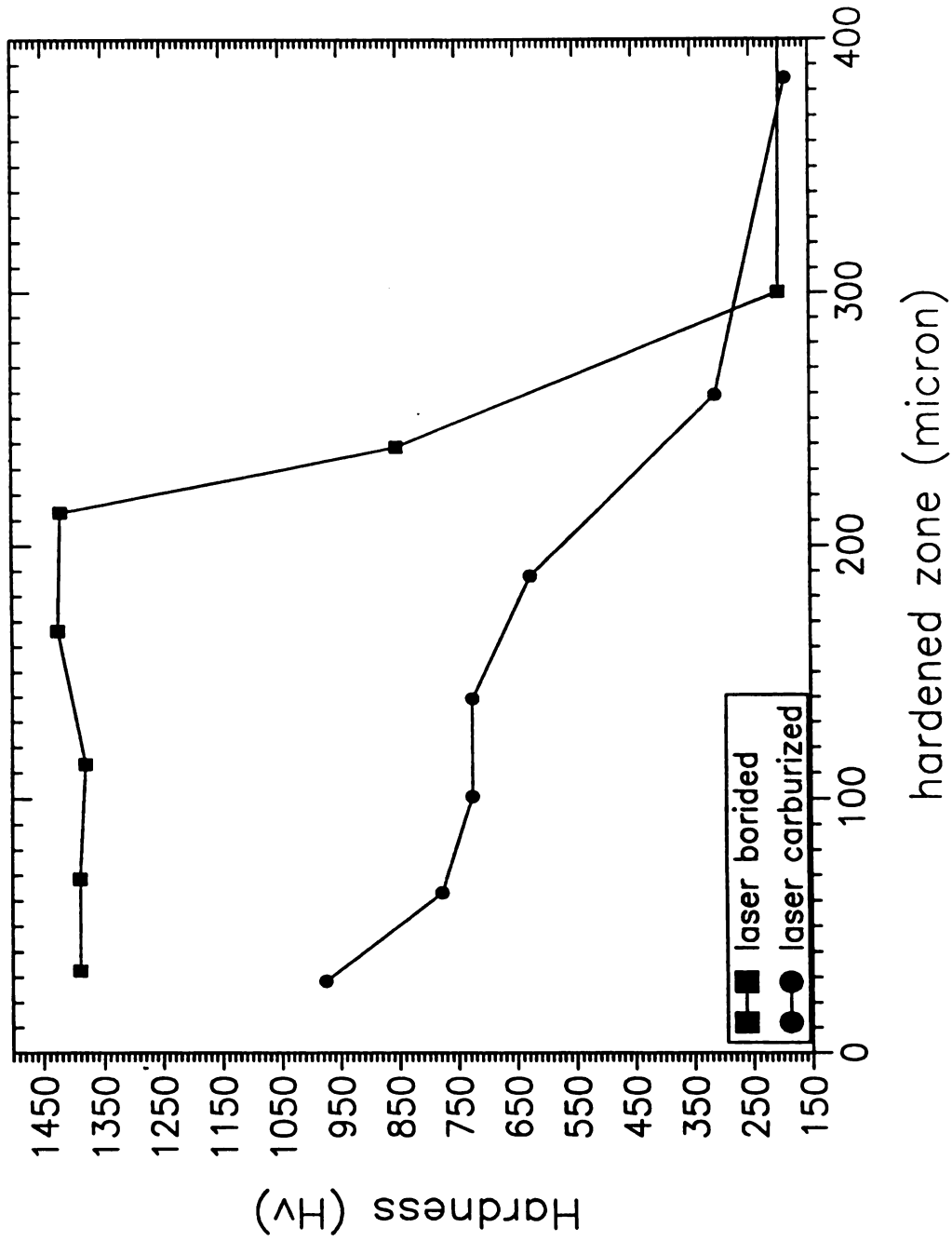


Figure 75. Comparison of hardness profiles at the transverse section of samples, treated by laser carburizing and laser boriding.

mented hard borides [184,185,187], on the surface of a laser borided sample.

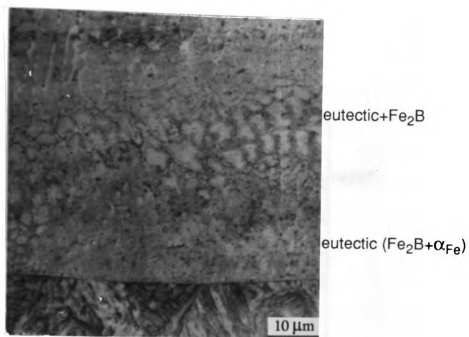
A series of microstructures have been observed on the laser borided surface, depending on laser parameters and boron coating thickness. The laser process parameters basically control the amount of boron dissolved in the laser melted surface and the solidification behavior. Figure 76 shows a typical microstructure of a laser borided zone. The laser borided microstructure, shown in figure 76, was obtained by two passes of a laser beam on a boron coated 1018 steel sample. The process parameters are shown in the caption of the figure. Characterization of the various zones in the microstructure, in figure 76, can be done by reviewing the iron-boron equilibrium phase diagram (figure 77) [185 ], even though the solidification conditions are non-equilibrium. Four distinct zones can be seen from figure 76.

**(i) HAZ martensite :** This zone consists of low carbon martensite. Coarse martensite has a low hardness of ~390 Hv.

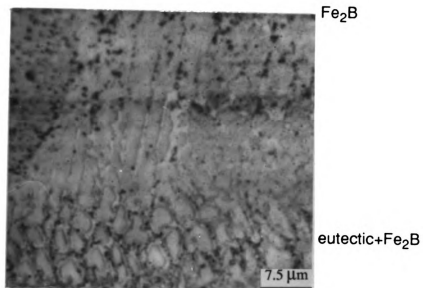
**(ii)Eutectic ( $\alpha_{Fe}$  &  $Fe_2B$ ):** This zone consists of planar looking eutectic. SEM examination showed that this zone consisted of fine lamellae of  $\alpha_{Fe}$  and  $Fe_2B$ . The microhardness was found to be about 900 Hv. A sharp boundary between this phase and the unmelted substrate can be seen from the figure 76a.

**(iii) Mixture of eutectic and  $Fe_2B$ :** Boron concentration in this zone was between 4 and 8.5 wt%. Figure 76b shows cellular dendrites of  $Fe_2B$  surrounded by eutectic. The microhardness in this zone was found to be about 1100 Hv.

**(iv) Single phase  $Fe_2B$ :** This zone consisted of mostly  $Fe_2B$  phase surrounded by very small amount of eutectic (figure 76b). In this zone the boron concentration was approxi-

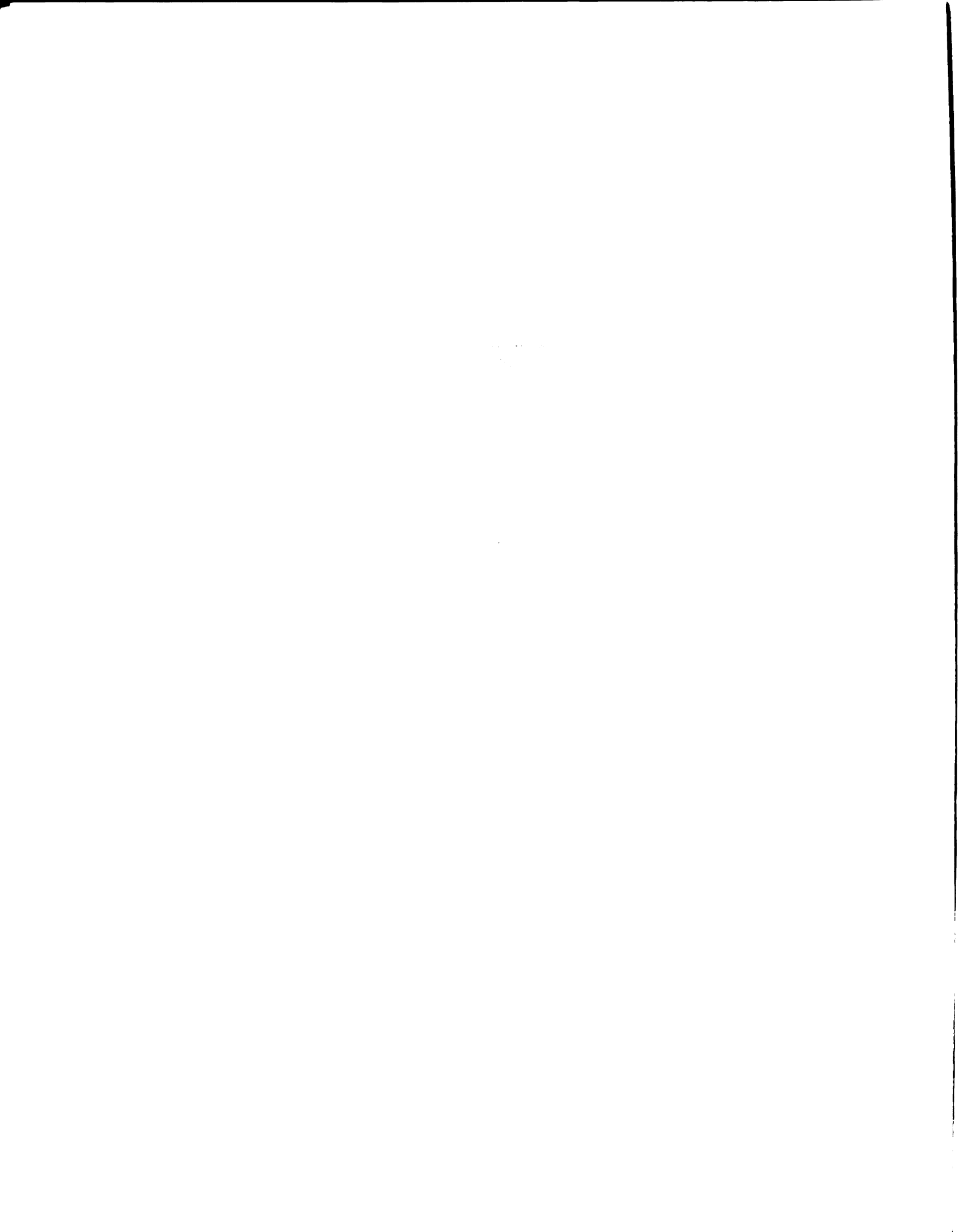


(a)



(b)

Figure 76. Typical microstructure of laser borided zone (a). Two passes of laser (200 W), boron layer thickness 0.30 mm, and traverse speed 2 mm/s (b) Magnified top left portion of (a).



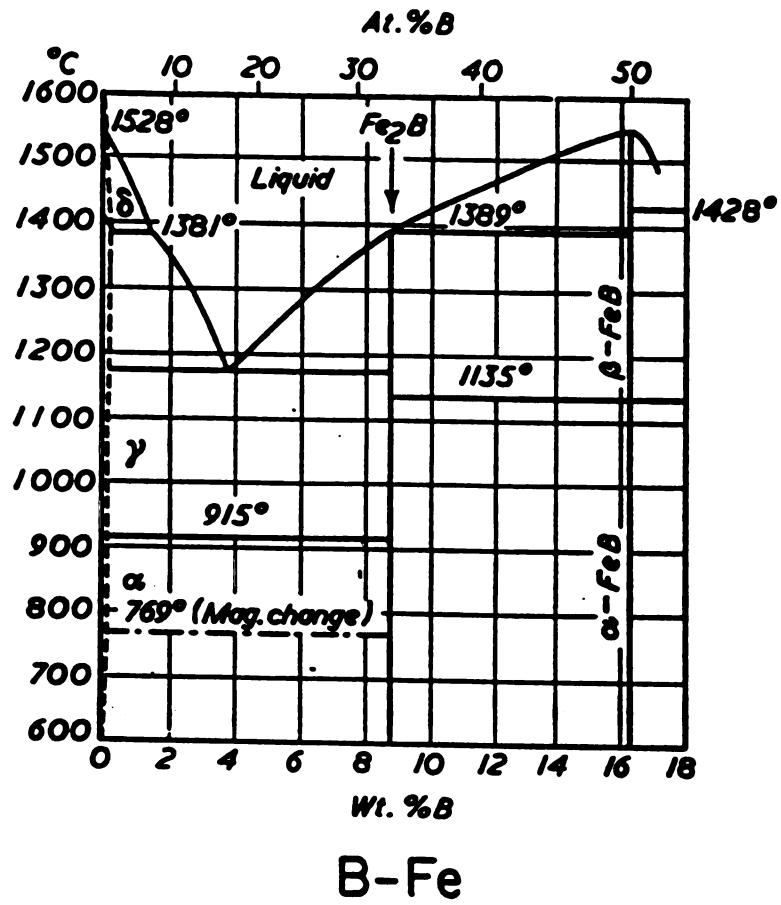


Figure 77. Fe-B equilibrium diagram. [185]

mately 8.5 wt%.

No evidence of the presence of solid solution of boron in iron was found close to the substrate, which shows minimum diffusion of boron in the parent phase, during laser boriding. No evidence of FeB was found in the borided zone shown in figure 76. This shows a significant loss of boron due to evaporation during laser boriding, hence not enough supply of boron to form FeB. Further saturation of boron was achieved by adding a boron layer repetitively during each pass of laser. Figure 78 shows the microstructure which evolved due to the high concentration of boron in surface layers of the laser borided specimens. For the microstructure in figure 78, three successive cycles of boron coating (~0.38 mm) and laser melting were applied. The laser power used was 200 watt and traversal speed was 2.0mm/s. Additional features observed in figure 78, as compared to figure 76 are:

- (a) **FeB phase:** At the surface of borided layer, a FeB phase was observed, due to high saturation of boron. The volume fraction of FeB on top of the microstructure was ~0.98, which indicates that boron concentration in the surface of the borided layer, was approximately 16.5 wt%. Microhardness of FeB ranged from 1900 to 2200 Hv.
- (b) **Mixture of FeB and Fe<sub>2</sub>B:** Next to almost pure FeB phase, moving towards the substrate, a gradual decrease of FeB and an increase of Fe<sub>2</sub>B phase was observed. This indicates that there is an increasing dilution of boron inside the laser borided zone. The boron concentration in this zone was in the range 8.5-17.0 wt%.

Borided microstructure, shown in figure 78, has been found to be quite hard as compared to the borided structure shown in figure 79. This is due to the significant fraction of FeB in the microstructure shown in figure 78 ( which is considered to be the hardest phase in Fe-B system). On the other hand, a mixture of Fe<sub>2</sub>B and eutectic present in microstructure shown in figure 79, is relatively softer than the FeB phase. The process cycle for the micro-

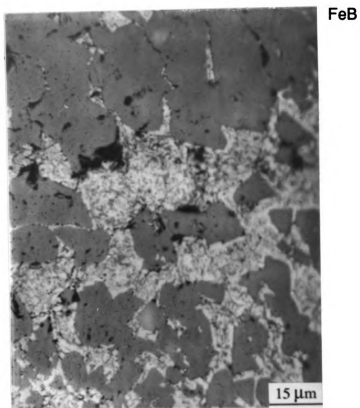


**Figure 78.** Laser borided microstructure showing features in addition to ones shown in figure 76. 3 cycles of laser pass (200 W) and boron coating at traverse speed of 2 mm/s.

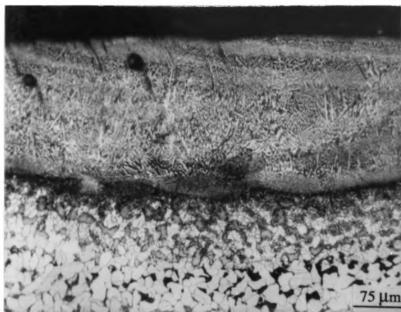


Figure 79. SEM micrograph of transverse section of laser borided zone, showing softer microstructure: a mixture of Fe<sub>2</sub>B and eutectic. Two passes of laser (200 W) on boron coated (0.18 mm) sample, with traverse speed of 2 mm/s.

structure shown in figure 79 was: two passes of laser beam (200 watt) on the boron coated (.18mm) sample. This treatment causes extensive dilution of boron, resulting in the evolution of the relatively softer phases; eutectic ( $\alpha_{Fe}$  &  $Fe_2B$ ) and  $Fe_2B$ .

#### 4.3.2 Hardness profile study

Figure 80 shows the hardness profiles of laser borided specimens, treated under different conditions of process parameters. These profiles basically show the effect of various microstructures, formed under different conditions of laser process parameters, on the hardness distribution at the borided zone. A notation system of x-y-p-t has been used to denote processing parameters in figure 80, where x denotes the number of times boron coating was laid, y denotes the number of laser passes, p denotes the laser power (watts) and t is the thickness (in mm) of boron coating. Highest hardness has been achieved in case of the sample for which x=3, y=3, p=200 watts and t=0.38mm. The high hardness of 2150 Hv matches with the hardness of the single phase  $FeB$ . The lowest hardness of 950 was observed in case of the sample with x=1, y=2, p=200 watts and t=0.18mm. This lower hardness matches approximately with the hardness of a single phase eutectic ( $\alpha_{Fe}$  &  $Fe_2B$ ). Increasing the saturation of boron in the borided zone, resulted in the hardness profile, shown for samples 1-2-200-.28 and 2-2-200-0.38. In case of sample 1-2-200-0.28, the microstructure consisted of mostly  $Fe_2B$ , whereas in sample 2-2-200-0.38, which has a hardness in between the hardness of samples 3-3-200-0.38 and 1-2-200-0.28, the microstructure consisted of mixture of  $Fe_2B$  and  $FeB$ .

#### 4.3.3 Phase and composition analysis

Phase analysis in the laser borided samples, were done by using a Scintag x-ray diffractometer fitted with copper target tube. Figure 81 shows the x-ray diffraction peaks for a laser

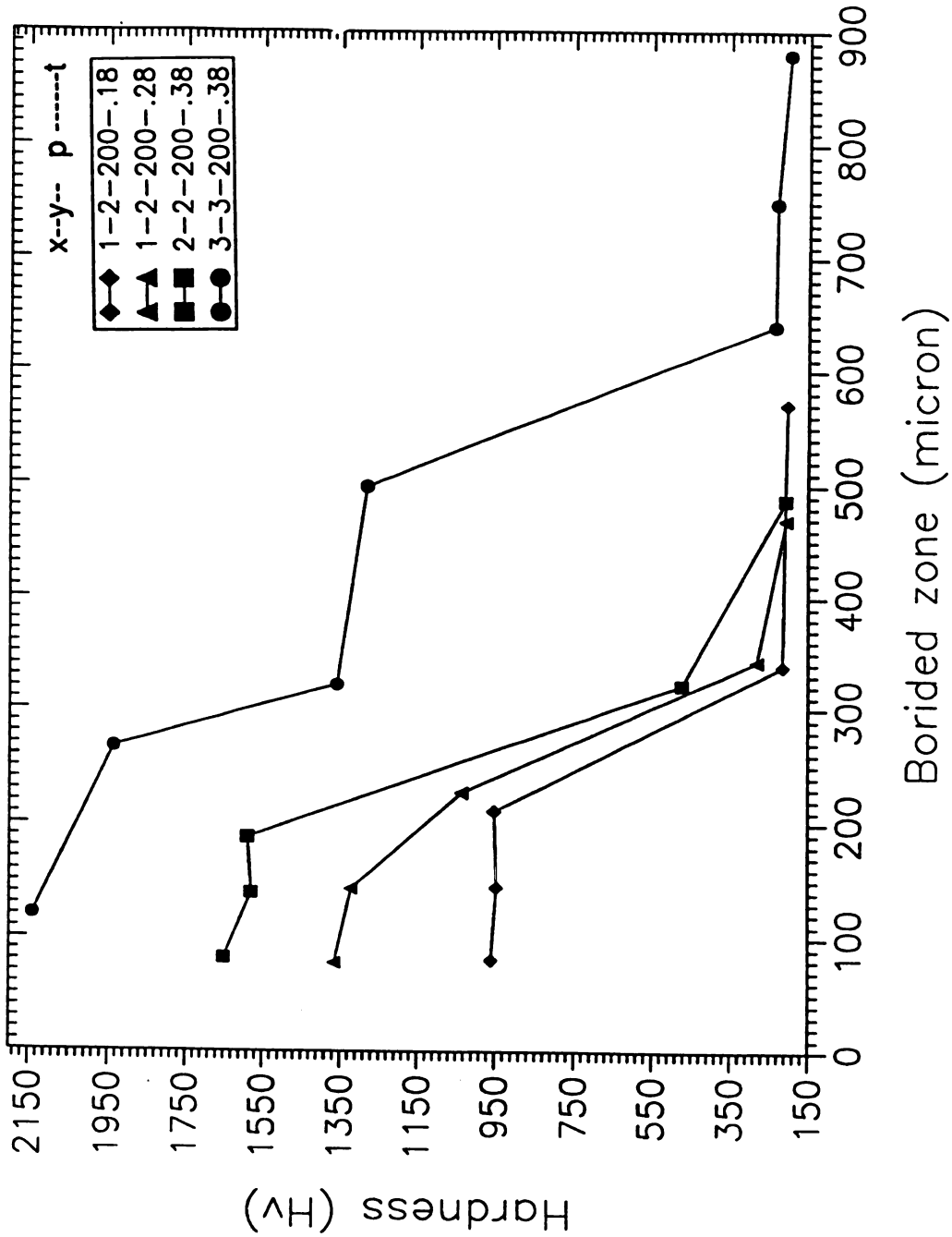


Figure 80. Hardness profiles at the transverse section of laser borided samples treated under different process conditions. In this figure x is the the number of times boron coating was layed, y is the number of laser passes, p is the laser power (watts) and t is the thickness (mm) of boron coating.

borided sample, which was treated with two passes of the laser beam and two successive layers of boron coating. Most of the peaks in the diffraction pattern, shown in figure 81, were identified to be from FeB. Remaining peaks were from Fe<sub>2</sub>B. No evidence of amorphous phases were found in the layers, as has been reported for Fe-B system [188,189,190]. This absence of amorphous phase could be attributed to the cooling rate, which is attained during our conditions of laser processing. Normally glass forming process requires a rapid cooling rate of approximately  $\sim 10^8$  K/s [90], but our process conditions only achieved a cooling rate approximately  $\sim 10^4$  K/s (as discussed in section 4.2.3).

Figure 81 showed the evidence of texture formation in the laser borided zone. Both FeB and Fe<sub>2</sub>B phases exhibited a sharp texture. The FeB was found to be preferentially oriented in  $\langle 111 \rangle$  texture, whereas the Fe<sub>2</sub>B phase shows a  $\langle 002 \rangle$  texture. The degree of texture in Fe<sub>2</sub>B was studied using the ratio R of the diffracted intensities corresponding (002) and (201) peaks. For a randomly oriented Fe<sub>2</sub>B, ratio the value of this R is 0.25. The value of R was found to be 0.67 for Fe<sub>2</sub>B (from figure 81) in borided zone, indicating a significant texture in the borided zone. In addition to Fe<sub>2</sub>B, FeB has also been found to have a significant texture. The degree of texture in FeB was determined by using the intensity ratio of the (111) and (021) diffraction peaks. R was found to be 1.5 for FeB (from figure 81) as compared to the ratio of 0.72, for randomly oriented FeB.

Concentration of boron in laser borided zones was determined by using an ARL (Applied Research Laboratories) electron micro probe. The measurements for Bk<sub>α</sub> were obtained using lead stearate crystal (Pb-St) analyzer. Figure 82 shows the boron and iron mapping of a transverse section of a laser borided specimen. It shows two phases, one richer in boron than the other. Individual total counts for boron in each phase were used to approximate the composition of the phase. The boron rich phase (16.3 wt% B) was found to be approximately matching the composition of FeB (16.9wt%). The composition of boron deficient

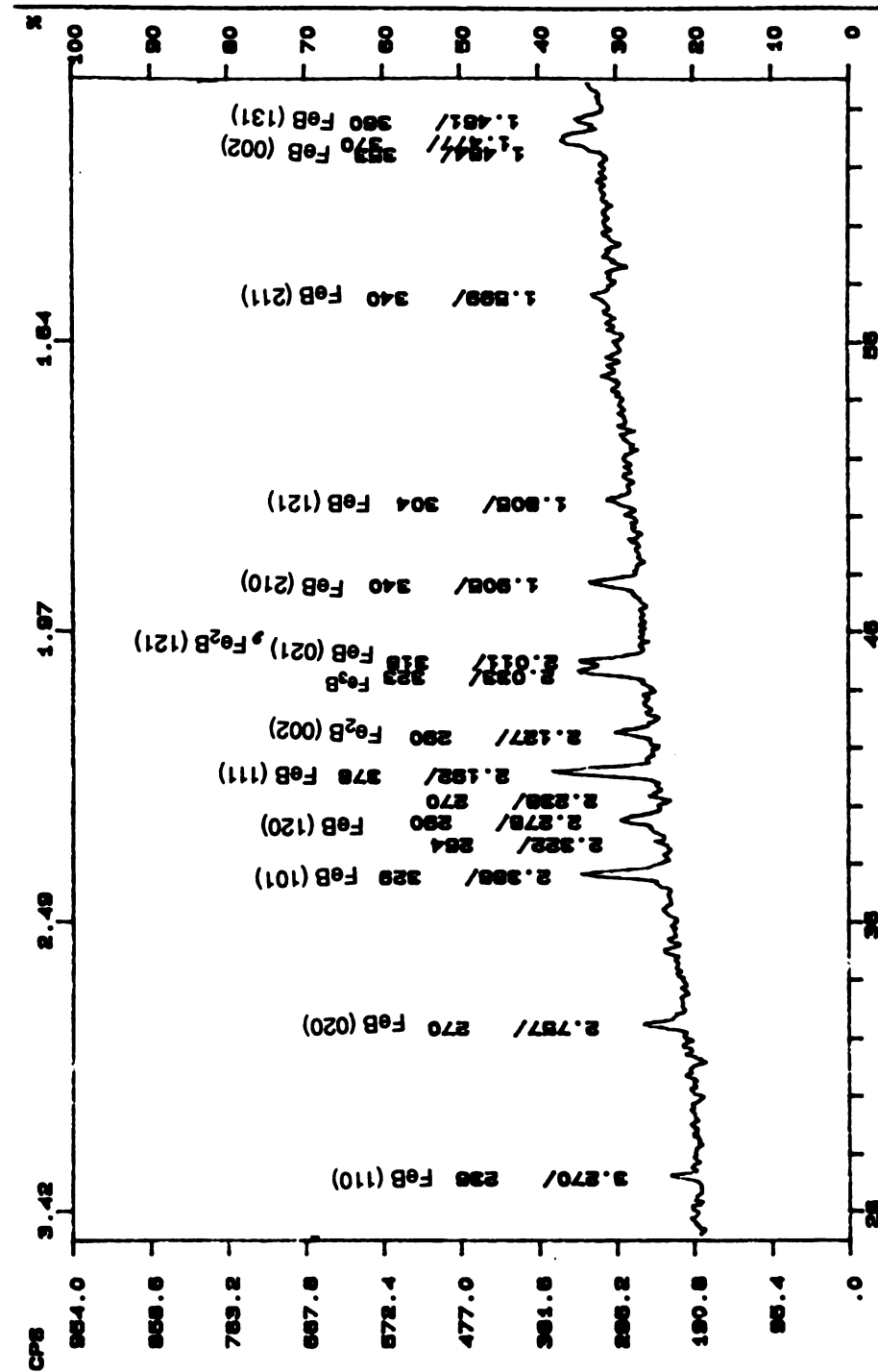


Figure 65. X-ray diffraction data from laser carburized zone.

phases was found to match approximately with the composition of a peritectically formed  $\text{Fe}_2\text{B}$ . Figure 83 shows the boron and iron mapping in the area interior to the one shown in figure 82. The microstructure in figure 83 shows more of a boron deficient phase than the boron rich phase. Again, by individual total counts for boron, these phases were consistent with the stoichiometry of  $\text{Fe}_2\text{B}$  and  $\text{FeB}$  respectively.

#### 4.2.4 Stress states in laser borided layer

Cracks were observed in borided zones with almost 100%  $\text{FeB}$  phase, but no cracks were detected in the borided zones with  $\text{Fe}_2\text{B}$  phase. The crack formation in borided layer is thought to be due to the thermal stresses, since no solidification cracking was observed. Now, one of the important variables controlling the magnitude of the thermal stress, is the thermal expansion coefficient. After examining the thermal expansion coefficients of  $\text{FeB}$ ,  $\text{Fe}_2\text{B}$  and AISI 1018 steel, shown in table 4.1, an important information has been extracted.

**Table 3. Values of thermal expansion coefficients ( $\text{K}^{-1}$ ) [184]**

Material	Thermal expansion Coefficient ( $\text{K}^{-1}$ )
$\text{FeB}$	$8.7 \times 10^{-8}$
$\text{Fe}_2\text{B}$	$2.9 \times 10^{-8}$
AISI 1018	$5.7 \times 10^{-8}$

If the surface of the laser borided sample contains mostly  $\text{FeB}$  phase, then the surface will try to contract much more during cooling than the sample with only  $\text{Fe}_2\text{B}$  phase or steel. Therefore the result will be a tensile stress and it will be more prone to cracking. On the other hand, the coefficient of expansion of  $\text{Fe}_2\text{B}$  is less than that of steel, and hence it con-

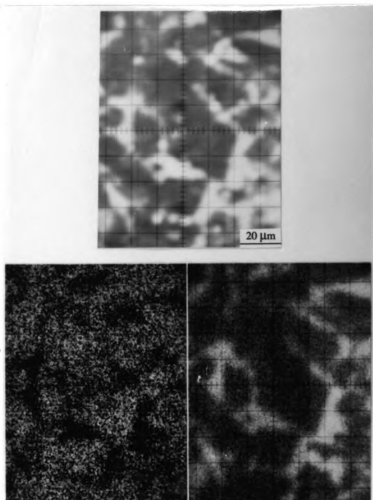


Figure 82. Micrograph showing boron and iron mapping in an area near the surface (in transverse section) of laser borided sample. Bigger grains are found to be FeB and smaller grains are Fe<sub>2</sub>B. (sample from figure 78). (a) main photograph, (b) boron mapping, and (c) iron mapping.

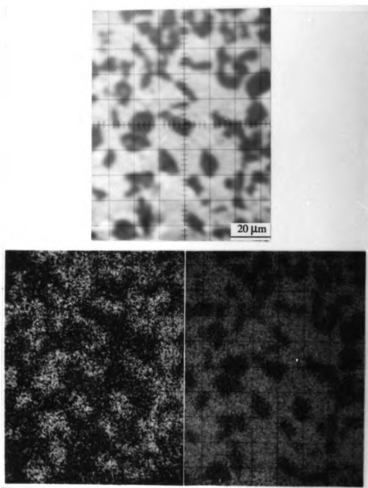


Figure 83. Micrograph showing boron and iron mapping in an area away from surface (in transverse section) of laser borided sample. Grains are found to be FeB and Fe<sub>2</sub>B. (sample from figure 78). (a) main micrograph, (b) boron mapping, and (c) iron mapping.

tracts less during cooling. This puts the  $\text{Fe}_2\text{B}$  layer in a compression state after cooling. This analysis, along with the experimental results of laser boriding, demonstrates that the best microstructure in laser borided layer should be the single phase  $\text{Fe}_2\text{B}$ .  $\text{Fe}_2\text{B}$  in microstructure imparts ideal properties to the laser borided layer: a high hardness (1200-1600 Hv) and a favorable state of compressive stress.

#### **4.4 A new Approach to Temperature Distribution Modelling During Laser hardening**

The laser surface treatment relies on the modification of the surface by altering microstructure and or composition. This, in turn, is controlled by the distribution of temperature on the surfaces, to be laser treated. Normally, measurement of temperature variation during laser surface treatment is not possible because of the high temperature variation rate.

Hence there is a need of theoretical models to predict temperature distribution during laser surface treatments. A simple analytical model, using Green's function, has been developed for temperature distribution, due to a stationary laser. A FORTRAN program has been developed to solve this problem. The proposed solution can be used to describe the transient temperature distribution, due to the heating produced by directed laser beam.

In order to be efficient in description and solution of the problem, the notation system proposed by Beck [191] is used. For a one dimensional plate problem the system X is followed by two numbers, one for each boundary condition, numeral 1 is used for a prescribed temperature, 2 is used for a prescribed heat flux and 3 is used for a convective condition. If there are no physical boundary conditions (i.e. natural boundary condition such as going to infinity), a 0 is used. For two and three dimensional problems, Y is used for the y direction and Z for the z direction. These notations can be used, along with Green's function, to obtain solution for the temperature distribution.

#### 4.4.1 Physical definition of the process

A stationary laser beam with uniform power distribution strikes the surface of a plate. Shape of the laser source is considered to be a square, with a finite dimension on each side. The plate, used in the model, was assumed to be rectangular, with dimensions  $L_x$  in x direction,  $L_y$  in y direction and  $L_z$  in z direction. The geometry of the plate (with the schematic of the physical definition of the process) is shown in figure 84. Heating is assumed to be only over the surface ( $y=0$ ), where the laser interacts. Elsewhere, the surface is assumed to be insulated. On the lower surface ( $y=L_y$ ), there is assumed to be a convective boundary condition. The temperature distribution is found by assuming temperature independent thermal properties like thermal conductivity, density and specific heat. These assumptions linearize the problem, so that an analytical solution is possible.

#### 4.4.2 Mathematical definition of the process

A finite plate is described by a region  $0 < x < L_x$ ,  $0 < z < L_z$ , and  $0 < y < L_y$ ; where the region  $x_1 < x < x_2$ ,  $z_1 < z < z_2$  is exposed to a constant heat flux of  $q_0$ . The relevant heat conduction parameters are shown in figure 84. The basic heat transfer equation is given by:

$$\alpha \left( \frac{\delta^2 T}{\delta x^2} + \frac{\delta^2 T}{\delta y^2} + \frac{\delta^2 T}{\delta z^2} \right) = \frac{\delta T}{\delta t} \quad (\text{EQ 4.4.1})$$

The boundary conditions are given by:

$$-K \left( \frac{\delta T}{\delta y} \right) \Big|_{y=0} = \begin{cases} q_0 & x_1 < x < x_2 \text{ and } z_1 < z < z_2 \\ 0 & \text{elsewhere} \end{cases} \quad (\text{EQ 4.4.2})$$

$$\left( \frac{\delta T}{\delta x} = 0 \right), \quad \text{at } x=0 \text{ and } x=L_x \quad (\text{EQ 4.4.3})$$

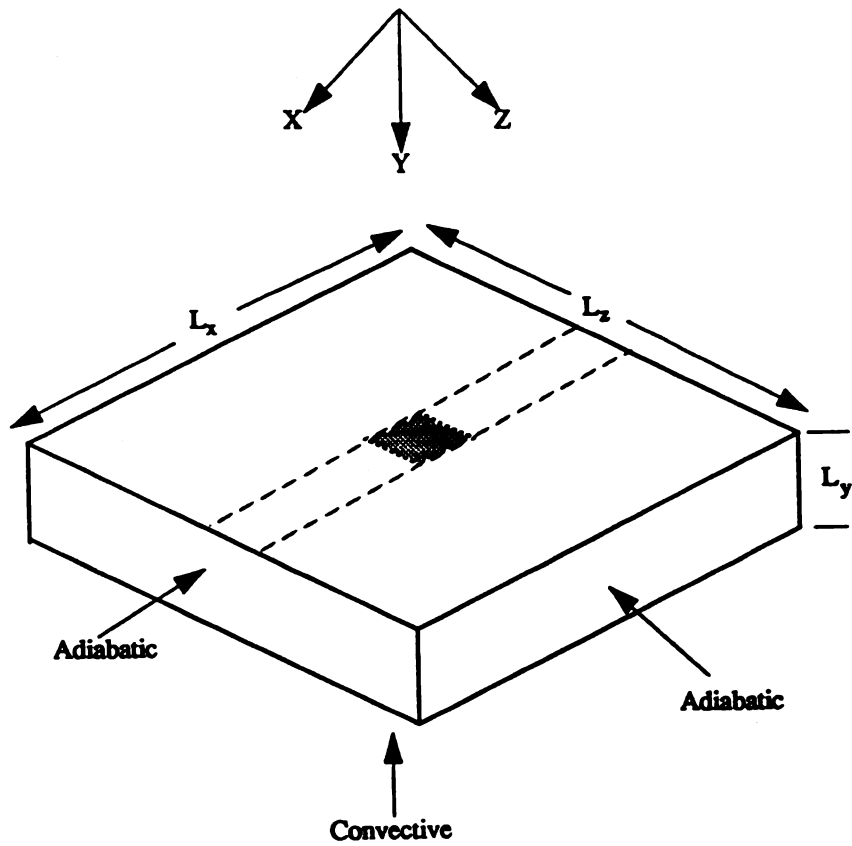


Figure 84. Schematic diagram illustrating the various dimensions, coordinates and boundary conditions for the laser surface processing heat transfer model.

$$\left(\frac{\delta T}{\delta z} = 0\right), \quad \text{at } z=0 \quad \text{and } z=L_z \quad (\text{EQ 4.4.4})$$

$$-K \left(\frac{\delta T}{\delta y}\right) \Big|_{y=L_y} = hT \quad (\text{EQ 4.4.5})$$

and the initial condition is  $T(x, y, z, t) = 0$ ,

where T is the temperature: x,y and z are the cartesian coordinates; t is time,  $\alpha$  is the thermal diffusivity, h is the heat transfer coefficient,  $L_x$ ,  $L_y$  and  $L_z$  are the dimensions of sample (as shown in figure 84), and K is the thermal conductivity of the plate material.

#### 4.4.3 Derivation of the model

The temperature distribution, in terms of Green's function can be given by[192]

$$T(x, y, z, t) = \frac{\alpha q_o}{K} \int_{\Delta\tau} \int_{x_1}^{x_2} \int_{z_1}^{z_2} G_{x_2z_2y_2z_3} \left(\frac{x, z, y, t}{x', z', 0, \tau}\right) dx' dz' d\tau \quad (\text{EQ 4.4.6})$$

Where  $G_{x_2z_2y_2z_3}(\ )$  is the Green's function for the  $x_2z_2y_2z_3$  geometry. The multiplicative property of Green's function permits writing

$$G_{x_2z_2y_2z_3} \left(\frac{x, z, y, t}{x', z', 0, \tau}\right) = G_{x_2z_2} \left(\frac{x, t}{x', \tau}\right) G_{z_2z_3} \left(\frac{z, t}{z', \tau}\right) G_{y_2z_3} \left(\frac{y, t}{0, \tau}\right) \quad (\text{EQ 4.4.7})$$

The  $G_{z_2z_3}(\ )$  is the Green's function for the one dimensional geometry of plate with insulation condition at  $z=0$  and  $z=L_z$ . The  $G_{y_2z_3}(\ )$  is the Green's function for the one dimensional geometry of plate with insulation at  $y=0$  and convective boundary condition at  $y=L_y$

The  $G_{z_2z_3}(\ )$  function is given exactly by [192].

$$G_{z_2z_3} \left(\frac{z, t}{z', \tau}\right) = \frac{b}{L_z} + \frac{2}{\pi} \sum_{n=1}^{\infty} \frac{1}{n} e^{-n^2 \pi^2 \alpha \frac{(t-\tau)}{L_z^2}} \cos\left(\frac{n\pi z}{L_z}\right) \sin\left(\frac{n\pi b}{L_z}\right) \quad (\text{EQ 4.4.8})$$

where  $n$  is the summation variable;  $b$  is the laser beam size in the  $z$  direction,  $G_{z22}(\cdot)$  can be simplified for our case as

$$\int_{z_1}^{z_2} G_{z22} \left( \frac{z, t}{z', \tau} \right) dz' = \frac{z_2 - z_1}{L_z} + \frac{2}{\pi} \sum_{n=1}^{\infty} \frac{1}{n} e^{-n^2 \pi^2 \alpha \frac{(t-\tau)}{L_z^2}} \cos \left( \frac{n\pi z}{L_z} \right) \times \left[ \sin \left( \frac{n\pi z_2}{L_z} \right) - \sin \left( \frac{n\pi z_1}{L_z} \right) \right] \quad (\text{EQ 4.4.9})$$

Similar to the above equation we get  $G_{x22}(\cdot)$

$$\int_{x_1}^{x_2} G_{x22} \left( \frac{x, t}{x', \tau} \right) dx' = \frac{x_2 - x_1}{L_x} + \frac{2}{\pi} \sum_{m=1}^{\infty} \frac{1}{m} e^{-m^2 \pi^2 \alpha \frac{(t-\tau)}{L_x^2}} \cos \left( \frac{m\pi x}{L_x} \right) \times \left[ \sin \left( \frac{m\pi x_2}{L_x} \right) - \sin \left( \frac{m\pi x_1}{L_x} \right) \right] \quad (\text{EQ 4.4.10})$$

The  $G_{y23}(\cdot)$  function is given exactly [191] after setting  $y'=0$ :

$$G_{y23} \left( \frac{y, t}{0, \tau} \right) = \frac{2}{L_y} \sum_{p=1}^{\infty} e^{\frac{(-\beta_p^2) \alpha (t-\tau)}{L_y^2}} \left( \frac{\beta_p^2 + B^2}{\beta_p^2 + B^2 + B} \right) \cos \left( \beta_p \frac{y}{L_y} \right) \quad (\text{EQ 4.4.11})$$

Where  $p$  is the summation variable;  $\beta_p \tan(\beta_p) = B$ , and  $B = \frac{hL_y}{K}$ .  $B$  is the Biot's modulus,  $K$  is the thermal conductivity of the sample and  $h$  is the heat transfer coefficient.

The eigen values  $\beta_p$  can be approximated as indicated below [191]

For  $0 \leq B \leq 2$  :

$$\beta_1 = \left\{ \frac{3B}{3+B} \left( 1 - \frac{1}{45} \left( \frac{3B}{3+B} \right)^2 \right) \right\}^{1/2} \quad (\text{EQ 4.4.12})$$

For  $p \geq 2$  and  $B \leq 2$

$$\beta_p = \frac{(p-1)\pi}{2(B+3)} \left\{ 2B+3 + 3 \left( 1 + \frac{4B(B+3)}{3(p-1)^2\pi^2} \right)^{1/2} \right\} \quad (\text{EQ 4.4.13})$$

Now, to present the final expression in organized fashion, the following variables and constants can be defined:

$$C_1 = \frac{x_2 - x_1}{L_x} \quad C_2 = \frac{z_2 - z_1}{L_z} \quad (\text{EQ 4.4.14})$$

$$S_{mx} = \cos\left(\frac{m\pi x}{L_x}\right) \left[ \sin\left(\frac{m\pi x_2}{L_x}\right) - \sin\left(\frac{m\pi x_1}{L_x}\right) \right] \quad (\text{EQ 4.4.15})$$

$$S_{nz} = \cos\left(\frac{n\pi z}{L_z}\right) \left[ \sin\left(\frac{n\pi z_2}{L_z}\right) - \sin\left(\frac{n\pi z_1}{L_z}\right) \right] \quad (\text{EQ 4.4.16})$$

$$S_{py} = \frac{\beta_p^2 + B^2}{\beta_p^2 + B^2 + B} \cos\left(\beta_p \frac{y}{L_y}\right) \quad (\text{EQ 4.4.17})$$

Using these variables/constants, and simplifying the expression for  $T(\cdot)$  can be written as

$$T(x, y, z, t) =$$

$$\begin{aligned} & \frac{\alpha}{K} q_0 \int_0^{(t-\Delta t)} \left[ C_1 C_2 + \frac{2}{\pi} C_2 \sum_{m=1}^{\infty} e^{-m^2 \pi^2 \alpha \frac{t-\tau}{L_x^2}} S_{mx} \frac{1}{m} + \frac{2}{\pi} C_1 \sum_{n=1}^{\infty} e^{-n^2 \pi^2 \alpha \frac{t-\tau}{L_z^2}} S_{nz} \frac{1}{n} \right] + \\ & \frac{4}{\pi^2} \left( \sum_{m=1}^{\infty} \sum_{n=1}^{\infty} \frac{1}{nm} e^{(-\pi^2 \alpha)(t-\tau) \left( \frac{m^2}{L_x^2} + \frac{n^2}{L_z^2} \right)} S_{mx} S_{nz} \right) \\ & \left[ \frac{2}{L_y} \sum_{p=1}^{\infty} e^{-\beta_p^2 \alpha \frac{(t-\tau)}{L_y^2}} S_{py} \right] d\tau \quad (\text{EQ 4.4.18}) \end{aligned}$$

#### 4.4.4 Solution of the model

There are four expressions summed up inside the integration, in the above expression (4.4.18) for  $T(\cdot)$ . All four expressions are solved and simplified for a computer solution as shown in the appendix A.

To solve the expression for  $T(\cdot)$ , a FORTRAN program was developed. The algorithm to solve  $T(\cdot)$  is given in the flow chart shown in figures 85 and 86. To solve the infinite summation over variables  $m, n$  and  $p$ , advantage was taken of decreasing value of  $\exp(-x)$ . The summation was done up to the lowest value of  $\exp(-20)$ , beyond which the contribution to  $T(\cdot)$  was negligible ( $10^{-10}$ ). As shown in the flow chart (figure 85), the treatment of expressions involving single, double and triple summation was done separately. Figure 86 shows the detailed steps for implementation of the summation of an infinite triple summation.

Temperature distribution in the whole specimen can be determined by the above model. The data for  $K$ ,  $C_p$ , and  $\rho$  can be changed either in the program or interactively. Figure 87 shows the temperature variation at two locations on the surface of the specimen, due to laser beam (at the center of plate (1"X1"X.25")) with increasing interaction time. The model shows fast increase in temperature with time (at small times) and eventually the attainment of a steady state for a longer interaction time. This typical behavior of heat transfer in a plate, due to a high energy source, establishes the authenticity of the this model. This model shows a new approach for formulating heat transfer problems associated with a high energy collimated source. Although the model presented in this section does not involve the laser traverse speed term, the information from this model can be used to simulate the laser traverse speed effect. For example, as shown in figure 87, the time to reach a specific temperature at two locations can be considered to be equivalent to the laser interaction time for a given traverse speed. The laser interaction time (laser spot radius/

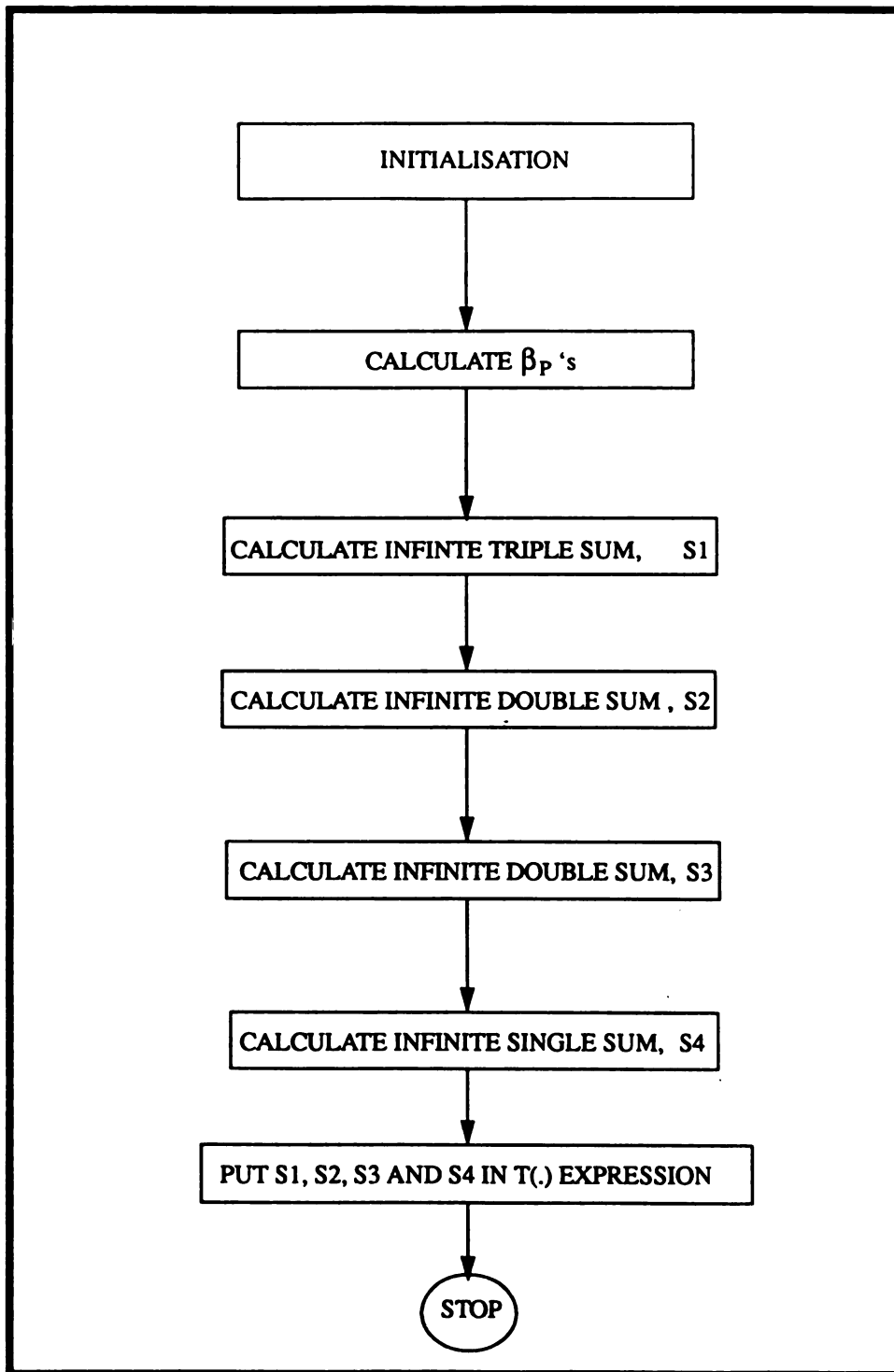
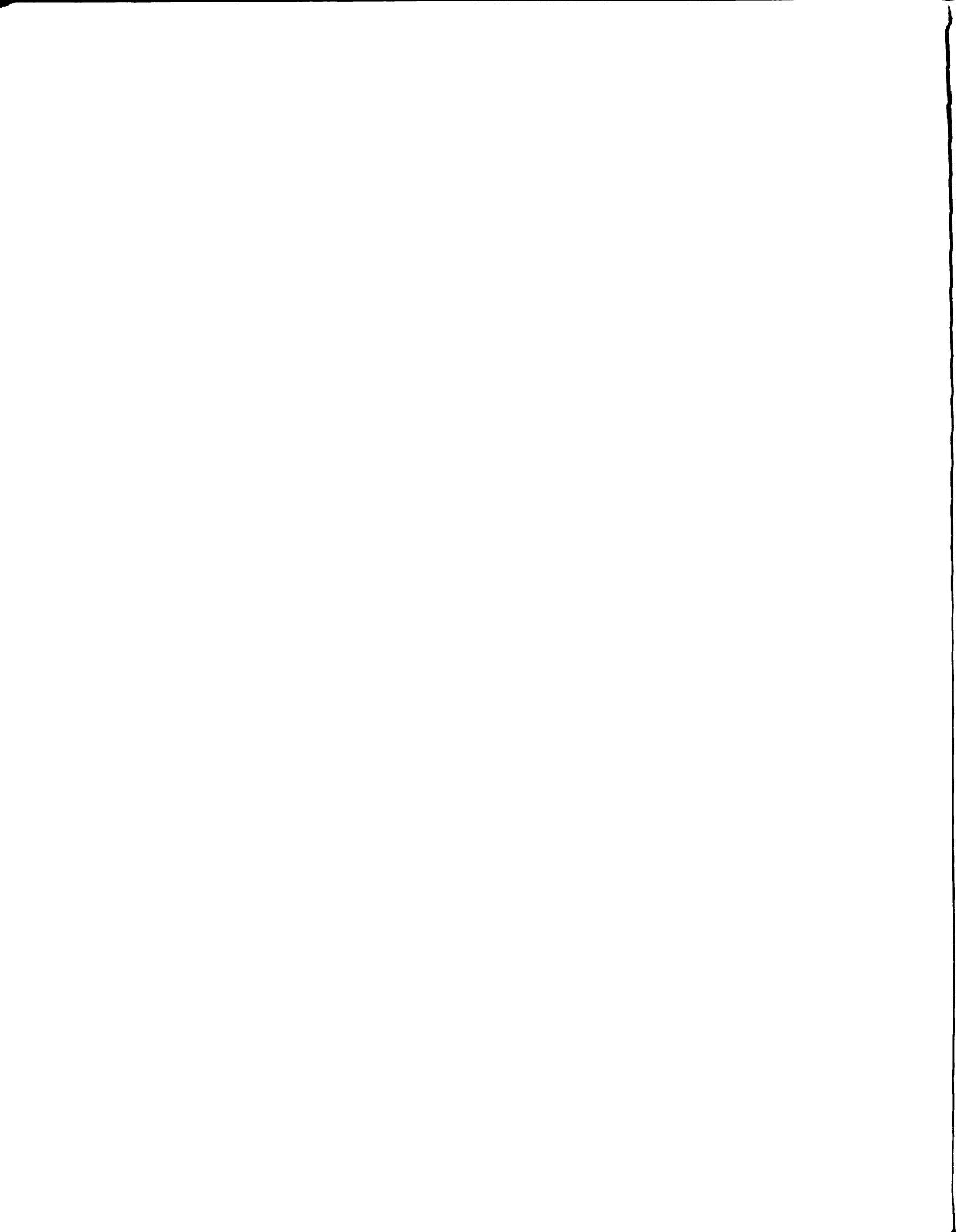


Figure 85. Main flow chart of computer program, developed to solve the analytical model



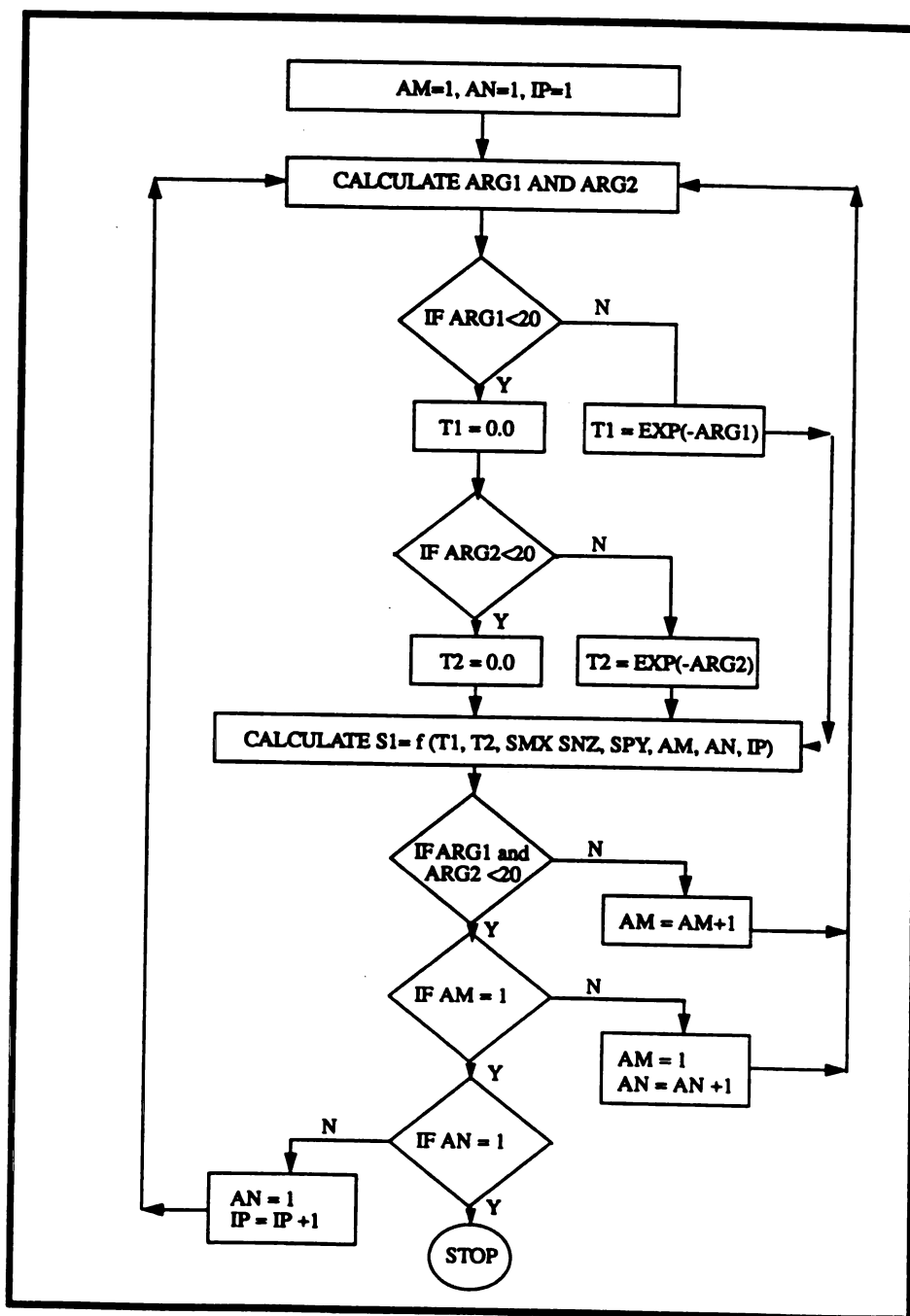


Figure 86. Detailed flow chart for the computation of triple summation of the model.

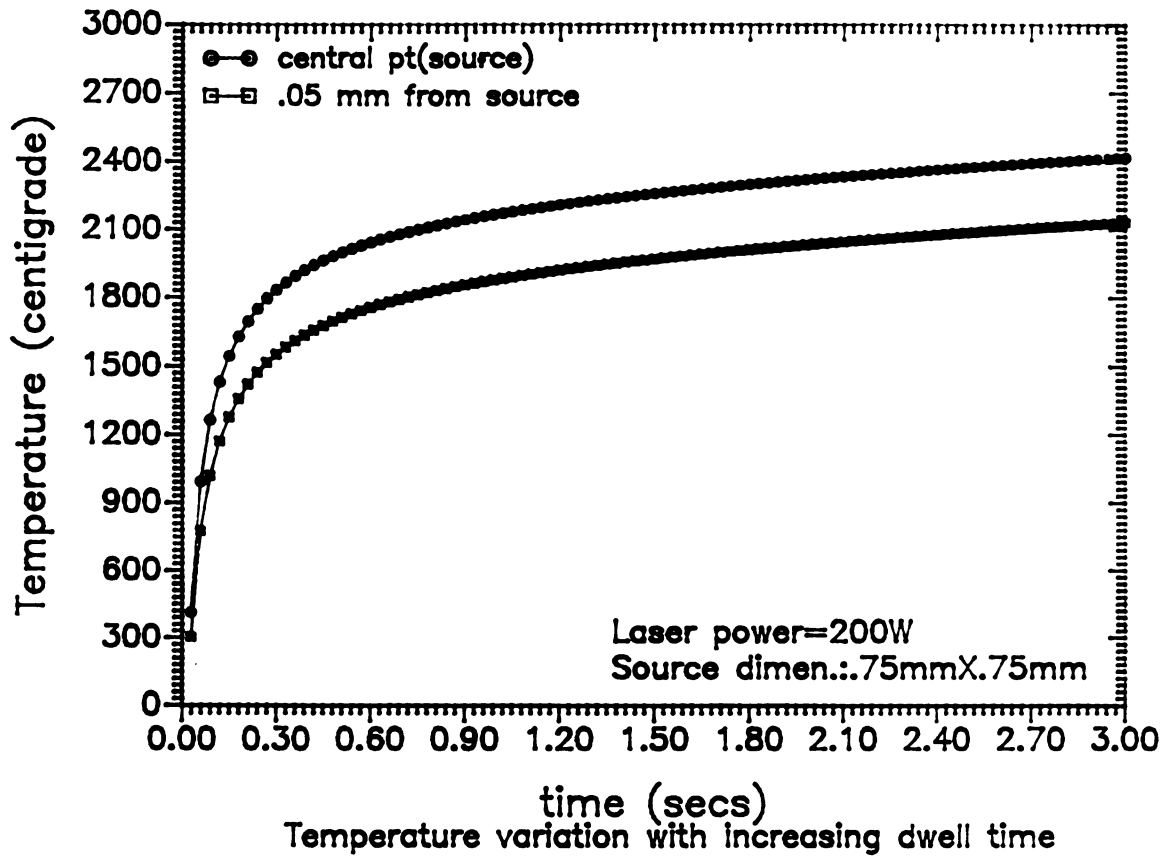


Figure 87. Diagram showing computed temperature variation with increasing laser dwell time on the sample.

speed), when input into the model, gives the maximum temperature at a specific location on the sample. Once the maximum temperature, at locations in the depth direction is predicted, it can be used for predicting the depth to which the austenization temperature can be reached at a given traverse speed (alternatively the laser dwell time). A series of plots, similar to figure 87, can be drawn for various points in the depth of laser irradiated zone until the temperature attained is above the austenization temperature. That depth (distance) of the last point will be the case depth during laser hardening. This is because the limiting factor for hardening in laser hardening is not as much the critical cooling rate, but the attainment of the austenization temperature.

Although the model assumes temperature independent properties, the results obtained compare well with the results obtained by a numerical solution considering the temperature dependent  $K$ ,  $C_p$  and  $\rho$ . Numerical solutions were obtained by using a commercial FEM package (ANSYS). Figure 88 shows the temperature distribution on the sample due to simulation of laser irradiation at the surface of the specimen under the same conditions considered in the analytical model solution (convective boundary at the bottom and adiabatic conditions at the sides). The temperature attained at the end of 0.1 second is about  $1005^{\circ}$  K. This compares well with the temperature shown in figure 87 at the end of 0.1 sec of laser dwell time. Some additional numerical solutions were obtained for temperature distribution on the surface of a specimen due to a moving laser beam. Figure 89 shows the temperature distribution on the specimen surface due to a moving laser beam with a velocity  $v$  (interaction time 0.1s). Figure 89, and 90 are the snap shots of the temperature distribution on the surface of sample at the end of 0.2 and 0.3 seconds respectively. This simulation of a moving laser beam by using the ANSYS program shows that the maximum temperature achieved at the surface is shifted towards the tail of the moving laser beam spot.

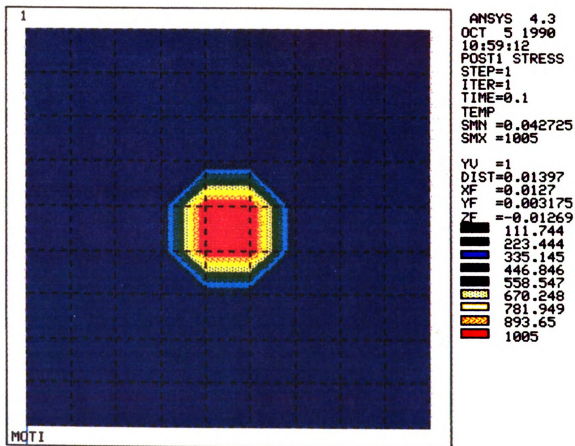


Figure 88. Temperature contour on AISI 1018 steel surface due to irradiation of stationary laser. Laser power 200 W and interaction time .1 sec.

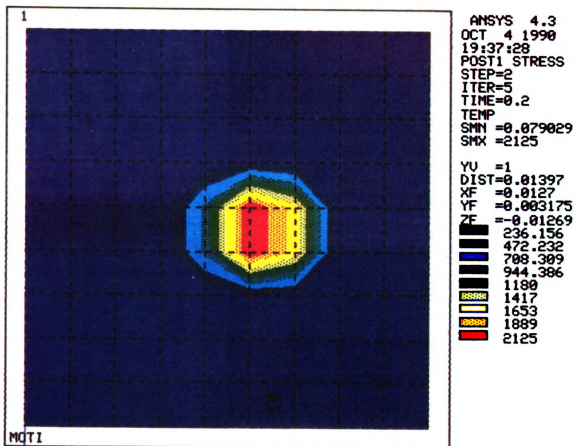


Figure 89. Temperature contour on AISI 1018 steel surface due to a moving laser. Laser power 200 W, interaction time of .1 sec., snap shot at time .2 sec.

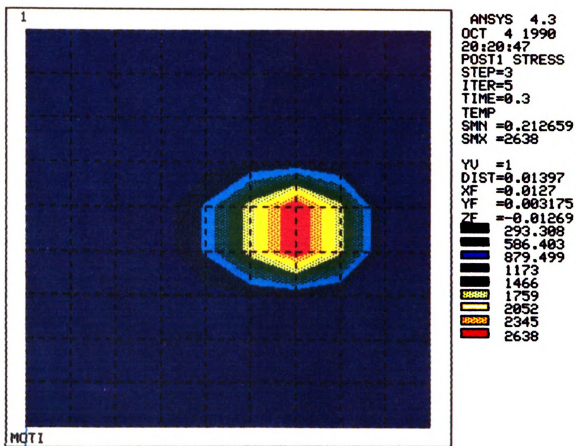


Figure 90. Temperature contour on AISI 1018 steel surface due to a moving laser. laser power 200 W, interaction time of .1 sec., snap shot at time .3 sec.

The analytical model, developed and solved in this thesis, can be modified to implement the velocity term. A modified model is shown in appendix (C). The solution of this model requires modification of the program, as shown in appendix (B), and requires numerical integration of the terms.

## V CONCLUSIONS

The present study of surface treatment of steel with Nd:Yag laser leads to the following conclusions:

- Increase in surface hardness of steel through microstructure control, or introduction of carbon or boron in the surface by use of a Nd:Yag laser has been established.
- High surface hardness of laser transformation hardened AISI 1045 steel is due to the fineness of the martensitic structure, attained by a relatively high self quenching rate.
- High surface hardness of laser carburized AISI 1018 steel is due to the formation of ledeburitic structure, which imparts surface hardness as high as ~1050 Hv.
- High surface hardness of laser borided AISI 1018 steel was due to the formation of FeB and Fe<sub>2</sub>B phases. Surface hardness achieved was in the range of 1300 to 2200 Hv.
- The morphology of microstructure, obtained during laser surface treatments, involving melting, is a strong function of laser processing parameters, which in turn control the G/R ratio.
- Defects such as porosity and cracks are produced during laser carburizing and boriding. Two types of cracks have been observed during laser carburizing of AISI 1018 steel: straight and wiggly cracks.
- The best microstructure (with respect to crack free and high hardness) which can form, during laser carburizing of AISI 1018 steel, is a mixture of austenite dendrites and interdendritic eutectic.
- The best microstructure which can form, during laser boriding of AISI 1018 steel, is the single phase Fe<sub>2</sub>B. It imparts ideal properties to the borided layer: high hardness (1200-1600 Hv) and a favorable state of compressive stress.

- One important aspect of laser surface modification studies is to understand the heat transfer, during the process, which controls the microstructure evolution. Therefore, a simple analytical heat transfer model, using Green's function, has been developed to predict the temperature distribution on a workpiece during laser surface treatments.
- The above model can be used to predict the case depth during laser hardening, and it has been modified to implement the laser traverse speed.

## Appendix A

### A Complete solution of the model developed in section 4.4

Four expressions, in the integral, are expanded individually as follows

(a) Expression under single summation is

$$\int_0^{(t-\Delta t)} \left( C_1 C_2 \frac{2}{L_y} \sum_{p=1}^{\infty} e^{-\beta_p^2 \alpha \frac{(t-\tau)}{L_y^2}} S_{py} \right) d\tau \quad (\text{A.1})$$

$$C_1 C_2 \frac{2}{L_y} \left( \sum_{p=1}^{\infty} e^{\frac{-\alpha \beta_p^2 t}{L_y^2}} \right) \int_0^{(t-\Delta t)} e^{\beta_p^2 \alpha \frac{\tau}{L_y^2}} S_{py} d\tau \quad (\text{A.2})$$

$$\frac{2C_1 C_2}{L_y} \left( \sum_{p=1}^{\infty} e^{\frac{-\alpha \beta_p^2 t}{L_y^2}} \right) \left( \frac{L_y^2}{\beta_p^2 \alpha} S_{py} e^{\beta_p^2 \alpha \frac{\tau}{L_y^2}} \right) \Bigg|_0^{t-\Delta t} \quad (\text{A.3})$$

$$\frac{2C_1 C_2}{L_y} \frac{L_y^2}{\beta_p^2 \alpha} \sum_{p=1}^{\infty} e^{\frac{-\alpha \beta_p^2 t}{L_y^2}} S_{py} \left[ e^{\frac{\beta_p^2 \alpha (t-\Delta t)}{L_y^2}} - 1 \right] \quad (\text{A.4})$$

$$2 \left( \frac{C_1 C_2 L_y}{\alpha} \right) \sum_{p=1}^{\infty} \frac{S_{py}}{\beta_p^2} \left[ e^{\frac{-\beta_p^2 \alpha \Delta t}{L_y^2}} - e^{\frac{-\beta_p^2 \alpha t}{L_y^2}} \right] \quad (\text{A.5})$$

(b) One of the expressions, involving double summation is

$$\int_0^{(t-\Delta t)} C_2 \frac{4}{\pi L_y} \sum_{m=1}^{\infty} \sum_{p=1}^{\infty} \frac{S_{mx} S_{py}}{m} \exp \left( - \left( \frac{m^2 \pi^2 \alpha}{L_x^2} + \frac{\beta_p^2 \alpha}{L_y^2} \right) (t-\tau) \right) \delta \tau \quad (\text{A.6})$$

Assigning,

$$A_{mp} = \frac{m^2 \pi^2 \alpha}{L_x^2} + \frac{\beta_p^2 \alpha}{L_y^2} \quad (\text{A. 7})$$

equation (A.6) can be written as

$$\int_0^{(t-\Delta t)} C_2 \frac{4}{\pi L_y} \sum_{m=1}^{\infty} \sum_{p=1}^{\infty} \frac{S_{mx} S_{py}}{m} e^{-A_{mp}(t-\tau)} \delta \tau \quad (\text{A. 8})$$

$$C_2 \frac{4}{\pi L_y} \sum_{m=1}^{\infty} \sum_{p=1}^{\infty} \frac{S_{mx} S_{py}}{m} e^{-A_{mp}t} \int_0^{(t-\Delta t)} e^{A_{mp}\tau} d\tau \quad (\text{A. 9})$$

$$C_2 \frac{4}{\pi L_y} \sum_{m=1}^{\infty} \sum_{p=1}^{\infty} \frac{S_{mx} S_{py}}{m} e^{-A_{mp}t} \frac{1}{A_{mp}} (e^{A_{mp}(t-\Delta t)} - 1) \quad (\text{A. 10})$$

$$C_2 \frac{4}{\pi L_y} \sum_{m=1}^{\infty} \sum_{p=1}^{\infty} \frac{S_{mx} S_{py}}{m} \frac{1}{A_{mp}} (e^{-A_{mp}\Delta t} - e^{-A_{mp}t}) \quad (\text{A. 11})$$

(c) Second expression, involving double summation can be written similar to the expression (A.11), just by substituting n for m and z for x. Final form is given by

$$C_2 \frac{4}{\pi L_y} \sum_{n=1}^{\infty} \sum_{p=1}^{\infty} \frac{S_{nz} S_{py}}{n} \frac{1}{A_{np}} (e^{A_{np}\Delta t} - e^{-A_{np}t}) \quad (\text{A. 12})$$

(d) Expression, involving tripple summation is

$$\int_0^{(t-\Delta t)} \frac{8}{\pi^2 L_y} \sum_{m=1}^{\infty} \sum_{n=1}^{\infty} \sum_{p=1}^{\infty} \frac{S_{mx} S_{nz} S_{py}}{mn} \exp(-A_{mnp}(t-\Delta t)) \delta \tau \quad (\text{A. 13})$$

Where

$$A_{mnp} = \frac{m^2 \pi^2 \alpha}{L_x^2} + \frac{n^2 \pi^2 \alpha}{L_z^2} + \frac{\beta_p^2 \alpha}{L_y^2} \quad (\text{A. 14})$$

The main expression (A.13) can be written as

$$\frac{8}{\pi^2 L_y} \sum_{m=1}^{\infty} \sum_{n=1}^{\infty} \sum_{p=1}^{\infty} \frac{S_{mx} S_{nz} S_{py}}{mn} e^{(-A_{mnp})t} \int_0^{(t-\Delta t)} e^{A_{mnp}\tau} \delta\tau \quad (\text{A. 15})$$

$$\frac{8}{\pi^2 L_y} \sum_{m=1}^{\infty} \sum_{n=1}^{\infty} \sum_{p=1}^{\infty} \frac{S_{mx} S_{nz} S_{py}}{mn} e^{(-A_{mnp})t} \frac{1}{A_{mnp}} e^{A_{mnp}\tau} \Big|_0^{t-\Delta t} \quad (\text{A. 16})$$

$$\frac{8}{\pi^2 L_y} \sum_{m=1}^{\infty} \sum_{n=1}^{\infty} \sum_{p=1}^{\infty} \frac{S_{mx} S_{nz} S_{py}}{mn A_{mnp}} (e^{(-A_{mnp})\Delta t} - e^{(-A_{mnp})t}) \quad (\text{A. 17})$$

## Appendix B

### A computer program to solve the model in section 4.4.

(Program listing)

```
C
C
C   This program predict transient temperature distribution
C   on a plate, due to a stationary laser source. It accepts
C   thermal properties, such as thermal conductivity, density
C   and diffusivity of the material. In addition, it also expects
C   the dimensions of laser (assumed square)
C
C   SUM1 : TRIPLE SUMMATION IN APPENDIX A
C   SUM2: SINGLE SUMMATION IN APPENDIX A
C   SUM3: FIRST DOUBLE SUMMATION (M, P)
C   SUM4: SECOND DOUBLE SUMMATION (N, P)
C
PROGRAM STAT3D
C
C*DEFINITION OF VARIABLES
C
DOUBLE PRECISION BETA(300),ARG1,ARG2,SMX,SPY,SNZ,PI
DOUBLE PRECISION SUM1,SUM2,SUM3,SUM4,AMNP
DOUBLE PRECISION TERM1,TERM2,EXP1,EXP2,ALPHA
REAL ALX,ALY,ALZ,X,Y,Z,X1,X2,Z1,Z2,AK,H,B,CON,DT,TIME
INTEGER AM,AN,IP,I
REAL P1,P2,P3,VAL,Q0
```

C

C \*DEFINITION OF FUNCTIONS

C

$$SMX(AM)=\cos(AM*\pi*X/ALX)*(\sin(AM*\pi*X2/ALX)-\sin(AM*\pi*X1/ALX))$$

$$SNZ(AN)=\cos(AN*\pi*Z/ALZ)*(\sin(AN*\pi*Z2/ALZ)-\sin(AN*\pi*Z1/ALZ))$$

$$SPY(IP)=(\beta(IP)^2+B*B)*\cos(\beta(IP)*Y/ALY)/(\beta(IP)^2+B*B+B)$$

$$AMNP(P1,P2,P3)=\alpha*((AM*\pi*P1/ALX)^2+(AN*\pi*P2/ALZ)$$

$$+^2+(\beta(IP)*P3/ALY)^2)$$

C \*\*

OPEN(UNIT=60,FILE='becc3.res',STATUS='NEW')

PI=4.0\*ATAN(1.0)

ALPHA=.00001675

C PRINT \*, 'LX,LY,LZ'

C READ(\*,\*) ALX,ALY,ALZ

C PRINT \*, 'X,Y,Z'

C READ(\*,\*)X,Y,Z

C PRINT \*, 'X1,X2,Z1,Z2'

C READ(\*,\*)X1,X2,Z1,Z2

C PRINT \*, 'TIME AND DELTA TIME'

C READ \*, TIME,DT

C

C \*INITIALIZATION

C

ALX=.0254

Q0=200

ALY=.00634

ALZ=.0254

```
X=.01270
Y=-.001
Z=.01270
X1=.01195
X2=.01345
Z1=.01195
Z2=.01345
WRITE(60,*)X,Y,Z
WRITE(60,*)ALPHA,Q0
C 2 CONTINUE
Y=Y+.001
DO 5 I=3,300,3
TIME=I*.01
DT=.02
AM=1
AN=1
IP=1
C1=(X2-X1)/ALX
C2=(Z2-Z1)/ALZ
SUM1=0.0
SUM2=0.0
SUM3=0.0
SUM4=0.0
AK=64.0
H=300.0
B=H*ALY/AK
C
```

## C \* CALCULATION OF BETAS

C

CON=3.0\*B/(3.0+B)

BETA(1)=SQRT(CON\*(1-CON\*CON/45.0))

DO 10 IP=2,250

BETA(IP)=(IP-1)\*PI/(2.0\*(B+3.0))

$$\text{BETA(IP)} = \text{BETA(IP)} * (2.0 * \text{B} + 3.0 + 3.0 * \text{SQRT}(1 + (4 * \text{B} * (\text{B} + 3.0) / \\ + (3 * (\text{IP} - 1) * (\text{IP} - 1) * \text{PI} * \text{PI}))))$$

10 CONTINUE

C \*\*

C \*\*

IP=1

PRINT \*, 'ENTERING THE TRIPLE'

20 CONTINUE

ARG1=AMNP(1.0,1.0,1.0)\*DT

ARG2=AMNP(1.0,1.0,1.0)\*TIME

IF(ARG1 .LT. 20.0) THEN

EXP1=EXP(-ARG1)

ELSE EXP1=0.0

END IF

IF(ARG2 .LT. 20.0) THEN

EXP2=EXP(-ARG2)

ELSE EXP2=0.0

END IF

C \*\*

TERM1= EXP1-EXP2

TERM2= SMX(AM)\*SNZ(AN)\*SPY(IP)/(AM\*AN\*AMNP(1.0,1.0,1.0))

```
SUM1=SUM1+8.0*TERM1*TERM2/(PI*PI*ALY)
C **
IF (.NOT.((ARG1 .GT. 20.0).AND.(ARG2 .GT. 20.0))) THEN
AM=AM+1
GOTO 20
ELSE IF ((AM.EQ.1).AND.(AN.NE.1)) THEN
AN=1
IP=IP+1
GOTO 20
ELSE IF ((AM.EQ.1).AND.(AN.EQ.1)) THEN
GOTO 25
ELSE
AM=1
AN=AN+1
GOTO 20
END IF
C **
25 CONTINUE
PRINT *, 'OUT OF FIRST TRIPLE'
PRINT *,SUM1
C * SINGLE SUMMATION COMPUTATION STARTS
IP=1
30 CONTINUE
ARG1=AMNP(0.0,0.0,1.0)*DT
ARG2=AMNP(0.0,0.0,1.0)*TIME
IF(ARG1 .LT. 20.0) THEN
EXP1=EXP(-ARG1)
```

```
ELSE
EXP1=0.0
END IF
IF(ARG2 .LT. 20.0) THEN
EXP2=EXP(-ARG2)
ELSE
EXP2=0.0
END IF
C *
TERM1=EXP1-EXP2
TERM2=SPY(IP)/AMNP(0.0,0.0,1.0)
SUM2=SUM2+2.0*TERM1*TERM2*C1*C2/ALY
C **
IF(.NOT.((ARG1.GT.20.0).AND.(ARG2.GT.20.0))) THEN
IP=IP+1
GOTO 30
END IF
PRINT *, 'OUT OF SINGLE SUM'
PRINT *, SUM2
C **
C * FIRST DOUBLE SUMMATION (M,P) STARTS
AM=1
IP=1
40 CONTINUE
ARG1=AMNP(1.0,0.0,1.0)*DT
ARG2=AMNP(1.0,0.0,1.0)*TIME
IF(ARG1 .LT. 20.0) THEN
```

```
EXP1=EXP(-ARG1)
ELSE EXP1=0.0
END IF
IF(ARG2 .LT. 20.0) THEN
EXP2=EXP(-ARG2)
ELSE EXP2=0.0
END IF
C **

TERM1= EXP1-EXP2
TERM2= SMX(AM)*SPY(IP)/(AM*AMNP(1.0,0.0,1.0))
SUM3=SUM3+4.0*C1*TERM1*TERM2/(PI*ALY)
C **

IF (.NOT.((ARG1.GT.20.0).AND.(ARG2.GT.20.0))) THEN
AM=AM+1
GOTO 40
ELSE IF (AM .NE. 1) THEN
AM=1
IP=IP+1
GOTO 40
END IF
PRINT *, 'OUT OF FIRST DOUBLE SUMMATION'
PRINT *, SUM3
C **
C SECOND DOUBLE SUMMATION STARTS
AN=1
IP=1
50 CONTINUE
```

```

ARG1=AMNP(0.0,1.0,1.0)*DT
ARG2=AMNP(0.0,1.0,1.0)*TIME
IF(ARG1 .LT. 20.0) THEN
EXP1=EXP(-ARG1)
ELSE EXP1=0.0
END IF
IF(ARG2 .LT. 20.0) THEN
EXP2=EXP(-ARG2)
ELSE EXP2=0.0
end iF
C **
TERM1= EXP1-EXP2
TERM2= SNZ(AN)*SPY(IP)/(AN*AMNP(0.0,1.0,1.0))
SUM4=SUM4+4.0*C2*TERM1*TERM2/(PI*ALY)
C **
IF (.NOT.((ARG1.GT.20.0).AND.(ARG2.GT.20.0))) THEN
AN=AN+1
GOTO 50
ELSE IF (AN .NE. 1) THEN
AN=1
IP=IP+1
GOTO 50
END IF
PRINT *, "OUT OF SECOND DOUBLE SUMMATION"
PRINT *, SUM4
C **
C

```

C\*FINAL EXPRESSION FOR T(.)

C

VAL=(Q0\*ALPHA/(AK\*.00075\*.00075\*PI))\*(SUM1+SUM2+SUM3+SUM4)

WRITE(60,\*)TIME,VAL

PRINT \*,VAL

5 CONTINUE

CLOSE(60)

END

## Appendix C

### Development of heat transfer model for a moving laser source

#### Physical definition of problem

A square region on a plate is heated by a moving laser beam. The square source has dimensions '2a' on each side. Due to the small dimensions of the laser spot, the plate can be considered to be infinite in the plane of the heated surface. The thickness is finite and is called L. The geometry is as shown in figure (91). Heat is assumed to be only over the surface (at y=0), where the laser impinges. Elsewhere, the surface is assumed to be insulated. On the lower surface (y=L), a convective boundary condition has been assumed.

The temperature distribution is found assuming temperature independent thermal properties, no radiant heat transfer and no melting are assumed. These assumptions linearize the problem so that an analytical solution is possible. As before (section 4.4) Green's function is used in the solution.

#### Mathematical description of the problem

If the problem is solved for the moving plate and a coordinate system attached to the center of the laser beam, the governing partial differential equation is :

$$\alpha \left( \frac{\delta^2 T}{\delta x^2} + \frac{\delta^2 T}{\delta y^2} + \frac{\delta^2 T}{\delta z^2} \right) = \frac{\delta T}{\delta t} + v \frac{\delta T}{\delta z} \quad (\text{C. 1})$$

The boundary conditions, as shown in figure (91) are

$$T \rightarrow 0 \quad \text{at} \quad x \rightarrow \infty$$

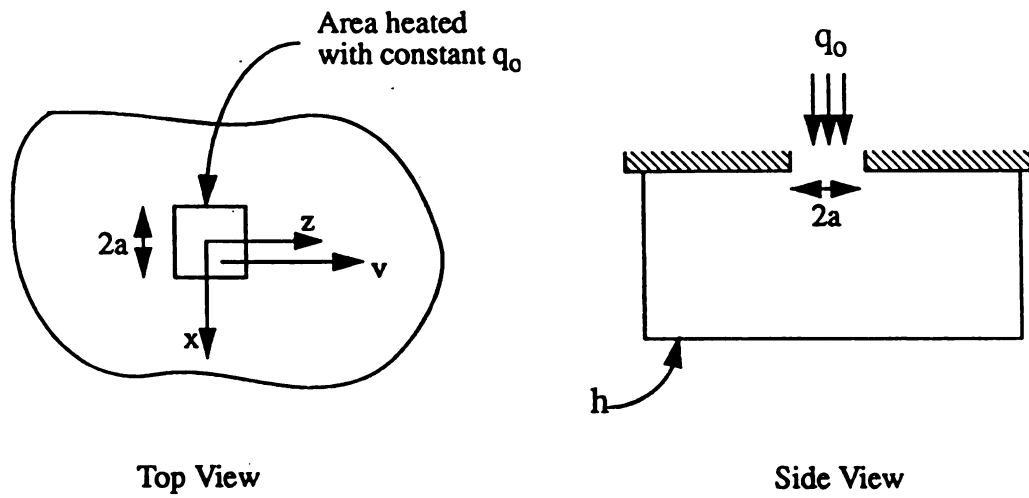


**Figure 91. Schematic diagram illustrating the various dimensions, coordinates and boundary conditions for the laser surface processing heat transfer model in appendix C.**

$T \rightarrow 0$  at  $z \rightarrow \infty$

At  $y = 0$

$$-K \frac{\delta T}{\delta y} = \begin{cases} q_0 & \text{for } -a < x < a \text{ and } -a < z < a \\ 0 & \text{otherwise} \end{cases} \quad (\text{C. 2})$$

At  $y = L$ ,

$$-K \frac{\delta T}{\delta y} = h(T - T_\infty) \quad (\text{C. 3})$$

The initial condition is  $T(x, y, z, 0) = 0$

This is the complete mathematical definition of the problem. The objective is to find an expression for  $T(\cdot)$ , for known values of heat input  $q_0$ , thermal conductivity  $K$ , thermal diffusivity  $\alpha$  and relevant dimensions.

### Derivation of the model

The problem can be put into a more manageable form by using a transformation [193] as follows:

$$T(x, y, z, t) = W(x, y, z, t) \exp\left[\frac{vz}{2\alpha} - \frac{v^2 t}{4\alpha}\right] \quad (\text{C. 4})$$

This reduces the main equation to::

$$\alpha \left( \frac{\delta^2 W}{\delta x^2} + \frac{\delta^2 W}{\delta y^2} + \frac{\delta^2 W}{\delta z^2} \right) = \frac{\delta W}{\delta t} \quad (\text{C. 5})$$

Without a loss of generality  $T_\infty$  can be set equal to zero and  $T(\cdot)$  interpreted as the temper-

ature raise above T. Then the boundary conditions become:

$$W \rightarrow 0 \quad \text{at } x \rightarrow \infty$$

$$W \rightarrow 0 \quad \text{at } z \rightarrow \infty$$

At  $y = 0$ ,

$$-K \frac{\delta W}{\delta y} = \begin{cases} q_0 \left[ -\frac{vz}{2\alpha} + \frac{v^2 t}{4\alpha} \right] & \text{for } -a < x < a \quad \text{and} \quad -a < z < a \\ 0 & \text{otherwise} \end{cases} \quad (\text{C.6})$$

At  $y = L$ ,

$$-K \frac{\delta W}{\delta y} = hW \quad (\text{C.7})$$

and initial condition is  $W(x, y, z, 0) = 0$

The solution can be obtained by using Green's function. The problem is described by  $X00Y23Z00Vz$ , denoting a constant velocity in the z-direction. The needed Green's function is  $G_{X00Y23Z00}(x, y, z, t/x', y', z', t)$ , which can be related to an 1-D Green's function by the product:

$$G_{X00Y23Z00} \left( \frac{x, y, z, t}{x', y', z', \tau} \right) = G_{X00} \left( \frac{x, t}{x', \tau} \right) G_{Y23} \left( \frac{y, t}{y', \tau} \right) G_{Z00} \left( \frac{z, t}{z', \tau} \right) \quad (\text{C.8})$$

Using a method similar to that shown in section 4.4, the solution of  $W(\cdot)$  is given by

$$W(x, y, z, t) = \frac{\alpha}{K} \int_{-a}^a \int_{-a}^a \int_0^t q_0 \exp \left[ -\frac{vz'}{2\alpha} + \frac{v^2 \tau}{4\alpha} \right] (G_{X00} \left( \frac{x, t}{x', \tau} \right) G_{Y23} \left( \frac{y, t}{y', \tau} \right) G_{Z00} \left( \frac{z, t}{z', \tau} \right)) dx' dz' d\tau \quad (\text{C.9})$$

The integrals on  $x'$  and  $z'$  can be performed first, using equations for  $G_{X00}(\cdot)$  and  $G_{Z00}(\cdot)$ :

$$\int_{-a}^a G_{x00} \left( \frac{x, t}{x, \tau} \right) dx' = \frac{1}{2} \left[ \operatorname{erfc} \left( \frac{x-a}{(4\alpha(t-\tau))^{1/2}} \right) - \operatorname{erfc} \left( \frac{x+a}{(4\alpha(t-\tau))^{1/2}} \right) \right] \quad (\text{C. 10})$$

In case of the integral involving  $z'$ , an additional term  $vz'/2a$  has to be considered:

$$\int_{-a}^a G_{z00} \left( \frac{z, t}{z', \tau} \right) \exp \left( \frac{vz'}{2\alpha} \right) dz' = \int_{-a}^a \frac{1}{(4\alpha(t-\tau))^{1/2}} \exp \left[ -\frac{(z-z')^2}{4\alpha(t-\tau)} - \frac{vz'}{2\alpha} \right] dz' \\ \frac{1}{2} e^{\left[ \frac{v^2(t-\tau)}{4\alpha} - \frac{vz}{2\alpha} \right]} \left\{ \operatorname{erfc} \left[ \frac{z-a}{(4\alpha(t-\tau))^{1/2}} - v \left( \frac{t-\tau}{4\alpha} \right)^{1/2} \right] - \operatorname{erfc} \left[ \frac{z+a}{(4\alpha(t-\tau))^{1/2}} - v \left( \frac{t-\tau}{4\alpha} \right)^{1/2} \right] \right\} \quad (\text{C. 11})$$

The  $G_{y23}(\cdot)$  is handled in the same way as is handled in section 4.4

The solution for  $T(\cdot)$  is given by using the above equations (C.4, C.10 and C.11), involving  $G_{x00}(\cdot)$ ,  $G_{y23}(\cdot)$  and  $G_{z00}(\cdot)$  and  $T = f(W, v, z, t, a)$

We get,

$$T(x, y, z, t) = \\ \frac{1}{4} \frac{\alpha}{K} q_0 \int_0^t \left[ \operatorname{erfc} \left( \frac{x-a}{(4\alpha(t-\tau))^{1/2}} \right) - \operatorname{erfc} \left( \frac{x+a}{(4\alpha(t-\tau))^{1/2}} \right) \right] \left( \frac{2}{L_y} \sum_{p=1}^{\infty} e^{-\frac{(-\beta_p^2)\alpha(t-\tau)}{L_y^2}} \left( \frac{\beta_p^2 + B^2}{\beta_p^2 + B^2 + B} \right) \cos \left( \beta_p \frac{y}{L_y} \right) \right) \\ \left\{ \operatorname{erfc} \left[ \frac{z-a}{(4\alpha(t-\tau))^{1/2}} - v \left( \frac{t-\tau}{4\alpha} \right)^{1/2} \right] - \operatorname{erfc} \left[ \frac{z+a}{(4\alpha(t-\tau))^{1/2}} - v \left( \frac{t-\tau}{4\alpha} \right)^{1/2} \right] \right\} \delta\tau \quad (\text{C. 12})$$

## REFERENCES

1. F. D. Seaman and D. S. Gnanamuthu, *Met. Prog.*, 8, (1975), p. 67.
2. C. Wick, *Manufacturing Engineering*, 6, (1976), p. 36.
3. W. M. Steen and C. Courtney, *Met. Techn.*, 10, (1979), p. 456.
4. S. A. Towers, *Manufacturing Engineering*, 8, (1984), p. 145.
5. M. F. Ashby and K. E. Esterling, *Acta Metall.*, 32(1), (1984), p. 1935.
6. Y. Arata, 'Plasma, Electron and Laser Beam Technology: Development and use in Materials Processing', ASM, (1986), p. 658.
7. V. G. Gregson, in 'Laser Materials Processing', ed.: M. Bass, North-Holland Publishing Co. New York, (1983), p. 201.
8. P. G. Moore and L. S. Weinman, in 'Source Book on Applications of the Laser in Metal Working', ed.: E. A. Metzbower, ASM, (1981), p. 318.
9. G. C. Irons, in 'Source Book on Applications of the Laser in Metal Working', ed.: E. A. Metzbower, ASM, (1981), p. 359.
10. J. E. Miller and J. A. Wineman, *Met. Prog.*, 5, (1977), p. 23.
11. H. Kawasumi, *Technocrate*, 6, (1978), p. 180.
12. O. Sandven, Metal Handbook, Ninth edition, vol. 4, (1990), p. 507.
13. W.W. Duley, CO<sub>2</sub> Lasers: Effects and Applications, Academic Press, New York, (1976), p. 53.
14. J. F. Eloy, Power Laser, Ellis Horwood Limited, Chichester, USA, (1990), p.19
15. M. J. Weber, Handbook of Laser Science and Technology, CRC press, Boca Raton, FL, (1982), vol. 1, p. 552.
16. J. F. Ready, Industrial Applications of Lasers, Academic Press, New York, (1978), p.88.
17. J. F. Harry, Industrial Lasers and Their Applications, Mcgraw Hill, London, England, (1974), p.82.

18. J. F. Ready, Industrial Applications of Lasers, Academic Press, New York, (1978), p.83.
19. W.W. Duley, CO<sub>2</sub> Lasers: Effects and Applications, Academic Press, New York, (1976, p. 15.
20. J. F. Ready, Industrial Applications of Lasers, Academic Press, New York, (1978), p. 84.
21. J. F. Ready, Industrial Applications of Lasers, Academic Press, New York, (1978), p. 85.
22. J. F. Eloy, Power Laser, Ellis Horwood Limited, Chichester, USA, (1990), p. 31
23. J. F. Ready, Industrial Applications of Lasers, Academic Press, New York, (1978), p. 94.
24. J. F. Harry, Industrial Lasers and Their Applications, Mcgraw Hill, London, England, (1974), p.86.
25. J. F. Ready, Industrial Applications of Lasers, Academic Press, New York, (1978), p. 101.
26. J. F. Ready, Industrial Applications of Lasers, Academic Press, New York, (1978), p. 106.
27. E. V. Locks and R. A. Hella, IEEE, J. Quantum Electronics, vol. QE-10, No. 2, (1974), p. 179.
28. C. Courtney and W. M. Steen, Paper No. 2 in Proc. intl. Conf. on Advances in Surface Coating Technology, British Welding Institute, England, 91978), p. 24.
29. J. F. Eloy, Power Laser, Ellis Horwood Limited, Chichester, USA, (1990),p. 24
30. F. J. McClung and R. W. Hellworth, "Characteristics of Giant Optical Pulsations from Ruby", Proceedings of IEEE, (1963), p.46.
31. J. F. Eloy, Power Laser, Ellis Horwood Limited, Chichester, USA, p. 26
32. J. F. Ready, Industrial Applications of Lasers, Academic Press, New York, (1978), p. 224.
33. J. Mazumder, J. Met., 5, (1983), p. 18.
34. C. Courtney and W. M. Steen, Appl. Phys., 17, (3), 1978, p. 303.

35. A. F. Gibson, M. H. Kimmit and A. C. Walker, *Appl. Phys. Lett.*, 17 (1970), p.75.
36. J. Mazumder, in 'Laser Materials Processing', ed.: M. Bass, North-Holland Publishing Co. New York, (1983), p. 124.
37. Y. Arata and I. Miyamoto, *Laser Focus*, No. 3, (1977), p. 43.
38. M. A. Bramson, Infra-red Radiation: A Handbook for Applications, Plenum Press, New York, (1968), p. 197.
39. Hans Koebner, Industrial Applications of Lasers, Wiley Inter Science Publications, John-Wiley Sons, New York, (1984), p.78.
40. Hans Koebner, Industrial Applications of Lasers, Wiley Inter Science Publications, John-Wiley Sons, New York, (1984), p.83.
41. Y. Arata, "Basic Characteristics of Laser Output High Energy Density Heat Source", Paper No. 2 in Proc. Int. US/Japan int. Laser processing Conf. , LIA, Toledo, OH, (1981).
42. D. N. H. Trafford, T. Bell, J. H. P. C. Megaw and A. S. Brandon, in 'Heat Treatment' 79, The Metal Society, London, (1979), p. 33.
43. W. W. Duley, CO<sub>2</sub> Lasers: Effects and Applications, Academic Press, New York, (1976), p. 241.
44. J. Mazumder, in 'Laser Materials Processing', ed.: M. Bass, North-Holland Publishing Co. New York, (1983), p. 117.
45. T. R. Anthony and E. Cline, *J. Appl. Phys.*, 48, (1977), p.388.
46. J. Mazumder and W. M. Steen, *J. Appl. Phys.*, 51, (1988), p.941.
47. F. D. Seaman, "The Role of Shielding Gas in High Power CO<sub>2</sub> Laser Welding", SME Technical Paper No. MR77-982, Society of Manufacturing Engineers, Dearborn, MI.
48. R. C. Crafer and P. J. Oakley, in 'Applied Laser Tooling', eds: O. D. D. Soares and M. Derez-Amor, Martinus Nijhoff Publishers, Dordrecht, (1987), p. 79.
49. W. M. Steen, in 'Applied Laser Tooling', eds: O. D. D. Soares and M. Derez-Amor, Martinus Nijhoff Publishers, Dordrecht, (1987), p. 132.

50. M. F. Ashby, K. B. Easterling and W. B. Li, in 'Laser Processing of Materials', eds: K. Mukherjee and J. Mazumder, Conf. Proc. of AIME, held at Los Angeles on Feb. 26-31, (1984), p. 225.
51. S. L. Ream, in 'Surface Engineering', eds: R. Kossowski and S. Singhal, NATO ASI Series E, Applied Science-No. 85, Martinus Nijhoff Publisher, Dordrecht, (1989), p. 285.
52. I. Hawks, A. Walker, W. M. Steen and D. R. F. West, in 'Laser Processing of Materials', eds: K. Mukherjee and J. Mazumder, Conf. Proc. of AIME, held at Los Angeles on Feb. 26-31, (1984), p. 169.
53. C. H. Chen, M. K. Keshavan, C. J. Altstetter and J. M. Rigsbee, in 'Laser Processing of Materials', eds: K. Mukherjee and J. Mazumder, Conf. Proc. of AIME, held at Los Angeles on Feb. 26-31, (1984), p. 183.
54. J. Mazumder, C. Cusand, A. Ghosh and C. Eiholzer, in 'Laser Processing of Materials', eds: K. Mukherjee and J. Mazumder, Conf. Proc. of AIME, held at Los Angeles on Feb. 26-31, (1984), p. 199.
55. E. M. Breinan and B. H. Kear, in 'Laser Materials Processing', ed: M. Bass, North-Holland Publishing Co. New York, (1983), p. 238.
56. H. W. Bergmann and H. V. Fritsch, in 'Rapidly Solidified Metastable Materials', eds: B. H. Kear and B. C. Giessen, Mat. Res. Soc. Symp. Proc., Elsevier Science Publishing Co. Inc., (1984), p. 3.
57. J. Powell, Conf. on "Surface Engineering with Lasers", held on May 22-26 at London 1985, Metal Society Publication, London.
58. V. M. Weerasinghe and W. M. Steen, in 'Applied Laser Tooling', eds: O. D. D. Soares and M. Derez-Amor, Martinus Nijhoff Publishers, Dordrecht, (1987), p. 183.
59. K. Mukherjee, T. H. Kim and W. T. Walter, in 'Laser in Metallurgy', eds: K. Mukherjee and J. Mazumder, Conf. Proc. of AIME held at Chicago, Ill on Feb 22-26, 1981, p.137.
60. Y. Arata, Plasma, Electron and Laser Beam Technology: Development and use in Materials Process, ASM Publication, (1986), p. 415.
61. G. Christodoulou, W. M. Steen, "Laser Surface Treatment of Chromium Electroplated Medium Carbon Steel", Paper in 4th int. conf. on Laser Processing held at Los Angeles, Jan., 1983.

62. C. W. Draper, *Appl. Surf. Sci.*, 7, (1981), p. 276.
63. D. S. Gnanamthu, *Opt. Eng.*, 19, (1980), p. 783.
64. J. D. Ayers, R. J. Schafer and W. P. Robers, *J. Met.*, 33, (8), (1981), p. 276.
65. J. H. P. C. Megaw, *Surfacing J.*, 11, (1980), p. 6.
66. C. J. Lin and F. Spaepen, *Proc. Mater. Res. Soc.*, 28, (1984), p. 75.
67. C. J. Lin, F. Spaepen and D. Turnbull, *J. Non-Crystal.*, 61, (1984), p. 712.
68. R. C. Ruhl, B. C. Giessen, M. Cohen and N. J. Grant, *Acta Metall.*, 15, (1967), p. 1693.
69. P. L. Bonora, *Electro. Chem. Acta*, 25, (1980), p. 1499.
70. P. L. Bonora, *Thin Solid Films*, 8, (1981), p. 339.
71. N. D. Tomashov, G. P. Chernova and T. A. Feseeva, *Prof. Met. (USSR)*, 13, (1977), p. 134.
72. C. W. Draper, *Thin Solid Films*, 75, (1981), p. 237.
73. M. MacIntyre, "Laser Hardfacing of RB211 Turbine Blade Shroud Interlocks", Paper in 2nd Int. Conf. on Application of Laser in Materials Processing, held at Los Angeles, Jan. 1983
74. M. Eboo and A. E. Lindemanis, "Advances in Laser Cladding Technology", Paper in LIA Conf. held at Los Angeles, May 1985.
75. A. H. Claer, B. P. Fairand, in 'Source Book on Applications of the Laser in Metal Working', ed: E. A. MetzBower, ASM Engg Bookshelf, (1981), p. 229.
76. W. F. Bates, in 'Source Book on Applications of the Laser in Metal Working', ed: E. A. MetzBower, ASM Engg Bookshelf, (1981), p. 254.
77. S. C. Ford, B. P. Fairand, A. H. Claer and R. D. Galliner, in 'Source Book on Applications of the Laser in Metal Working', ed: E. A. MetzBower, ASM Bookshelf, (1981), p. 271.
78. S. A. Tower, *Manufacturing Eng.*, 8, (1984), p. 145.
79. G. H. Harth, W. C. Leslie, V. G. Gregson and B. A. Anders, *J. Met.*, 4, (1976), p. 5.

80. P. J. Oakley, ICALEO, 1983, vol 38, LIA, Toledo, OH, p. 118.
81. R. K. Shiue and C. Chen, Metall. Trans., 2A, (1991), p. 221.
82. J. A. Wine, Laser Focus, 11, (1979), p. 44.
83. H. B. Singh and S. M. Copley, Metall. Trans., 12A, (1981), p. 138.
84. P. G. Moore and E. McCafferty, J. Electro. Chem. Soc., 128, (1981), p. 1391.
85. P. A. Molian, Script. Metall., 16, (1982), p. 65.
86. P. A. Molian and W. E. Wood, Script. Metall., 16, (1982), p. 1301.
87. P. A. Molian and W. E. Wood, J. Mat. Sci., 18, (1983), p. 2555.
88. P. A. Molian, Mat. Sci. Eng., 58, (1983), p. 175.
89. P. A. Molian and W. E. Wood, Mat. Sci. Eng., 56, (1982), p271.
90. W. A. Glaeser and B. P. Fairand, in 'Source Book on Applications of the Lasers in Metal Working', ed: E. A. MetzBower, ASM Engg Bookshelf, (1981), p. 292.
91. M. Yessik and R. P. Scherer, in 'Source Book on Applications of the Lasers in Metal Working', ed: E. A. MetzBower, ASM Engg Bookshelf, (1981), p. 219.
92. J. D. Ayers, T. R. Tucker and R. J. Shaefer, in 'Source Book on Applications of the Laser in Metal Working', ed: E. A. MetzBower, ASM Bookshelf, (1981), p. 301.
93. H. S. Carslaw, Introduction to the Mathematical Theory of the Conduction of Heat in Solid, 2nd edition, MacMillan, New York, (1921), p. 150.
94. D. Rosenthal, Welding Journal, (1941), vol 20, p. 220s.
95. L. Tall, PhD Thesis, Lehigh University, (1961), p. 106.
96. N. Dahotre, PhD Thesis, Michigan State University, (1987).
97. D. Rosenthal, Trans. ASME, (1946), 48, p. 848.
98. S. Kou, Metall. Trans., A, 13A, 3, (1982), p. 363.

99. W. F. Hess, L. L. Merrill, E. F. Nippes, Jr. , and A. P. Buruk, *Weld. J.*, (1943), vol 22, p. 3775.
100. R. S. Myers, O. A. Uyehara and G. L. Borman, *Weld. Res. Coun. Bull.*, July 1967, No. 123.
101. D. J. Swifthook and A. F. Gick, *Weld. J.*, (1973), vol 52, p. 4925.
102. P. Jhaveri, W. G. Moffatt and C. M. Adams, Jr., *Weld. J.*, (1962), vol 41, p. 125.
103. R. Trivedi and S. R. Srinivasan, *J. Heat. Transf.*, (1974), vol 96, p. 427.
104. V. Pavelic, R. Tanbakuchi, O. A. Uehara and P. S. Myers, *Weld. J.*, 1969, vol 48, p. 295s.
105. E. Friedman, *J. Press. Vessel Tech.*, (1975), vol 975, p. 206.
106. E. Friedman, *Nucl. Metall.*, (1976), vol 20, 1160.
107. Y. Sharir, A. Grill and J. Pelleg, *Metall. Trans.*, 11B, (1980), p. 257.
108. T. Chande and J. Mazumder, in 'Lasers in Metallurgy', eds: K. Mukherjee and J. Mazumder, The Metallurgical Society of AIME, Warrendale, PA, (1981), p. 165.
109. J. A. Sekhar, S. Kou and R. Mehrabian, *Metall. Trans.*, 14A, (1983), p. 1169.
110. C. R. Lamar, "Laser Diagnosis by Heat Conduction", AIAA/ASME 4th Joint Thermo-physics and Heat Transfer Conf., June 2-4, 1986, Boston, MA, AIAA, 1633, Broadway, New York, NY, p. 56.
111. K. V. RamaRao and J. Sekhar, *Acta Metall.*, vol 35, No. 1, p. 81.
112. Y. Arata, K. Inou, H. Maruo and I. Miyamoto, in 'Electron and Laser Beam Technology: Development and use in Materials Process', ed: Y. Arata, ASM Publication, (1986), p. 550.
113. H. Maruo, I. Miyamoto, T. Ishida and Y. Arata, in 'Electron and Laser Beam Technology: Development and use in Materials Process', ed: Y. Arata, ASM Publication, (1986), p. 568.
114. T. Zacharia, S. A. David, J. M. Vitek and T. Debroy, *Metall. Trans. A*, 20A, (1989), p. 957.

115. P. Cacciatore, in 'Modeling of Casting and Welding Progress', eds: H. D. Brody and Diran Apelian, Conf. Proc., Aug 3-8, 1980, The Metallurgical Soc. of AIME, Warrendale, PA, p. 113.
116. S. Kou, in 'Modeling of Casting and Welding Progress', eds: H. D. Brody and Diran Apelian, Conf. Proc., Aug 3-8, 1980, The Metallurgical Soc. of AIME, Warrendale, PA, p. 113.
117. T. Debroy, J. Szekely and T. W. Eagar, in 'Modeling of Casting and Welding Progress', eds: H. D. Brody and Diran Apelian, Conf. Proc., Aug 3-8, 1980, The Metallurgical Soc. of AIME, Warrendale, PA, p. 113.
118. F. Blottner, in 'Modeling of Casting and Welding Processes II', eds: J. A. Dantzig and J. T. Berry, Conf. Proc., July 31-Aug. 5, 1983, p. 349.
119. S. Kou, Welding Metallurgy, A Wiley-Interscience Publication, John Wiley & Sons, New York, NY, P. 143.
120. W. F. Savage, C. D. Lundin and A. H. Aronson, Weld. J., 44, (1965), p.175s.
121. W. F. Savage and R. J. Hrubec, Weld. J., 51, (1972), p. 260s.
122. S. Kou, Welding Metallurgy, A Wiley-Interscience Publication, John Wiley & Sons, New York, NY, P. 146.
123. V. Laxmanan, Rapid Solidification, Mat. Res. Soc. Symp., vol 28, (1984), p. 21.
124. K. A. Jackson , Solidification, ASM, Metal part, OH, (1971), p. 121.
125. T. Z. Kattamis, U. T. Holmber, and M. C. Fleming, J. Inst. Met., 55, (1963), p. 343.
126. W. A. Tiller, K. A. Jackson, J. W. Rutter and B. Chalmer, Acta. Meta., 1, (1953), p. 428.
127. R. F. Sekerka, J. Phys. Chem. Sol., 28, (1967), p. 983.
128. M. C. Fleming, Solidification Processing, McGraw Hill, New York, 1974.
129. K. A. Jackson and J. S. Hunt, Acta. Meta., 13, (1965), p. 1212.
130. B. Brando and R. Sabastiano, Rapidly Quenched Metal, ed: S. Steel and H. Warlimont, Elsevier Science Publications, (1985), p. 851.

131. T. W. Clyne, Metall. Trans., 13B, (1982), p. 471.
132. T. W. Clyne, Metall. Trans., 15B, (1984), p. 369.
133. S. Kou, Welding Metallurgy, A Wiley-Interscience Publication, John Wiley & Sons, New York, NY, P. 133.
134. C. Chabrol and A. B. Vannes, in 'Laser Surface Treatments of Metals', NATO Advanced Study Institute on Laser Surface Treatments of Metals 1985, San Miniato, Italy, Martinus Nijhoff; Norwell, MA, USA.
135. E. Macherauch and K. H. Kloos, in 'Residual Stresses in Science and Technology', vol 1, eds: E. Macherauch and V. Hauk, Conf. Proc. for Int. In Conf. on Residual Stresses, Deutsche Gesellschaft fur Metallkunde, (1986), p. 3.
136. I. C. Noyan and J. B. Cohen, American Scientist, vol 79, March-April, 1991, p. 142.
137. W. Baldwin, Jr., "Residual Stresses in Metals", Paper Presented before 52th annual meeting of the ASTM, ASTM, Philadelphia, PA, (1949).
138. J. T. Norton and D. Rosenthal, Weld. J. , Res. suppl., Feb, (1943), p. 1.
139. E. D. Walker, in 'Residual Stress for Designers and Metallurgist', ed: L. J. Vande Walle, Conf. Proc. of ASM held on 9-10 April, 1980, at Chicago, IL, p. 41.
140. H. Wohlfraht, in 'Advances in Surface Treatment', ed: A. Niku-Lari, vol 4, Pergamon Press, 1986, p. 40.
141. G. Beck and T. Erickson, in 'Residual Stresses in Science and Technology', vol 1, eds: E. Macherauch and V. Hauk, Conf. Proc. for Int. In Conf. on Residual Stresses, Deutsche Gesellschaft fur Metallkunde, (1986), p. 135.
142. S. Denis and A. Simon, in 'Residual Stresses in Science and Technology', vol 2, eds: E. Macherauch and V. Hauk, Conf. Proc. for Int. In Conf. on Residual Stresses, Deutsche Gesellschaft fur Metallkunde, (1986), p. 565.
143. S. Denis, S. Sjostrom and A. Simon, in 'Residual Stresses in Science and Technology', vol 2, eds: E. Macherauch and V. Hauk, Conf. Proc. for Int. In Conf. on Residual Stresses, Deutsche Gesellschaft fur Metallkunde, (1986), p. 595.

144. E. P. DeGarmo, J. L. Meriam and F. Jonassen, *Weld. J.*, 25, (1946), p.485s
145. L. Tall, *Weld. J.*, 43, (1964), Res. Suppl., p. 10s.
146. N. R. Nagaraja and L. Tall, *Weld. J.*, 40, (1961), Res. Suppl., p. 468s.
147. J. O. Kristianson, *J. therm. Stresses*, vol 5, (1982), p. 315.
148. A. J. Fletcher, *Thermal Stress and Strain Generation in Heat Treatment.*, Elsevier Applied Science, London, (1989), p. 193.
149. L. Karlsson, *Thermal Stresses I*, vol1, Ed: R. B. Hetnarski, Elsevier Science, (1986), p. 299.
150. C. A. Peck, in '*Residual Stresses in Design, Process and Materials Selection*', Conf. Proc. of ASM held at Cincinnati, OH on April 27-29, 1987. ASM Publication, p. 7.
151. R. L. Frohlick, in '*Residual Stresses in Design, Process and Materials Selection*', Conf. Proc. of ASM held at Cincinnati, OH on April 27-29, 1987. ASM Publication, p. 63.
152. I. C. Noyan and J. B. Cohen, *Residual Stresses*, MRE, Spring-verlag, (1987), p. 117.
153. K. Masubuchi, *Analysis of Welded Structures in Residual Stresses and Distortion and their Consequences*, Pergamon Press, Oxford, (1980), p. 231.
154. L. C. Cox, in '*Residual Stresses in Design, Process and Materials Selection*', Conf. Proc. of ASM held at Cincinnati, OH on April 27-29, 1987. ASM Publication, p. 109.
155. E. M. Beaney, *Strain*, 2, (1976), p. 99.
156. E. M. Beaney and E. Proctor, *Strain*, 10, (1974), p. 7.
157. A. J. Fletcher, *Thermal Stress and Strain Generation in Heat Treatment.*, Elsevier Applied Science, London, (1989), p. 199.
158. J. G. Zhao, A. M. Huntz and J. L. Baron, *Acta Metall.*, vol 17, (1986), p. 135.
159. A. M. Huntz and J. G. Zhao, in '*Residual Stresses in Science and Technology*', vol 1, eds: E. Macherauch and V. Hauk, Conf. Proc. for Int.

- In Conf. on Residual Stresses, Deutsche Gesellschaft für Metallkunde, (1986), p. 223.
160. I. C. Noyan and J. B. Cohen, Residual Stresses, MRE, Springer-verlag, (1987), p.4.
  161. B. D. Cullity, Elements of X-ray Diffraction, Second edition, Addison-Wesley, (1978), p. 458.
  162. S. Kou, Welding Metallurgy, A Wiley-Interscience Publication, John Wiley & Sons, New York, NY, P. 122.
  163. J. T. Luxon and D. E. Parker, Industrial Lasers and Their Applications, Prentice Hall Inc., Engle Wood Cliffs, New Jersey, p.201.
  164. J. F. Lancaster, Metallurgy of Welding, 4th edition, Addison-Wiley & Sons, New York, NY, P. 127.
  165. J. Nutting, J. Iron Steel Inst., vol 6, (1969), p. 872.
  166. W. Amende, Industrial Applications of Lasers, Wiley-Interscience publ., (1984), p. 79.
  167. H. J. Hegge and J. T. M. De Hosan, Scrip. Met., vol21, (1987), p. 1737.
  168. R. A. Grange, Trans. AIME, vol 59, (1966), p26
  169. G. H. Harth and W. C. Leslie, Weld J. Res Supp., vol 54, (1975), p. 205.
  170. W. C. Leslie, The Physical Metallurgy of Steel, McGraw Hill, New York (1982), p. 180.
  171. A. Walker, D. R. F. West and W. M. Steen, Met. Tech., vol 11, (1984), p. 399.
  172. A. Walker, H. M. Flower and D. R. F. west, J. Met., vol 20, (1985), p.989.
  173. C. H. Chen, C.J. Altstetter and J. M. Rigsbee, Met. Trans. A, vol 15A, (1984), p. 719.
  174. B. Badan, L. Giordano, E. Ramous, in 'Rapidly Solidified Metals VI' eds: S. Steels and H. Warlimonts, Elsevier Sci. Publications, (1985), p.855.
  175. G. Barton, M. Diefenbach and J. betz, in 'Rapidly Solidified Metals VI' eds: S. Steels and H. Warlimonts, Elsevier Sci. Publications, (1985), p.851.

176. W. AiHua, T. Zengyi and Z. Beidi, *Weld. Res. Supp*, 04, (1991), p. 107s.
177. B. L. Mordike, H. W. Bergman, 'Rapidly Solidified Metastable Materials', eds: B. H. Kear and B. C. Giessen, *Mat. Res. Soc. Symp. Proc.*, Elsevier Science Publishing Co. Inc., (1984), p. 30.
178. C. S. Roberts, *Trans. AIME*, vol 197, (1953), p. 203.
179. C. Y. Kung and J. J. Rayment, *Met Trans. A*, vol 13A, 02, (1992), p. 328.
180. D. G. Morris, *Mat. Sci. Eng.*, vol 16, (1982), p. 457.
181. L. E. Eiselstein, O. A. Ruano and O. D. Sherby, *J. Met.*, vol 18, (1983), p. 483.
182. L. M. Gourd, Principles of Welding Technology, second edition, Edward Arnold, 1985, p. 203.
183. D. L. Chambers, K. A. Taylor, C. T. Wan and G. T. Susi, *J. Vac. Sci. Tech. A* May/June, (1991), p1104.
184. A. P. Epik, in 'Boron and Refractory Borides', ed.: P V. I. Matkovich, Springer-Verlag, New York, (1977), p. 597.
185. O. Kubaschewski, Iron Binary Phase Diagram, Springer-Verlag, New York (1981), p. 15.
186. P. Goeuriot, F. thevnot, J. H. Driver, T. Magnin, in 'Advances in Surface Treatments', vol 2, Edt.: A. Niku-Lari, (1988), p. 171.
187. K. Kumar and E. Stuart, *Mat. Eng.*, vol 4, (1973), p. 70.
188. E. Horbogen and S. Stanieze, *Z. Metallkunde*, vol 79, (1988), p. 171.
189. Y. Khan and M. Sostarich, *Z. Metallkunde*, Vol 72, (1981), p. 261.
190. M. Carbucchio, L. Bardani and G. Palombari, *J. Met.*, vol 15, (1980), p. 711.
191. J. V. Beck, *AIAA J.*, vol 24, 1988, p. 327.
192. J. V. Beck, Haji-Seikh and K. D. Cole, Green's Functions in Heat Conduction Problems, McGraw Hill, 1991, p. 150
193. M. N. Ozisik, Heat Conduction, A Wiley-Interscience publication, New York, 1980, p. 74.

MICHIGAN STATE UNIV. LIBRARIES



31293010553257